TAILORING POLYELECTROLYTE MULTILAYER NANOFILTRATION MEMBRANES THROUGH AEROSOL-ASSISTED PRINTING

LIHONG GAN

PhD

The Hong Kong Polytechnic University

2025

The Hong Kong Polytechnic University

Department of Civil and Environmental Engineering

Tailoring Polyelectrolyte Multilayer Nanofiltration Membranes through Aerosol-Assisted Printing

Lihong GAN

A thesis submitted in partial fulfilment of the requirements for the degree of Doctor of Philosophy

August 2025

CERTIFICATE OF ORIGINALITY

I hereby declare that this thesis is my own work and that, to the best of my knowledge and belief, it reproduces no material previously published or written, nor material that has been accepted for the award of any other degree or diploma, except where due acknowledgement has been made in the text.

_____(Signed)

_____Lihong GAN_____(Name of student)

Abstract

Polyelectrolyte multilayer (PEM) nanofiltration (NF) membranes, composed of alternatively charged polyelectrolytes (PE) assembled via layer-by-layer (LbL) deposition, have gained considerable attention owing to their highly tunable surface properties, excellent separation performance, and potential for multifunctional integration. The traditional LbL assembly method by dip coating typically involves sequential immersion of a substrate into oppositely charged PE solutions. However, this approach is inherently time-intensive due to the slow diffusion of PEs in aqueous media and requires large volumes of solutions, limiting its scalability for applications. This limitation presents a major bottleneck in the widespread application of PEM technology. Moreover, effectively addressing diverse water and wastewater challenges necessitates the development of PEM NF membranes with precisely controlled structures and performance characteristics tailored to specific treatment goals.

To address the challenges of scalability, this work reports the first application of aerosol-assisted printing (AAP) to PEM NF membrane fabrication, and the overarching goal is to establish fabrication-structure-performance relationships to develop PEM NF membranes with tunable permeability and selectivity. In this thesis, an AAP system is built by modifying a commercial 3D printer with a Collison nebulizer. Different PEM membranes are fabricated using three PE pairs: polyethyleneimine (PEI)/poly(sodium 4-styrenesulfonate) (PSS), poly(allylamine hydrochloride) (PAH)/PSS, and poly(diallyldimethylammonium chloride) (PDDA)/PSS. A higher viscosity of the PE solution leads to larger droplets with increased momentum, thereby improving deposition efficiency and resulting in the formation of a thicker PE layer. The thicker and denser PEI/PSS membranes exhibit lower water permeability and higher rejection of neutral organic solutes than the other two membranes. The PAH/PSS membranes and PDDA/PSS membranes exhibit a loose

structure. Among these membranes, the PEI/PSS membrane is chosen as the most promising PEM NF candidate because it can achieve NF-level separation with minimal fabrication time and material. The thicknesses of the PE layer and PEM exhibit linear growth as the printing scan number increases. Furthermore, PE interdigitation forms an effective polymeric network barrier, which increases resistance to solute and water transport. By manipulating the PE deposition mass and layering, PEM membranes with tunable pore radii and water permeability are obtained for various water treatment applications, ranging from humic acid retention to micropollutant removal.

The drying process (water evaporation) is not merely a post-treatment step but an integral part of the assembly when using the AAP method. The drying of the PEM membrane proceeds through three sequential stages: compaction of the PEM, deformation of the substrate, and eventual tearing of the PEM due to interfacial stress. The compaction of the PEM layer improves selectivity, but the substrate deformation drives permeability loss. This difference results from the different elastic moduli and pore architectures of the PEM and substrates. Furthermore, incorporation of glycerol into either the substrate or the PEM can effectively preserve membrane structure during drying and maintain its filtration performance, due to the diffusion or convective mass transfer of glycerol between the PEM and substrate.

This thesis demonstrates the AAP method as an effective and practical approach for fabricating PEM membranes at scale. The PEM membranes can be tailored from loose to dense NF to meet diverse water treatment needs. Overall, this thesis advances the fabrication, application, and storage of PEM membranes, providing key technical insights that support their broader application in sustainable water purification.

Acknowledgements

I would like to express my deepest gratitude to my supervisor, Prof. Yi JIANG, for his guidance, support, and mentorship throughout my PhD study. Beginning my PhD in 2020, during the unprecedented COVID-19 pandemic, was uniquely challenging. Without his unwavering support, I would not have been able to pursue and complete this work. His visionary insights, relentless passion for research, and educational philosophy have profoundly influenced both my academic growth and professional aspirations. It is a great honor and privilege to conduct my doctoral research under his supervision.

I would also like to extend my heartfelt thanks to Prof. Peng WANG, who has offered me guidance and experimental support. My sincere appreciation goes to Prof. Shihong LIN of Vanderbilt University, whose helpful suggestions and thoughtful guidance greatly supported my published paper. I am also thankful to my thesis examination committee for their time, thoughtful comments, and rigorous review, all of which significantly improved the quality of this work.

I am deeply grateful to several senior colleagues for their mentorship and encouragement, including Dr. Delai ZHONG, Dr. Zhuo CHEN, Dr. Zhenyu ZHAO, Dr. Yangtao WU, Dr. Xiaoqing LIU, Dr Bo PENG, and Dr. Zhishang WAN. My thanks also go to other members of Prof. Jiang's research group, including Jin ZHANG, Yuchen WU, Beizhao CHEN, Si YANG, Liang WEI, Yiru CHEN, Chengfeng WAN, Yuan XIAO, Yanni WENG, Xunjie LI, and Cleo KLOSSNER. I also wish to acknowledge the dedicated technical staff in the water lab, including WS LAM, Jonathan CHAN, Celine CHE, Bosco TAM, and Kate TAM, for their assistance with my laboratory work.

Additionally, I thank the funding support from the Hong Kong Research Grants Council (15214222) and Science, Technology and Innovation Commission of Shenzhen Municipality (SGDX20210823103401009).

I would like to thank my dear friends, Dr. Zhihang XUE, Dr. Haixin LIU, Dr. Yaohan LI, Dr. Partha DEBNATH, Dr. Kunal Krishna DAS, Dr. Yanlin ZHANG, and Manli WANG, for their warm encouragement, kind companionship, and unwavering support over the years.

Finally, I would like to thank my parents, parents-in-law, and my husband, Dr Yi HE. Thank you for being my rock. Your faith in me has been a constant source of strength.

Table of Contents

Abstract i

Acknowledgements iii

Table of Contents v

List of Figures ix

List of Tables x

Chapter 1. Introduction 1

Chapter 2. Literature Review 10

2.1 Polyelectrolyte-Based Coatings 10

2.1.1 Polyelectrolytes 10

2.1.2 Polyelectrolyte Complex (PEC) 11

2.1.3 Polyelectrolyte Multilayer 13

2.2 Polyelectrolyte Multilayer Assembly Method 15

2.2.1 Dip Coating 15

2.2.2 Spin Coating 16

2.2.3 Spray Coating 18

2.2.4 Inkjet Printing 19

2.2.5 Comparison of the Polyelectrolyte Multilayer Assembly Methods 20

2.3 Aerosol-Assisted Printing for Membrane Fabrication 22

2.3.1 Aerosol 22

2.3.2 Aerosol Deposition Principle 23

2.3.3 Aerosol-Jet Printing 24

2.4 Polyelectrolyte Multilayer Nanofiltration Membrane Application in Water and Wastewater Treatment 26

2.4.1 Separation Mechanisms 26

2.4.2 Water and Wastewater Treatment 28

Chapter 3. Polyelectrolyte-Dependent Spray Dynamics and Molecular Interactions in Aerosol-Assisted Printing of Multilayer Membranes: Implications on Assembly and Filtration Performance 30

Abstract 30

3.1 Introduction 31

3.2 Experimental 35

3.2.1 Materials and Chemicals 35
3.2.2 Aerosol-Assisted Printing Setup 35
3.2.3 PEM Membrane Fabrication 36
3.2.4 Characterization of Aerosol Deposition Process 37
3.2.5 Membrane Characterization 37
3.2.6 Membrane Filtration Performance 38
3.3 Results and Discussion 39
3.3.1 Polyelectrolyte Aerosol Characterization 39
3.3.2 PE Aerosol Deposition and Multilayer Formation 41
3.3.3 Characteristics of Polyelectrolyte Multilayer Membranes 44
3.3.4 Membrane Filtration Performance 46
3.4 Conclusion 49
Acknowledgement 50
Appendix A: Supporting Information for Chapter 3 51
Chapter 4. Tailoring Polyelectrolyte Multilayer Nanofiltration Membranes by Aerosol-Assisted Printing: Insights into Membrane Formation Mechanisms 53
Abstract 53
4.1 Introduction 55
4.2 Experimental 58
4.2.1 Materials and Chemicals 58
4.2.2 Polyelectrolyte Multilayer Membrane Fabrication 58
4.2.3 Characterization of Aerosol Deposition Process 60
4.2.4 COMSOL Simulation 60
4.2.5 Membrane Characterization 61
4.2.6 Membrane Filtration Performance Evaluation 61
4.3 Results and Discussion 62
4.3.1 Polyelectrolyte Aerosol Generation, Characterization, and Deposition 62
4.3.1.1 Polyelectrolyte Droplet Generation by Aerosolization 62
4.3.1.2 PE Aerosol Transport 63
4.3.1.3 Aerosol Deposition Mechanism 64
4.3.2 Membrane Formation Mechanism 66

4.3.2.1 Formation of a Polyelectrolyte Layer 66
4.3.2.2 Polyelectrolyte Multilayer Assembly 68
4.3.3 Membrane Filtration Performance 71
4.3.3.1 Water Flux and Molecular Weight Cut Off 71
4.3.3.2 Retention of Micropollutants 75
4.4 Conclusion 76
Acknowledgement 77
Appendix B: Supporting Information for Chapter 4 77
Chapter 5. Drying Effects on Structure and Performance of Polyelectrolyte Multilayer Membranes: Insights into Differential Responses of the Polyelectrolyte Multilayer Compaction and Substrate 97
Abstract 97
5.1 Introduction 98
5.2 Experimental 101
5.2.1 Materials and Chemicals 101
5.2.2 Polyelectrolyte Multilayer Membrane Fabrication 101
5.2.3 Glycerol-Polyelectrolyte Multilayer Membrane Preparation 102
5.2.4 Controlled Drying Experiment 103
5.2.5 Water Evaporation Experiment 103
5.2.6 Membrane Characterization 103
5.2.7 Membrane Filtration Performance 104
5.3 Results and Discussion 105
5.3.1 Water Evaporation Process 105
5.3.2 Characterization of Dried Polyelectrolyte Multilayer Membranes 110
5.3.3 Drying Effect on Membrane Filtration Performance 112
5.3.3.1 Drying Effect on the Substrate 112
5.3.3.2 Drying Effect on Polyelectrolyte Multilayer Membrane 114
5.3.4 Glycerol's Effect on Preventing Pore Structure Shrinkage 118
5.4 Conclusion 121
Acknowledgement 122
Appendix C: Supporting Information for Chapter 5 123

Chapter 6. Conclusions, Impacts, and Future Directions..... 126
6.1 Conclusions..... 126
6.2 Impacts..... 127
6.3 Future Directions..... 128
Reference..... 130

List of Figures

Figure 1.1 Schematic of PEM membrane fabrication with alternating electrostatic deposition of polycation and polyanion on a substrate. 3

Figure 2.1 Chemical structures of polyethyleneimine (PEI), poly (allylamine hydrochloride) (PAH), poly(diallyldimethylammonium chloride) (PDDA), poly(sodium 4-styrenesulfonate) (PSS), and poly(acrylic acid) (PAA). 11

Figure 2.2 Schematic structure of PECs: ladder-like model and scrambled egg model. 13

Figure 2.3 Schematic illustration of dip coating, spin coating, spray coating, and inkjet printing. 15

Figure 2.4 Schematic illustration of aerosol-jet printing. 25

Figure 3.1 (a) Droplet size distribution of PEI, PAH, PDDA, and PSS droplets, (b) Dv_{50} of PEI, PAH, PDDA, and PSS droplets, (c) viscosity of PEI, PAH, PDDA, and PSS solutions, (d) surface tension of PEI, PAH, PDDA, and PSS solutions, and (e) the vertical velocity distribution field of PEI, PAH, PDDA, and PSS aerosols under nebulizer pressure of 1 bar. 40

Figure 3.2 (a-d) Size distribution of deposited PEI, PAH, PDDA, and PSS particles on the silicon wafer, and the inset figures are representative phase, (e) comparison of PEI, PAH, PDDA, and PSS deposition efficiency under 1 bar nebulizer pressure and (f-h) cross-section SEM images of $(PEI/PSS)_2$, $(PAH/PSS)_2$, and $(PDDA/PSS)_2$ membranes, respectively. 42

Figure 3.3 Surface characterization of the different PEM membranes including PEI/PSS, PAH/PSS, PDDA/PSS membranes and hydrolyzed polyacrylonitrile (HPAN) substrate: (a) surface zeta potential evolution at pH 7 during LbL deposition of polycation (PC) and polyanion (PA), (b) water contact angle evolution during LbL deposition of PC and PA, and (c) ratios of elemental fraction of nitrogen (N) to sulfur (S) of the $(PEI/PSS)_2$, $(PAH/PSS)_2$, and $(PDDA/PSS)_2$ membranes determined from the XPS depth profiling analysis. 45

Figure 3.4 Filtration performance of $(PEI/PSS)_2$, $(PAH/PSS)_2$, and $(PDDA/PSS)_2$ membranes and HPAN substrate: (a) pure water permeability, (b) PEG rejection curve; and (c) Salt rejection of $(PEI/PSS)_2$, $(PAH/PSS)_2$, and $(PDDA/PSS)_2$ membranes. 47

Figure 4.1 Schematics of (a) the PEM membrane fabrication process via aerosol-assisted printing and (b) formation of the $(PEI_nPSS_n)_x$ membrane with various scans and bilayer numbers. Note: n represents n scans for each PEI or PSS layer (n =1-5). 59

Figure 4.2 Droplet and particle size measurement: size distribution of (a) PEI and (b) PSS droplets generated under different nebulizer pressure; (c) the D_{v50} of PEI and PSS droplets under different nebulizer pressure; (d) droplet velocity of PEI aerosols at the nozzle exit under different nebulizer pressure; (e) velocity distribution field under 1 bar nebulizer pressure from the COMSOL simulation. 64

Figure 4.3 (a) Schematic of a PE layer formation showcasing the transformation from droplets into a complete PE layer; (b) size distribution of deposited PEI and PSS particles on the silicon wafer, and the inset figures are representative phase AFM images; (c) variation in the thickness of the PEI and PSS layers with different scans obtained from analysis of cross-sectional SEM images. 67

Figure 4.4 Surface characterization of the $(PEI_nPSS_n)_x$ membranes with different bilayer numbers and scans for each single layer. (a) FTIR spectra, (b) surface and cross-section SEM images, (c) the ratios of elemental fraction of nitrogen (N) to sulfur (S) of the $(PEI_2PSS_2)_2$ and PEI_4PSS_4 membranes determined from the XPS depth profiling analysis, and (d) corresponding schematic of PEM assembly. 69

Figure 4.5 Filtration performance and pore characteristics of the $(PEI_nPSS_n)_x$ membranes with different bilayer numbers and scans: (a) PWP, (b) intrinsic rejection (R_i) of neutral organic solutes by the one-bilayer $(PEI_nPSS_n)_1$ membranes, (c) intrinsic rejection (R_i) of neutral organic solutes by the two-bilayer $(PEI_nPSS_n)_2$ membranes, (d) estimated mean pore radius, (e) observed rejection of BPA (BPA R_{obs}), and (f) observed rejection (R_{obs}) of AP, BPA, CIP, and OFX by the $(PEI_3PSS_3)_2$ membrane..... 73

Figure 5.1 Drying effect on moisture content of the substrate and PEM membranes at 60% RH and ambient temperature: (a) HPAN substrate, (b) glycerol pre-filled HPAN substrate (GHPAN), (c) PEM membrane fabricated on the HPAN substrate (HPAN-PEM), and (d) PEM membranes fabricated on glycerol pre-filled HPAN substrates (GHPAN-PEM), (e) PEM membranes with exclusive glycerol incorporation in the PEM (HPAN-GPEM), (f) PEM membranes with glycerol incorporation in both the PEM and the HPAN substrate (GHPAN-GPEM), and the inset figures are magnified view of moisture decrease within the first 0-1.5 hours..... 107

Figure 5.2 (a) FTIR spectra for substrate and PEM membranes after 24-hours drying including the comparison among PAN, HPAN substrate and GHPAN substrate and the comparison among HPAN-PEM membrane, HPAN-GPEM membrane, GHPAN-PEM membrane, and GHPAN-GPEM membrane. (b) Surface SEM images of the substrates and PEM membranes after 0 hours and 24 hours drying including HPAN substrate, PEM membrane, (GHPAN) substrate, and GHPAN-PEM membrane.....111

Figure 5.3 Filtration performance of the HPAN substrates and PEM membranes after different drying time at 60% RH: (a) pure water permeability of HPAN substrates, (b) PEG rejection curve of HPAN substrates, (c) pure water permeability of PEM membranes, (d) PEG rejection curve of PEM membranes after 0, 1 and 2 hours, (e) PEG rejection curve of PEM membranes after 4, 6, 8 and 24 hours, (f) estimated mean pore radius of PEM membranes, and (g) hydration resistance ratio of PEM and HPAN substrates.....113

Figure 5.4 Hydraulic resistance ratio between PEM films and HPAN substrates after different drying time at 60% relative humidity.....118

Figure 5.5 Pure water permeability, and PEG rejection curve of the PEM membranes after 1, 4, 24 hours of drying time at 60% RH: (a) glycerol pre-filled HPAN (GHPAN) substrate, (b) PEM membranes fabricated on glycerol pre-filled HPAN substrates (GHPAN-PEM), (c) PEM membranes with exclusive glycerol incorporation in the PEM (HPAN-GPEM), (d) PEM membranes with glycerol incorporation in both the PEM and the HPAN substrate (GHPAN-GPEM). 119

List of Tables

Table 2.1 Comparison of the PEM assembly methods, including dip coating, spin coating, spray coating, and inkjet printing. 21

Chapter 1. Introduction

1.1 Background

Water scarcity has emerged as one of the most pressing challenges to the sustainability of modern society. To advance sustainable development, it is imperative to implement effective water treatment and management strategies that can both eliminate pollutants and ensure the supply of clean drinking water. Membrane technology has been playing an increasingly important role in water purification over the past few decades and has replaced some conventional processes due to its cost-effectiveness, ease of use, and environmental friendliness. Based on current market analyses, the global membrane separation technology market was valued at approximately USD 31.08 billion in 2024 and is expected to grow substantially to around USD 100.93 billion by 2034 (Bidwai, 2025), reflecting an annual growth rate of 12.5% over the forecast period. This growth is largely driven by increasing demand for more efficient membrane separations to provide clean water.

Nanofiltration (NF) is an attractive pressure-driven membrane process for advanced water treatment because it can remove all pathogens and most organic and inorganic contaminants in a single treatment step and with affordable energy input (Yang et al., 2022). It is used for removing solutes with molecular weight (MW) in the range of 200-2000 g mol^{-1}, with typically high rejection of multivalent ions but low to moderate rejection of monovalent ions (Higaki et al., 2015). The current mainstream NF membranes are polyamide (PA)-based, which exhibit high water-salt selectivity, with Na_2SO_4 and $MgSO_4$ rejections exceeding 90%, but show limited selectivity toward micropollutants (Liu et al., 2022). For example, the commercial NF270 membrane rejects micropollutants with molecular weights of 200-300 Da at efficiencies ranging from 50% to 80% (Liu et al., 2022). Moreover, their slightly hydrophobic surfaces lead to high fouling propensity,

thus requiring frequent cleaning and high operational cost; also, PA is subject to electrophilic attack by hypochlorite (chemical cleaning), which causes a significant drop in performance after prolonged exposure (Kwon and Leckie, 2006). There is an urgent need for NF membranes with high water permeability and tailored selectivity, chlorine resistance, as well as anti-fouling properties.

Polyelectrolyte multilayer (PEM) membrane has emerged as a new promising alternative to PA membranes, which allows for convenient synergetic control of structure/charge properties of the active layer bulk and surface. While commercial PA membranes have achieved good separation performance over the past decade, PEM-enabled membranes provide advanced functionalities that can significantly expand the scope of NF applications. By layer-by-layer (LbL) self-assembly of polycation and polyanion in sequence, a PEM is coated on the surface of the substrate (Figure 1.1). The versatility of polyelectrolytes (PEs) leads to diverse membrane structures, properties, and separation performance. Furthermore, no organic solvents are involved, and therefore, the fabrication process is environmentally friendly. The availability of various PEs as building blocks, as well as coating conditions (e.g., pH and ionic strength), enables the production of thin films with a different structure for a variety of membrane applications. Outstanding separation performance of PEM includes high permeability and tunable solute selectivity (e.g., divalent over monovalent cations (X^{2+}/Na^{+}) (Durmaz et al., 2021), organic contaminants over divalent cations (Wang et al., 2021) or monovalent cations (Brinke et al., 2020)). The common PE chemistries are inherently more chlorine-resistant than PA as demonstrated by several studies (Cho et al., 2015; de Grooth et al., 2015). The hydrophilicity of the PEs and controllable surface charge render the membranes high fouling resistance (Ba et al., 2010; Liang and Lin, 2020; Sanyal et al., 2015; Son et al., 2018). Although the potential of PEM membranes for water and wastewater treatment is

widely recognized, the underlying science and engineering required for scalable manufacturing and application-specific performance optimization remain underdeveloped.

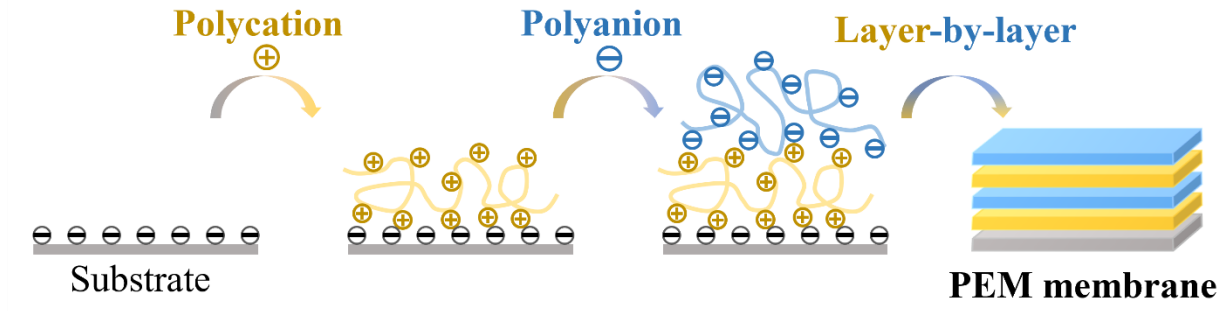

Figure 1.1 Schematic of PEM membrane fabrication with alternating electrostatic deposition of polycation and polyanion on a substrate.

1.2 Key Scientific and Engineering Issues

To apply the PEM membrane in water and wastewater treatment technologies, the first step is to identify the most applicable and advantageous membrane fabrication method. Common LbL fabrication methods for PEM include dip-coating, spin-coating, spray-coating, and inkjet printing. Taking the dip-coating method as an example, a substrate is cyclically immersed between two reservoirs containing aqueous solutions of PEs of opposite charges. In dip coating, a layer of PE is added to the oppositely charged substrate or the previously deposited layer via electrostatic force. The method usually takes a few hours to several days to achieve enough bilayers due to the diffusive time scale (Li et al., 2020). The limitations for dip-coating also include scalability challenges owing to the need for a substantial volume of solutions (for immersion). Spin coating could speed up the assembly process by using centrifugal force but can only cover tiny planar substrates. Another LbL assembly method, inkjet printing, enables precise and material-efficient

deposition but is relatively slow for large-area coating because droplets are deposited point-by-point. Therefore, it remains a challenge to speed up and scale up the PEM membrane fabrication.

Spray LbL assembly is a method in which films are assembled by aerosolizing solutions into droplets and spraying them sequentially onto substrates. The benefits of the spray-coating method include a drastic decrease in process time due to the improved means of mass transfer, a much smaller quantity of polymer solution required, reduced polymer aggregation, and controlled deposition dynamics for novel structures. Common spraying methods, such as spray guns and airbrushes, typically produce droplets with a broad size distribution, generally ranging from 30 to 50 μm in size (Chen and Lin, 2009; Scardaci et al., 2011). This large size hinders precise control over membrane properties, including its thickness and surface morphology. Rapid deposition of large droplets results in excessive material accumulation on the substrate within seconds, often forming overly thick PE layers (Xiang et al., 2015). Moreover, the drying process of large droplets leads to an uneven spread of PE on the substrate, resulting in low film uniformity and pronounced surface roughness, primarily because of the coffee-ring effect (Bose et al., 2013; Yunker et al., 2011). Thus, small droplets with a narrowly distributed size can facilitate precisely tuning the membrane property.

Aerosols are suspensions of small particles in gases, formed by the conversion of gases to particles or by the disintegration of liquids or solids (Friedlander, 1977). The Collison nebulizer generates aerosols/ fine droplets with sizes ranging from 1 to 5 μm (Feng et al., 2021), which are ideal for achieving uniform and fine coatings. Although aerosol-assisted coating can help to form a uniform film quickly, the final deposited area is limited to the spray nozzle space. Printing technology could use a designed program to control the moving route during the printing process. A combination of aerosol-assisted coating and printing technology thus allows for continuous and

automatic fabrication of PEM membranes, making the process more amenable to industrial deployment.

With such an approach, to truly enable tailored design and reproducibility, a deeper fundamental understanding of the PEM membrane formation mechanism is needed. The formation of PEM membranes through spray-printing methods involves a multistep process, including aerosol deposition, formation of the PE layer, and sequential assembly of multilayers. The spray process itself encompasses several dynamic steps: aerosolization of the PE solution, transport of droplets through the air, their impingement onto the substrate, potential resuspension or bouncing of droplets, and finally, droplet spreading and deposition (Zhao et al., 2022). Each of these stages can significantly affect the uniformity and thickness of the resulting PE layer. The characteristics of each deposited PE layer, governed by the spray dynamics, have a cumulative effect on the multilayer architecture, thereby impacting the properties of the PEM membrane.

Furthermore, the supply side (a promising candidate material of comparative advantage, here as tunable PEM membranes based on different PE pairs) needs to be strategically coordinated with the demand side (specific requirements of water and wastewater treatment). Advancing our fundamental understanding of PEM membrane design and fabrication is essential, enabling a fit-for-purpose strategy tailored to the specific requirements of the targeted water or wastewater treatment. The functionality of PEMs can be precisely modulated by altering the type of PE pairs (Reurink et al., 2020; Zhou et al., 2025) used and/or adjusting the number and sequence of bilayers (Liang and Lin, 2021). For instance, selecting PEs with stronger electrostatic or hydrogen bonding interactions can improve membrane stability in harsh conditions (de Grooth et al., 2015; Elshof et al., 2020). Meanwhile, altering layer architecture can tune selectivity, permeability, and antifouling characteristics, allowing for customized solutions to target contaminants in diverse water matrices

(Bashir et al., 2025; Wang et al., 2021). However, a critical gap remains in establishing predictive design principles that link molecular-level membrane structure to application-specific separation performance. Without this, the development of PEMs often relies on empirical trial-and-error methods, limiting the efficiency and scalability of tailored membrane solutions.

Finally, there exists an issue in the post-fabrication process that is particularly critical for LbL assembly of the PEM membrane. During and after LbL assembly, the solvent evaporates (Zhao et al., 2022), and the PEM membranes undergo a drying process. This drying step is not trivial because solvent evaporation can cause film compaction (Lösche et al., 1998; V Klitzing, 2006), densification (Déjugnat et al., 2007), or even a structure collapse (Liu et al., 2019; Zverina et al., 2020), depending on drying rate and ambient conditions. These issues can significantly impact membrane performance. Therefore, understanding and controlling the drying process is essential for ensuring consistent membrane quality and functionality.

1.3 Research Objectives

The overarching goal of this thesis is to develop an aerosol-assisted printing (AAP) method for PEM fabrication and establish the fabrication-structure-performance relationships to develop PEM NF membranes with tunable permeability and selectivity. The first objective of this thesis is to investigate the impact of different PEs on PEM membranes. An as-developed AAP system comprises a commercial 3D printer and a Collison nebulizer. The different PEs' spray dynamics (including aerosolization, droplet size distribution, and transport) and the molecular interactions after aerosol deposition are investigated to understand their roles in multilayer formation and membrane functionality.

After choosing the proper PE pair that achieves NF-level filtration performance with minimal fabrication time and material consumption, the second objective focuses on tailoring the PEM

membrane structure by varying two key factors: the printing scan number in each PE layer and the bilayer number. The deposition behavior of PE aerosols is connected to PE layer growth and PEM assembly, and ultimately, these structural features determine the membrane's filtration performance. These insights enable precise control over PEM membrane structure and performance for targeted separation applications.

The third objective of this thesis is to investigate the distinct drying impact on the PEM and the substrate during and after assembly, and to provide effective strategies to prevent the associated structural defects and changes in filtration performance. This involves first understanding the water evaporation process, followed by evaluating the impact of drying on the structure and separation performance of PEM membranes, and ultimately decoupling the respective contributions of the PEM and the substrate to the membrane's overall structure and filtration performance. Isolating the changes in the PEM layer and the substrate provides a clearer understanding of the drying influence on membrane performance and assists in identifying effective strategies to mitigate drying-related effects.

1.4 Thesis Organization

This thesis includes six chapters. It opens with an overview of membrane filtration technology, emphasizing key scientific and engineering challenges that remain unresolved. The objectives of this doctoral work are defined in alignment with the identified knowledge gaps and technical needs.

Chapter 2 of the literature review explores the fundamentals of PEM membranes, starting with an overview of PE, PEM, and polyelectrolyte complex (PEC). The chapter progresses to the assembly methods used to create PEM, including dip-coating, spin-coating, spray-coating, and inkjet printing techniques, each with its unique advantages, disadvantages, and applications in membrane fabrication. Furthermore, previous works on membrane fabrication methods are

discussed to emphasize the need for scalability. In this context, AAP emerges as a promising approach, showcasing its principles and benefits in achieving precise and uniform membrane structures, thereby addressing the challenges of scaling up membrane fabrication effectively. Finally, this chapter discusses the application of PEM NF membranes in water and wastewater treatment, detailing the separation mechanisms involved and highlighting real-world applications that illustrate their effectiveness in purifying water resources. This thorough exploration emphasizes the crucial role of PEM in advancing membrane technology and promoting environmental sustainability.

Chapter 3 demonstrates the use of the AAP method to prepare the PEM membranes. An AAP system is built by a commercial 3D printer with a Collison nebulizer. The dynamic behavior of droplets during their generation and deposition (e.g., droplet size and deposition efficiency) is analyzed to elucidate the formation mechanisms of different PEM membranes. The influence of spray dynamics of different PEs, including aerosolization, droplet size distribution, and droplet transportation, as well as molecular interactions between different PEs following aerosol deposition, on multilayer formation and membrane performance is investigated. This systematic investigation highlights the coupled effects of spray dynamics and PE molecular interactions on PEM membrane structure and performance.

Chapter 4 firstly investigates the relationship among the PE droplet deposition, PE layer growth, and PEM assembly. The aerosolization and transportation of PE droplets are characterized by both in-line measurements (aerosol particle sizing and velocity) and off-line measurements (state-of-the-art microscopy), and are modeled using COMSOL simulation. Moreover, various PEM membranes, which are adjusted by printing scan and bilayer number, feature tunable structures and separation properties tailored for diverse water treatment applications. This chapter provides

valuable mechanistic insights into the formation of PEMs and the precise structural adjustments achievable through AAP techniques, thereby enabling scalable manufacturing and broad applications of PEM NF membranes.

Chapter 5 investigates the coupled, time-dependent responses of the PEM and substrate during the drying process. These responses include changes in water content, structural changes, and variations in the separation performance of the individual PEM film, the substrate, and the overall membrane. These analyses provided valuable mechanistic insights into the distinct drying responses of the PEM and the substrate, as well as effective strategies for mitigating performance change.

Finally, Chapter 6 summarizes the key research findings of this thesis and outlines its novel contributions and impacts. The concluding remarks address potential future research directions and discuss the implications of these findings for the rational design and application of PEM membranes in practical scenarios.

Chapter 2. Literature Review

2.1 Polyelectrolyte-Based Coatings

PEs are macromolecules bearing ionizable groups and have garnered significant attention due to their broad applicability in various fields, ranging from biomedicine to materials science (DuChanois et al., 2023; Finbloom et al.; Xiong et al., 2023; Yu et al., 2018). Ionized PEs in solution can interact with oppositely charged counterparts to form polyelectrolyte complexes (PECs). Further extending their functionality, the LbL assembly of PEs enables the fabrication of PEMs, highly ordered thin films with precise control over composition and thickness.

2.1.1 Polyelectrolytes

PEs are ionizable polymers that dissociate in aqueous solutions to carry a net electrical charge and are broadly categorized as either polycations or polyanions. These macromolecules are composed of two key structural elements: the polymeric backbone and the ionic functional groups. Among the most common functional groups are quaternary ammonium-based and amine cationic moieties, typically found in polycations, and organic acid-based anionic groups, such as carboxylates or sulfonates, present in polyanions. Polycations, which carry positive charges, include widely used materials such as poly(diallyldimethylammonium chloride) (PDDA), poly(allylamine hydrochloride) (PAH), and polyethyleneimine (PEI). The chemical structures of the mentioned PEs are shown in Figure 2.1. PDDA is a linear PE featuring permanently charged quaternary ammonium groups, providing strong cationic properties independent of pH. PEI contains primary, secondary, and tertiary amines, giving it pH-dependent chargeability, and exists in both linear and branched forms. PAH, another linear PE, consists of primary amine groups that protonate in acidic conditions. Polyanions carry negative charges and typically include poly(sodium 4-styrenesulfonate) (PSS) and poly(acrylic acid) (PAA). PSS, a strong polyanion,

contains sulfonate groups that are ionized across a broad pH range, while PAA is a weak polyanion with pH-sensitive carboxylic acid groups.

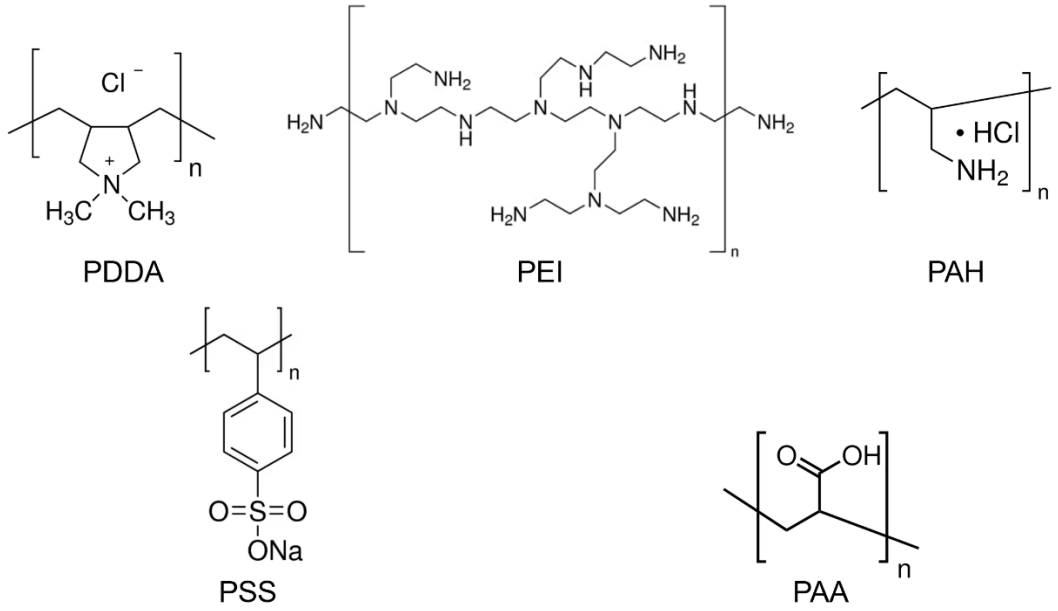

Figure 2.1 Chemical structures of polyethyleneimine (PEI), poly (allylamine hydrochloride) (PAH), poly(diallyldimethylammonium chloride) (PDDA), poly(sodium 4-styrenesulfonate) (PSS), and poly(acrylic acid) (PAA).

2.1.2 Polyelectrolyte Complex (PEC)

PECs are formed through the spontaneous association of oppositely charged PEs, driven primarily by electrostatic interactions and the entropic gain from counterion release (Fu and Schlenoff, 2016; Guo et al., 2009; Rathee et al., 2018). Although this thesis focuses on the layer-by-layer assembly of PEMs, a foundational understanding of PEC formation is essential, as the same electrostatic principles govern both complexation and multilayer buildup. The formation

mechanisms, structural characteristics, and applications of PECs lay the groundwork for subsequent discussion on PEM architecture and performance.

The oppositely charged PEs interact predominantly via electrostatic attraction, and secondary interactions such as hydrogen bonding, van der Waals forces, and hydrophobic effects (Guo et al., 2009; Thünemann et al., 2004). The theoretical and computational studies, notably by Solis and De La Cruz (2000) and later by Ou and Muthukumar (2006) have highlighted the central role of entropy in PEC formation. The entropic contribution arises primarily from the release of bound counterions during complexation, which significantly increases the system's overall disorder. For strong PEs, the free energy of complexation is dominated by the entropic gain from counterion and water release (Fu and Schlenoff, 2016; Gummel et al., 2007), whereas for weak PEs, an enthalpic gain from electrostatic attraction between oppositely charged chains governs polymer interactions and chain conformations (Mitra and Kundagrami, 2023; Ou and Muthukumar, 2006).

The structure of PECs is commonly described by two conceptual models: the ladder-like model and the scrambled egg model (Figure 2.2) (Manisha and Devendra, 2017; Michaels and Miekka, 1961). The ladder-like structure arises when PEs with significantly different molecular sizes and weakly charged groups associate in an ordered, sequential manner (Hartig et al., 2007). This configuration follows zippering mode, where the initial pairing of ionic sites promotes successive neighboring interactions along the polymer chain, leading to a regular, stepwise assembly reminiscent of a molecular ladder. The scrambled egg structure typically forms when multiple polymer chains with high charge density and comparable molecular weights become extensively entangled. This model represents disordered, densely aggregated complexes that result from the strong electrostatic interactions between highly charged PEs, often precipitating as insoluble materials under nearly 1:1 charge stoichiometry. The structure and final state of PECs, ranging

from colloidally stable dispersions to coacervate phases, are strongly influenced by factors such as the charge ratio between components, the molecular weight of the PEs, and the surrounding solution conditions (Manisha and Devendra, 2017). Depending on their structural characteristics, PECs lend themselves to a wide range of applications, including the formation of hydrogels (Chen et al., 2004; Gao et al., 2013) and nanoparticle-based delivery systems (Paltrinieri et al., 2017), as well as functional coatings and NF membranes (Ji et al., 2010; Zhao et al., 2011).

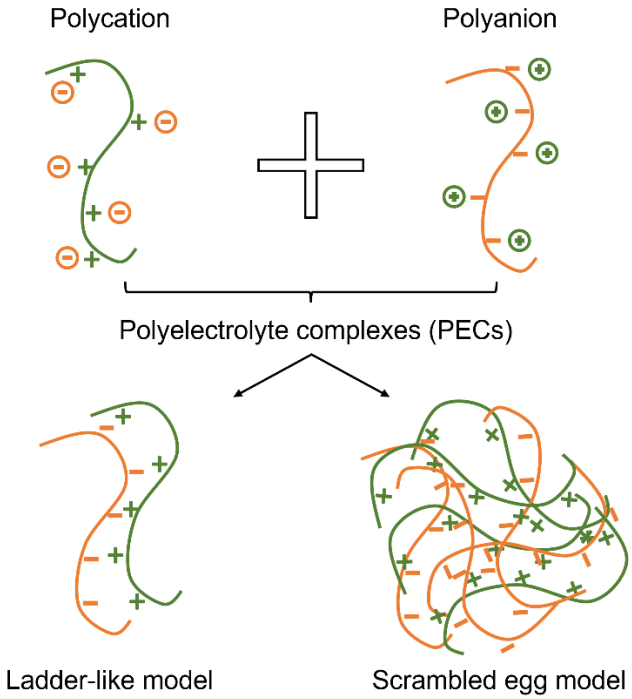

Figure 2.2 Schematic structure of PECs: ladder-like model and scrambled egg model.

2.1.3 Polyelectrolyte Multilayer

The formation of PEM films relies on sequential electrostatic adsorption of polycation and polyanion onto a charged substrate (Figure 1.1). When the substrate is immersed in a PE solution, electrostatic interactions drive the adsorption of polymer chains carrying opposite charges, forming a thin monolayer. Due to steric constraints and the spatial distribution of surface charges,

this initial adsorption does not result in complete charge neutralization. As a result, some surface charges remain uncompensated, requiring the adsorption of additional PE chains to achieve further charge compensation. This process often leads to overcompensation or charge inversion. The resulting layer includes structural features, such as loops and tails, that extend into the solution, carrying excess charge. This excess charge eventually prevents further adsorption of the same PEs due to electrostatic repulsion, thereby self-limiting the growth of a single layer and preparing the surface for adsorption of the next, oppositely charged layer (Izumrudov et al., 2018).

The alternating deposition of polycations and polyanions results in the stepwise buildup of PEM films. Initially, film growth often follows an exponential regime, attributed to diffusion of PEs into previously deposited layers during adsorption. This vertical interpenetration and accumulation lead to rapid increases in thickness with each additional bilayer. Over time, as the internal structure becomes more compact and diffusion is hindered, the system transitions into a linear growth regime, where each deposition cycle contributes a fixed increment to the overall film thickness (Azinfar and Helm, 2023). In dip-coating methods, where substrates are repeatedly immersed and withdrawn from PE solutions, PEM growth can also exhibit parabolic behavior. This is often due to mismatches in the linear charge densities of the polycation and polyanion, leading to uneven adsorption rates and variations in charge compensation across the layers (Azinfar and Helm, 2023; Azinfar et al., 2021).

Numerous parameters, including PE type (Mermut et al., 2003; Schlenoff and Dubas, 2001), solution ionic strength (Klitzing, 2006; Salomäki and Kankare, 2008), solution pH (Emonds et al., 2022; Shiratori and Rubner, 2000; Yoo et al., 1998), and PE molecular weight (MW), have been reported to affect the properties of PEMs (Towle et al., 2020). These factors enable the production of thin films with engineered functionality for various membrane applications, including ion

selectivity, fouling control, stability against harsh wastewater, contaminant removal from water, and responsiveness. These tunable properties highlight the versatility of PEMs, making it essential to carefully tailor the fabrication process to achieve the desired structural and functional characteristics.

2.2 Polyelectrolyte Multilayer Assembly Method

The assembly of PEMs is typically achieved through an LbL technique, which involves the sequential adsorption of oppositely charged PEs onto a substrate. LbL thin-film assembly has attracted the interest of many researchers over the last few decades due to its ability to precisely control film thickness and utilize various materials for coating both flat and particulate substrates. Dip-coating, spin-coating, spray-coating, and inkjet printing (Figure 2.3) are the commonly used methods for LbL assembly of PEM films.

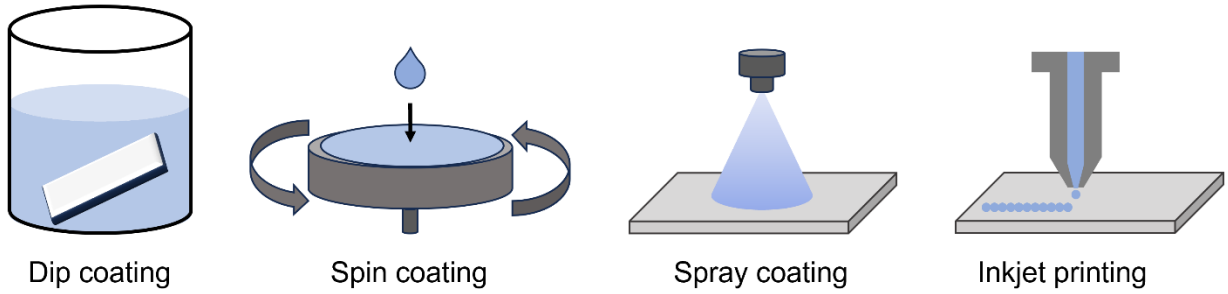

Figure 2.3 Schematic illustration of dip coating, spin coating, spray coating, and inkjet printing.

2.2.1 Dip Coating

Dip-coating is the most extensively used LbL method. Choi et al. (2015) employed a molecular LbL assembly strategy to create a highly cross-linked PE selective layer by alternating deposition

of reactive polymers on a porous substrate. The PDDA/PSS membranes show 96% rejection of SO_4^{2-} along with a water flux of 13.9 L $m^{-2} \cdot h^{-1} \cdot bar^{-1}$. Its filtration performance is comparable to that of the commercial NF membrane (NF 270) (Malaisamy and Bruening, 2005). This study shows that LbL can be used to fabricate an effective PEM NF membrane with high ion rejection.

One of the critical parameters in the LbL self-assembly process is the dipping time. PEs diffuse from the bulk solution to the vicinity of the oppositely charged surface and deposit onto it. Counterions also need time to build complexation on the charged surface. The best dipping time is determined by the combined effects of the diffusion speed of PE molecules in solutions, the degree of charge overcompensation of the PE onto the substrate, and the time of constructing a cross-linked structure among the charged groups (Zhang et al., 2008). At each stage of typical dip coating, the film is in contact with the PE solutions (at least 15 min) (Decher et al., 1992; Dubas and Schlenoff, 1999) and is rinsed by fluids long enough to produce a kinetically trapped structure, thus leading to a long membrane preparation time. The conventional dip-coating method is not suitable for large-scale membrane fabrication because it is time-consuming, labor-intensive, and wasteful of raw materials due to its high consumption of polymer solutions (Richardson et al., 2015). Scaling up the membrane fabrication process is crucial for advancing real-world applications. In addition, the cyclic nature of the dipping process can lead to carryover from the rinse bath to the preceding PE solution, inducing an unacceptable change in solution pH, which deteriorates the deposition efficacy and quality (Krogman et al., 2007). It is also difficult to process hydrophobic substrates or (nano)materials with even lower diffusivity.

2.2.2 Spin Coating

The LbL assembly via spin coating utilizes a standard process where a substrate is rotated to enable uniform material deposition (Chiarelli et al., 2001; Cho et al., 2001). Spin coating

accelerates the assembly process, enabling each layer to be formed within about 30 s (Cho et al., 2001). The properties of the material solutions, such as viscosity, concentration, thixotropy, and surface tension, influence film characteristics (Richardson et al., 2015). Compared with the dip-coating method, it is easier to form a homogeneous film by spin-coating (Cho et al., 2001). This is due to a combination of factors, including electrostatic interactions that promote polymer adsorption and rearrangement, as well as centrifugal, air shear, and viscous forces that cause the desorption of weakly bonded polymers and dehydration of the films. The shear forces existing in spin coating facilitate the production of thinner, highly ordered membranes compared with dip-coating assembly. In particular, the thickness of polymer layers prepared by spin coating is strongly influenced by the rotation rate, with faster speed yielding thinner coating (Chiarelli et al., 2001).

Spin-coating significantly accelerates the PEM assembly process and is particularly effective for producing uniform, ultrathin films with precise thickness control. The rapid rotation of the substrate spreads the PE solution evenly across the surface, while excess material is expelled by centrifugal force, enabling fast deposition and drying in a single step. However, despite these advantages, spin-coating presents several limitations in terms of scalability and substrate compatibility. One major constraint is its suitability primarily for small, planar substrates; as the substrate size increases, higher spin speeds are required to maintain uniform film formation, which may exceed practical or mechanical limits. Moreover, the technique is poorly suited for nonplanar or textured surfaces, as the centrifugal forces tend to cause uneven coating or solution runoff. These limitations restrict the broader applicability of spin-coating in industrial membrane fabrication, especially for large-area or three-dimensional geometries.

2.2.3 Spray Coating

In spray LbL assembly, polymer solutions are atomized into droplets, which are sprayed onto the substrate to form layered films. Spray assembly is much faster than dip-coating assembly (Izquierdo et al., 2005) and spin assembly (Dierendonck et al., 2014; Schaaf et al., 2012). Spray-assisted approaches are fast in terms of mass transfer and can be controlled to reach various targets by adjusting spray parameters.

Schlenoff et al. (2000) published the first report describing spray-assisted LbL build-up of PEM. The spray coating method has received increasing interest from researchers since 2005. Porcel et al. (2005) further used spray-assisted LbL assembly of PEM onto a vertically held substrate, resulting in continuous film growth. Spray-assembled PEM as an NF or RO membrane was only demonstrated in the last decade. In 2014, the Kentish group demonstrated a RO membrane with an active layer of PAA and PAH via spray coating (Cho et al., 2014). The cross-linked membrane can reject up to 80% $CaCl_2$ and 50% NaCl, with a water flux of 1.1-2.3 L $m^{-2} \cdot h^{-1} \cdot bar^{-1}$. The spray technique was further used to deposit an ultrathin (ca. 70 nm) active layer consisting of PAH and PSS, which showed 94% rejection of NaCl with a permeate flux of 0.75 L $m^{-2} \cdot h^{-1} \cdot bar^{-1}$ (Li et al., 2018), showing a very narrow separation regime due to dense deposited layers.

Spray coating methods are widely employed for membrane surface modification due to their compatibility with diverse substrate types and their ability to deposit various materials. Tang et al. (2013) used an automatically controlled sprayed LbL assembly method to build PEI/PAA multilayers onto a tubular ceramic macroporous substrate, achieving rapid coating of large areas. The composite membrane consisting of five PEI/PAA bilayers had a flux of around 10.0 L $m^{-2} \cdot h^{-1} \cdot bar^{-1}$ and a methyl blue rejection of 99%. In addition to polymer solutions, various nanomaterials, such as carbon nanotubes and graphene oxide, can be incorporated into the active layer through

the spray coating. Morelos-Gomez et al. (2017) presented a graphene-based membrane prepared using a spray coating. The as-synthesized membranes were robust enough to withstand strong crossflow shear for a prolonged period (120 h) while maintaining near 85% NaCl rejection and 96% rejection for an anionic dye. The spray assembly is a quick method for coating large or non-planar substrates and is increasingly recognized as a highly relevant technology for industrial applications.

2.2.4 Inkjet Printing

Inkjet printing has gained significant attention across a range of scientific fields, including electronics (Saleh et al., 2017), biosensing (Molazemhosseini et al., 2017), catalysis (Tempel et al., 2010), and biomedical engineering (Barui, 2021). This technology is considered a cost-effective and environmentally friendly method, due to its minimal material consumption and reduced chemical waste (Badalov et al., 2015; Fathizadeh et al., 2017). By enabling the digital patterning of deposited materials, inkjet printing facilitates the construction of well-organized membrane architectures with defined structures and surface properties. Moreover, the process is cost-effective and minimizes material waste, making it an efficient and environmentally friendly alternative for membrane manufacturing.

The inkjet printing technique has been applied to the fabrication of PEM membranes. Gao et al. (2016) used inkjet printing to form PAH/PSS NF membranes with a water permeability of 2.8 L $m^{-2} \cdot h^{-1} \cdot bar^{-1}$ and a $MgCl_2$ rejection of 75.5%. Wang et al. (2023) employed a composite ink of PEI and graphene oxide to fabricate a NF membrane via inkjet printing. The resulting membrane exhibited water permeability of 4.0 L $m^{-2} \cdot h^{-1} \cdot bar^{-1}$ and $MgCl_2$ rejection of 64.5%. The inkjet printing technique was also applied for the fabrication of organic solvent nanofiltration (OSN) PEM membranes, with single-walled carbon nanotubes incorporated into the PEI/PSS multilayer

(Wang et al., 2022a). The fabricated membrane exhibited permeances of 2.52, 4.21, 1.21, and 4.75 L $m^{-2} \cdot h^{-1} \cdot bar^{-1}$ for ethanol, methanol, isopropyl alcohol, and acetone, respectively, along with Rose Bengal rejection exceeding 98%. The relatively low permeability was mainly caused by the formation of a thick and dense active layer, which resulted from the large droplet size (ca. 25 μm) (Shin et al., 2023; Wijshoff, 2018) produced by the inkjet.

Although inkjet printing offers a promising approach for membrane fabrication, it still presents several limitations that may hinder its broader application. The large ink droplet size not only results in excessive material deposition but can also lead to poor surface morphology of the printed films, primarily due to the well-known "coffee-ring" effect, which arises from different time scales between evaporation and movement of inks (He and Derby, 2017). The choice of printable inks remains a key limitation in inkjet printing (Martin and Hutchings, 2012). Thermal drop-on-demand (DOD) printers primarily use water-based inks, while piezoelectric DOD printers accommodate both water- and solvent-based inks but require control of ink viscosity (20-40 mPa·s) and surface tension (<40 mN m^{-1} at 25 ℃) (Beeson, 1998). Additionally, organic solvents like n-hexane can damage the print head, and piezoelectric printers are costly due to the expensive piezoelectric components (Sakai, 2000). Moreover, nozzle clogging can disrupt stable ink ejection from the print head during the printing process (Smith and Shin, 2012). If these challenges can be effectively addressed, inkjet printing is a highly promising technique for membrane fabrication and surface modification.

2.2.5 Comparison of the Polyelectrolyte Multilayer Assembly Methods

The LbL assembly methods of PEM membranes include dip coating, spin coating, spray coating, and inkjet printing, each with distinct trade-offs in precision, scalability, and application suitability. Comparison of the PEM assembly methods, including dip coating, spin coating, spray coating, and

inkjet printing, is shown in Table 2.1. Dip coating, the most conventional method, relies on sequential substrate immersion in PE solutions with rinsing steps, offering simplicity and compatibility with complex geometries substrates but suffering from low throughput and poor industrial scalability. Spin coating enables rapid, uniform thin-film deposition via centrifugal force, but its restriction to flat substrates and significant material waste limit its utility for large-scale or resource-intensive applications. Spray coating utilizes aerosolized PE solutions to achieve quicker mass transfer and adaptability to irregular surfaces, but lacks control over chemical droplet size, uniformity, and velocity. Inkjet printing enables programmable patterning for well-defined membrane architectures, but its large droplets lead to excessive deposition and poor surface morphology.

Table 2.1 Comparison of the PEM assembly methods, including dip coating, spin coating, spray coating, and inkjet printing.

Feature	Dip Coating	Spin Coating	Spray Coating	Inkjet Printing
Precision	Low	Moderate	Moderate	High
Scalability	Moderate	Poor	Good	Moderate
Speed	Slow	Fast	Fast	Slow (drop-by-drop deposition)
Material Waste	High	High	Moderate	Low
Cost	Low (simple setup)	Moderate (spin coater)	Moderate (spray system)	High (printer, ink)

2.3 Aerosol-Assisted Printing for Membrane Fabrication

The AAP has emerged as a promising technique for the fabrication of membrane materials, offering a scalable, efficient, and precise method for depositing functional layers. This approach involves the generation of aerosolized droplets containing various materials, which are then directed onto a substrate to form thin films. By finely tuning parameters such as droplet size and printing pattern, AAP enables controlled deposition over large areas, including nonplanar and porous surfaces.

2.3.1 Aerosol

Aerosol is a suspension of fine solid particles or liquid droplets in gas (typically air) (Hinds, 1999). Natural examples include fog (liquid droplets in air), smoke (solid particles in air), or mist. In manufacturing, engineered aerosols are widely employed for controlled and precise material deposition. A key method for producing aerosols is nebulization, which involves converting a liquid into a fine mist through various techniques. Common nebulization methods include pressure-driven (pneumatic) nebulizers and ultrasonic nebulizers. These nebulizers are primarily designed to ensure a predictable and reproducible aerosolization performance.

Pressure nebulizers generate aerosols by forcing a liquid through a narrow orifice under high pressure, typically using a carrier gas or centrifugal mechanism to break the liquid into fine droplets. Taking the Collison nebulizer as an example, it can generate aerosols with droplet sizes in the range of 1-5 μm (Feng et al., 2021; Wang et al., 2012). Ultrasonic nebulizers employ high-frequency sound waves to induce periodic vibrations in a liquid, leading to the disruption of the liquid surface and the formation of fine droplets, typically around 5 μm in diameter for water at a frequency of ca. 2 MHz (Bang and Suslick, 2010). In contrast to conventional spray systems such as spray guns and airbrushes, which generate larger and more heterogeneous droplets (30-50 μm)

(Chen and Lin, 2009; Scardaci et al., 2011), these nebulizers offer superior precision in droplet size and deposition, making them especially suitable for applications that demand high control and uniformity.

2.3.2 Aerosol Deposition Principle

The spraying process consists of aerosolization, droplet transport, and deposition. In this process, the polymer solution is first atomized into ultrafine, nearly monodisperse droplets through the intense shear forces generated between compressed air and liquid at the nozzle. The viscosity and surface tension of different solutions are critical factors in the atomization process during nebulization (Mc Callion et al., 1996; McCallion et al., 1995; Steckel and Eskandar, 2003). During nebulization, an increase in solution viscosity results in greater liquid retention within the siphon, effectively reducing the diameter of the jetting channel. This constriction elevates the suction pressure (Feng et al., 2021) and accelerates the gas flow through the nozzle. The resulting higher gas velocity enhances atomization efficiency, causing the liquid stream to break up into finer droplets (Davis, 1978). The surface tension of the solution significantly influences the breakup dynamics of the liquid jet during atomization. Higher surface tension enhances the cohesive forces within the liquid, making the jet more resistant to disruption and resulting in larger droplets. As a result, more energy is required to disrupt the liquid stream, leading to the formation of larger droplets and less efficient aerosol generation. Conversely, lower surface tension facilitates jet disintegration, promoting the formation of smaller aerosol droplets (Modi et al., 2023).

The effluent stream of polymer aerosols was directed towards a flat membrane surface, causing the flow to deflect and create a curvilinear flow shape. The large droplets whose inertia is too high to follow the streamlines could collide (impact) on the flat plate and get deposited, while smaller droplets flow along the streamline and do not reach the substrate. The inertial impaction of particles can be characterized by the Stokes number (S_{tk}) (Eq. 2.1) (Agranovski, 2011). The S_{tk} is the ratio

of the stopping distance to a characteristic dimension. The stopping distance refers to the distance a particle will travel before it comes to a complete stop when subjected to a sudden change in the fluid velocity or direction. The characteristic dimension of the system refers to a length scale that is representative of the physical dimensions of the flow domain or the obstacles present in the flow. The S_{tk} is considered as the indicator of a droplet's tendency to deposit on a surface (Friedlander and Smoke, 2000). A droplet with a low S_{tk} follows the fluid streamlines, while a particle with a larger S_{tk} can be dominated by its inertia and continues along its initial trajectory.

$$S_{tk} = \frac{\rho_P {d_P}^2 V}{18\mu L} \tag{2.1}$$

where d_p, ρ_P, and V are the droplet diameter, density, and velocity, respectively, μ is the dynamic viscosity of the carrier gas, and L is the characteristic length (jet diameter).

Based on the S_{tk} (Eq. 2.1), the aerosol size and velocity are the two main factors affecting the inertial deposition efficiency. Larger droplets possess greater momentum, resulting in larger deposition mass on the substrate. Similarly, increasing droplet velocity enhances deposition efficiency by improving the likelihood of direct impingement. This velocity can be modulated by adjusting the nebulizer pressure because higher pressure generates a faster carrier gas stream and accelerates the droplets. However, excessively high velocities may cause droplet splashing or rebound, potentially compromising deposition efficiency and film uniformity (Agranovski, 2011). Therefore, optimizing both droplet size and velocity is essential for achieving consistent, high-mass deposition while maintaining control over coating morphology and thickness.

2.3.3 Aerosol-Jet Printing

The AAP is an advanced, versatile technique that enables the precise deposition of functional materials by delivering aerosolized droplets through a nozzle onto a substrate using a designed printing pattern (Figure 2.4). This approach allows for controlled, non-contact patterning and thin-

film formation over a wide range of surfaces, including flat, curved, or porous substrates. Aerosol jet printing, developed in the early 1990s, consists of two main components: an atomization system (nebulizer) and a motion control platform (Wilkinson et al., 2019). The nebulization process typically utilizes either pneumatic or ultrasonic methods to generate fine aerosols. This noncontact, maskless, direct-write technique allows for the precise deposition of functional or multifunctional materials in aerosol form through a nozzle positioned at a variable stand-off distance (typically 1-5 mm) from the substrate (Seiti et al., 2023). The process produces well-defined patterns with feature sizes ranging from as small as 15 μm to several centimeters in width and down to 0.1 μm in thickness (Seiti et al., 2023). These capabilities allow aerosol jet printing to fabricate a diverse range of electronic devices, including transistors, sensors, and organic light-emitting diodes (Jones et al., 2010; Kim et al., 2013; Salary et al.).

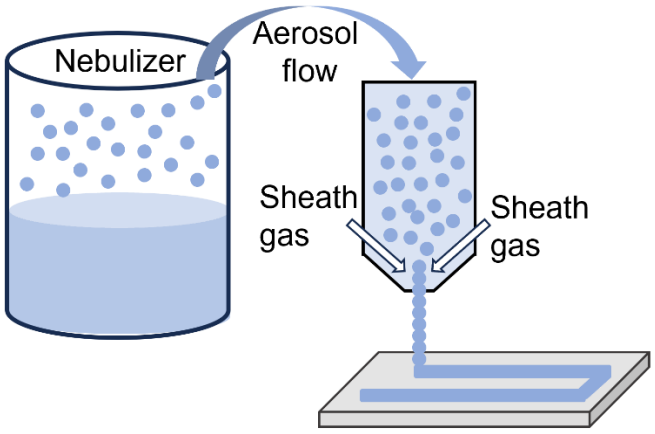

Figure 2.4 Schematic illustration of aerosol-jet printing.

While aerosol jet printing is well-suited for the fabrication of high-resolution components and microsensors, its application in filtration membrane fabrication remains limited. Aerosol jet printing is a serial, point-by-point deposition process, which results in low throughput and makes it inefficient for covering large surfaces. The narrow deposition width of the aerosol stream,

typically tens to hundreds of micrometers (Seiti et al., 2023), is inefficient for membrane manufacturing. One feasible solution to this limitation is to eliminate the aerodynamic focusing sheath gas, which is primarily responsible for tightly collimating the aerosol stream into a fine line. Eliminating the focusing sheath gas allows the aerosol stream to expand significantly, increasing deposition coverage.

2.4 Polyelectrolyte Multilayer Nanofiltration Membrane Application in Water and Wastewater Treatment

In recent years, PEM membranes have been increasingly investigated for their ability to remove a wide range of contaminants from complex aqueous environments, including salts, heavy metals, organic micropollutants, and pathogens. Their tunable chemical functionality, hydrophilicity, and surface charge make them especially suitable for addressing the diverse challenges associated with water purification. The fundamental separation mechanisms in PEM-based NF primarily involve size exclusion, Donnan exclusion, and dielectric exclusion, each contributing differently depending on the membrane structure and feed composition.

2.4.1 Separation Mechanisms

Solute transport through NF membranes is mainly governed by several fundamental mechanisms that are critical for enhancing membrane selectivity. Among these, size exclusion is the most basic and widely recognized principle, where larger solutes are more effectively rejected due to their inability to pass through the membrane pores. For uncharged solutes, the steric hindrance pore model is commonly applied to estimate membrane pore size (Deen, 1987; Nghiem et al., 2004). In this model, the NF membrane is represented as an array of cylindrical capillaries with uniform radii, and solute transport is governed by the degree of steric hindrance encountered within these pores.

In NF membranes, the pore diameters are often smaller than the Debye length of the electric double layer, meaning that electrostatic interactions within the pores become significant. The interactions between charged solutes and the membrane surface strongly influence separation behavior. To describe these effects, the widely recognized Donnan Steric Pore Model (DSPM) (Bowen et al., 1997), developed in 1997, combines steric hindrance with Donnan exclusion as fundamental mechanisms governing ion transport through NF membranes. PEM membranes offer a distinct advantage through their tunable surface charge, which can be precisely controlled by selecting the outermost layer. When a polycation forms the top layer, the membrane surface becomes positively charged; conversely, a polyanion top layer imparts a negative surface charge. This ability to control surface charge provides a powerful means of tailoring membrane selectivity through electrostatic interactions. Such tuning is especially effective for differentiating between monovalent and multivalent ions, as the strength of electrostatic repulsion or attraction can be selectively adjusted to favor or hinder the transport of specific ionic species.

Dielectric exclusion works alongside Donnan exclusion to influence ion transport in NF membranes. Dielectric exclusion primarily stems from the difference in the dielectric environment between the bulk solution and the membrane pores. Within the confined space of the pores, the dielectric constant of the solvent is reduced, which means there is an energy barrier to the solvation of ions into the pores. This effect significantly enhances salt rejection by limiting the transport of charged species through the membrane. This mechanism was first proposed by Born (1920). Bandini and Vezzani (2003) further proposed that dielectric exclusion also results from the difference in dielectric constants between the membrane material and the solvent inside the pore, by which polarization charges are generated. Building on this understanding, they enhanced DSPM by integrating both the solvation energy barrier and polarization charges, resulting in the DSPM-

DE model. This advanced model represents the current state of the art in accurately describing the filtration performance of NF membranes.

2.4.2 Water and Wastewater Treatment

Hard water is common throughout the world, which contains high levels of Ca^{2+} or Mg^{2+} (Ouyang et al., 2008). A promising approach to mitigate hardness in surface and groundwater is selectively removing these multivalent ions from the feedwater while allowing monovalent ions like Na^{+} and Cl^{-} to permeate. In NF, ion rejection mainly occurs through Donnan exclusion and steric exclusion. PEM NF membranes, especially those terminated with polycations, exhibit enhanced rejection of divalent cations due to their positively charged surface, making them a valuable tool for controlling scaling in membrane systems. Cheng et al. (2018a) fabricated PDDA/PSS PEM membranes for effective removal of divalent cations from feedwaters and reported 97% rejection of Mg^{2+} with Na^{+}/Mg^{2+}selectivity greater than 30. Another researcher used PAH/PSS PEM to prepare ion-selective NF membranes, which exhibited 95% rejection of $MgCl_2$ along with a Na^{+}/Mg^{2+} selectivity of 22 (Ouyang et al., 2008).

A wide range of trace organic compounds, including pharmaceuticals, personal care products, and environmental estrogenic hormones, have been increasingly detected in surface waters. PEM NF membranes have gained attention for their potential in removing these emerging micropollutants. Most micropollutants have molecular weights between 100 and 1000 Da, which fall within or above the molecular weight cutoff (MWCO) range of PEM NF membranes, enabling their efficient rejection. Wang et al. (2021) fabricated PEM NF membranes with a pore size of 0.94-1.06 nm using PDDA and PSS. These membranes can reject up to 90% perfluoroalkyl substances (perfluorooctanoic acid and perfluorooctanesulfonic acid) and antibiotics (amoxicillin trihydrate and tetracycline hydrochloride. Cheng et al. (2018b) coated gallic acid and PEI via LbL to fabricate a loose NF membrane for antibiotic treatment, achieving 96.7% rejection of

Azithromycin. Zhou et al. (2025) showed the feasibility of using a PEM NF membrane to remove micropollutants in real aquaculture water through membrane separation. The researchers compared three types of PEM membranes to treat real aquaculture water containing micropollutants. PAH/PSS PEM membranes with an average pore size of 0.58 nm and MWCO of 179 Da showed above 95% rejection to all tested micropollutants (testosterone, tetracycline, oxytetracycline, sulfadiazine, sulfamethoxazole, and norfloxacin). PDDA/PSS membranes and poly(vinylbenzyltrimethylammonium chloride) (PVB)/PSS membranes showed lower micropollutant rejection than PAH/PSS membranes due to their larger pore sizes. Among the various factors influencing micropollutant removal, membrane pore size was identified as the most critical. Recent studies have also highlighted operating pressure as another major factor affecting micropollutant removal, while membrane surface charge (zeta potential) and solution pH were found to have moderate impacts (Xu et al., 2024).

Overall, PEM NF membranes have demonstrated remarkable versatility in addressing a wide range of challenges in water and wastewater treatment. Their tunable surface charge and nanometer-scale structural control enable efficient water softening through selective removal of multivalent ions. PEM membranes effectively reject various micropollutants, including pharmaceuticals and personal care products, due to their well-defined pore size and favorable surface properties. These advantages highlight the broad application potential of PEM membranes in advanced water treatment and resource recovery technologies.

Chapter 3. Polyelectrolyte-Dependent Spray Dynamics and Molecular Interactions in Aerosol-Assisted Printing of Multilayer Membranes: Implications on Assembly and Filtration Performance

Abstract

Polyelectrolyte multilayer (PEM) membranes, renowned for their tunable chemistry and structural versatility, are at the forefront of advancing nanofiltration (NF) technologies, offering outstanding separation performance. Spray-assisted layer-by-layer assembly is an emerging method for fabricating PEM membranes. However, the influence of spray dynamics of different polyelectrolytes (PEs), including aerosolization, droplet size distribution, and droplet transportation, as well as molecular interactions between different PEs following aerosol deposition, on multilayer formation and membrane performance remains poorly understood. Herein, we developed an aerosol-assisted printing (AAP) system for fabricating PEM NF membranes with three polymeric structures, namely, those of polyethyleneimine (PEI)/poly(sodium 4-styrenesulfonate) (PSS), poly (allylamine hydrochloride) (PAH)/PSS, and poly(diallyldimethylammonium chloride) (PDDA)/PSS. Using in-line aerosol characterization, we measured droplet size and velocity of different PEs droplets during the spray process. Among these four PEs, PEI droplets form the largest droplets with the highest momentum, enhancing their deposition efficiency and leading to a thick multilayer. The three PE pairs are uniformly distributed throughout their PEM structure when assembled using the AAP method, forming a well-intermixed and homogeneous PEC within the membrane. The thicker and denser $(PEI/PSS)_2$ membranes have lower water permeability and higher rejection of neutral organic solutes than $(PAH/PSS)_2$ and $(PDDA/PSS)_2$ membranes do, demonstrating $(PEI/PSS)_2$ membranes' ability to achieve NF-level filtration performance with minimal fabrication time and material consumption.

The structures of PAH/PSS membranes and PDDA/PSS membranes are looser, which is due to their lower charge densities compared to PEI/PSS pairs. The $(PDDA/PSS)_2$ membrane has a more negative surface charge than the other two membranes, leading to higher Na_2SO_4 rejection. This study reveals key insights into the relationship between PE composition, multilayer formation, and membrane filtration performance, advancing PEM fabrication and enabling future innovations in spray-assisted processing for various materials.

3.1 Introduction

Global water scarcity and the growing demand for high-quality process streams continue to drive the search for membrane materials that enable high selectivity, chemical tolerance, and scalability. Polyelectrolyte multilayer (PEM) membranes represent a distinct category of nanofiltration (NF) membranes as compared to commercial polyamide-based membranes, featuring a selective layer composed of alternatively charged polyelectrolytes (PEs) assembled in a layer-by-layer (LbL) fashion. The past two decades have witnessed a keen interest in developing and applying PEM membranes in water treatment. Built through the iterative adsorption of oppositely charged PEs, PEMs offer exceptional tunability in membrane design (Jonkers et al., 2024; Scheepers et al., 2023; te Brinke et al., 2020).

The most widely studied polycations are poly(diallyldimethylammonium chloride) (PDDA), poly (allylamine hydrochloride) (PAH), and polyethyleneimine (PEI), and the commonly used polyanions are poly(sodium 4-styrenesulfonate) (PSS) and poly(acrylic acid) (PAA). By simply altering the polycation and polyanion pairs used during assembly, it is possible to tailor a wide range of membrane properties, including thickness, porosity/pore size, surface charge, and hydrophilicity, thus creating a wide range of separation properties (Evdochenko et al., 2020;

Regenspurg et al., 2024; Reurink et al., 2020; Scheepers et al., 2023). In aqueous systems (e.g., dip coating), the formation and quality of polyelectrolyte multilayers remain strongly dependent on the diffusive transport of polymer chains toward and within the growing film, which is heavily dependent on the molecular weight of PEs. For example, lower molecular weight PEs exhibit higher chain mobility, which facilitates more efficient interpenetration and stronger electrostatic binding with oppositely charged counterparts (Regenspurg et al., 2022). Another contributing molecular property is the charge density of different PE pairs. The charge density for PE pairs is defined as a couple of cationic and anionic monomers per number of carbon atoms (Regenspurg et al., 2024). Among the PE pairs studied, PEI/PSS exhibits the highest charge density, followed by PAH/PSS and then PDDA/PSS (Regenspurg et al., 2024). A higher charge density typically results in the formation of denser membranes. Krasemann and Tieke (2000) showed that a denser membrane is obtained by using PAH, instead of PDDA, as the polycation. The higher density and smaller effective pore size of the PAH/PSS multilayers are likely due to the greater charge density of PAH/PSS compared to PDDA/PSS, leading to stronger electrostatic interactions within the film and thus a more compact structure. A similar observation was obtained by De Vos et al (Reurink et al., 2020) in a separate study comparing PEI/PSS and PAH/PSS multilayers. They observed that PEI/PSS membranes exhibited lower water permeability, higher NaCl retention, and a smaller molecular weight cut-off (MWCO) than the PAH/PSS counterparts. The denser structure of PEI/PSS was attributed to the higher charge density. However, an understanding of the influence of specific molecular interactions on the structure of PEM films and membrane performance remains incomplete.

Spray coating has emerged as a promising membrane preparation method due to its benefits, including a drastic decrease in process time due to the improved means of mass transfer, and a

much smaller solution quantity required (Ma et al., 2021; Zhao et al., 2022) while maintaining the same film quality. The application of spray-assembled PEM as active layers for NF and reverse osmosis (RO) membranes has shown great promise (Cho et al., 2014; Li et al., 2018; Yassari et al., 2025). To date, spray-fabricated PEM membranes have primarily been optimized by tuning the number of bilayers, solution concentrations, ionic strength, and incorporating crosslinkers to enhance structural stability and filtration performance (Cho et al., 2015; Xiang et al., 2015). However, its process is fundamentally different from that of the dip coating method. Specifically, the chemical structures of the PEs not only affect the molecular interactions of the (deposited) film, but also the dynamic behavior of droplets during their generation and deposition (e.g., droplet size and deposition efficacy). In spray-based processes, membrane formation begins with the impingement of aerosolized droplets on the substrate. The possibility of droplet impingement on the membrane surface could be affected by many process parameters, such as droplet size and velocity. A deep investigation into the coupled effects of spray dynamics and molecular interactions of PEs, as impacted by the polyelectrolyte structures, on the membrane structure and performance is needed.

In this study, we used an aerosol-assisted printing (AAP) system consisting of a commercial 3D printer with a Collison nebulizer to fabricate PEM membranes with different PE pairs. The polyanion PSS is combined with three different polycations, including the branched PEI containing a high density of primary, secondary, and tertiary amine groups, linear PAH containing primary amine groups along an aliphatic backbone, and quaternary ammonium-based PDDA (Figure S3.1). The PE aerosols were characterized using a suite of novel in-line techniques, including a laser diffraction size analyzer (LDSA) and laser Doppler velocimetry (LDV), which provides essential information on the droplet size and velocity for understanding the deposition behavior of different

PEs. The deposited PEs were analyzed by atomic force microscopy (AFM), and the resulting PEM membranes were further characterized using field emission scanning electron microscopy (FESEM) and zeta potential measurements. To establish a clear link between multilayer structure and membrane performance, the PEM membranes were subsequently evaluated for their retention capabilities toward various ions and organic solutes. Our study provides novel mechanistic insights into the formation, structure, and filtration performance of PEMs assembled from different polyelectrolyte compositions via AAP. This work not only advances the understanding of PEM membrane fabrication but also supports further innovation in the spray-assisted processing of diverse functional materials.

3.2 Experimental

3.2.1 Materials and Chemicals

Commercially available polyacrylonitrile (PAN) ultrafiltration membranes with a MWCO of 300 kDa (Sterlitech) were used as substrates. The polycations employed included PEI with molecular weights of 750 kDa (Sigma-Aldrich), PAH with 15 kDa (Aladdin), and PDDA with 100-200 kDa (Aladdin). PSS with 1000 kDa served as the polyanion. The chemical structures of PEI, PAH, PDDA and PSS were shown in Figure S3.1. NaOH was purchased from Duksan. Poly (ethylene glycol) (PEG) with different molecular weights (200, 400, 1000, 1500, 2000, and 6000 Da) was purchased from Sigma-Aldrich. Na_2SO_4 was from J&K Scientific and $MgSO_4$, $MgCl_2$, and NaCl were purchased from Sigma-Aldrich. Deionized water (Milli-Q plus system, Millipore) was used to prepare solutions and test membrane water permeability.

3.2.2 Aerosol-Assisted Printing Setup

The AAP setup was constructed in our laboratory as illustrated in Figure S3.2. The equipment consists of an aerosol spray system, a pressure supply system, and a 3D printer. The aerosol spray system includes two six-jet Collison nebulizers (CH Technologies). A stainless-steel tube as the nebulizer outlet (diameter 14 mm) was aligned perpendicular to the platform/substrate surface. The distance between the nozzle and the membrane substrate surface was 15 mm. The pressure supply system provides a constant pressure of 0.5-1.5 bar by an air compressor. The 3D printer (3DLDL, six point zero inc.) was used to control the movement of the nozzle. The nozzle moved at a speed of 1,500 mm min^{-1} in a raster scan pattern, with a 7 mm line spacing.

3.2.3 PEM Membrane Fabrication

PEM membranes were assembled by AAP. The equipment consists of an aerosol spray system, a pressure supply system, and a 3D printer. The Collison nebulizer generates micrometer-sized droplets at an applied pressure of 1 bar using compressed air as the carrier gas. A stainless-steel tube as the nebulizer outlet (14 mm diameter) was aligned perpendicular to the substrate surface, positioned 15 mm above the substrate. The 3D printer (3DLDL, Six Point Zero Inc.) was used to control the movement of the nozzle.

Prior to LbL assembly coating, the PAN substrate was immersed in ethanol and then rinsed with pure water to remove preservatives. Subsequently, the treated PAN substrates were hydrolyzed in a 2.0 M NaOH solution at an ambient temperature for 2 hours. The HPAN membranes were rinsed with pure water to remove excessive NaOH and then stored in pure water for further PEM membrane preparation. The polycation with a concentration of 8.0 g L^{-1} and polyanion with a concentration of 16.0 g L^{-1} were added in two separate Collison nebulizers and sprayed on the substrates by the AAP setup in a step-by-step fashion. The HPAN substrate was first sprayed with polycation aerosol, after which the polyanion aerosol was introduced to the polycation-assembled membrane. The first PE bilayer (i.e., one polycation-polyanion bilayer) was produced. The PEM membranes coated with two bilayers were prepared by repeating the above coating. The viscosity of each PE solution was determined using a digital viscometer (Uchen), equipped with spindle No. 2 operating at 60 rpm. The surface tension of each PE solution was measured by a platinum ring tensiometer (MC-1021, MINCE). Each measurement was performed in triplicate to ensure reproducibility.

3.2.4 Characterization of Aerosol Deposition Process

Advanced in-line and off-line characterization and modeling techniques were used to analyze the aerosol/PE deposition process. The velocity field of the aerosol flow was monitored by a 2D mini LDV (Measurement Science). The continuous laser output was split into two beams of equal intensity using a beam splitter. Channel 1 operated at a wavelength of 658 nm and was utilized to measure the aerosol velocity component in the vertical direction. Channel 2 operated at 830 nm and was used to capture the horizontal velocity component of the aerosol flow. A laser diffraction size analyzer (Winner 311XP, Jinan Winner) was used to determine the size distribution of droplets produced by the Collison nebulizer. To obtain the size distribution and microscopic morphology of the deposited, dried PE particles, a trace amount of the PE was deposited on a silicon surface for AFM (NanoScope 8, Bruker) analysis. The dried PE particle size distribution was analyzed from the AFM phase images using ImageJ software. Deposition efficiency was determined by the ratio of the PE mass deposited over that delivered out of the nebulizer.

3.2.5 Membrane Characterization

The membrane samples were air-dried at ambient temperature before characterization. ATR-FTIR (PerkinElmer Spectrum Two) was used to investigate the surface chemistry evolution during the PE assembly, with a resolution of 4 cm^{-1} and a wavenumber range from 4,000 to 400 cm^{-1}. Membrane surface zeta potential was measured using a streaming potential analyzer (SurPASS electrokinetic analyzer, Anton Paar) with 1 mM KCl solution as the background electrolyte. The average values were obtained from at least three repeated measurements. Water contact angles (WCAs) were measured using the sessile drop method as done in our previous studies (Wan and Jiang, 2021). A 5-μL water droplet was dropped onto the membrane surface and photographed using a high-definition digital camera (BC4800, BoChen). The measurements were conducted at

left and right contact angles from the digital images with ImageJ software. Average data was obtained from five random locations in the membrane samples. Cross-sectional images of the PEM membranes were observed using a FESEM (Tescan MAIA3) after sputter coating the samples with gold (MCM-200 ion sputter coater, Micro Optics).

The elemental composition of the PEM membrane was analyzed using X-ray photoelectron spectroscopy (XPS, Nexsa G2 surface analysis system, Thermo Fisher Scientific). The XPS survey spectra were collected using a scanning monochromated Al source (1486.6 eV; 72 W; 400 μm spot size). The takeoff angle was 60° from the vertical direction, and the X-ray beam collected C1s, N1s, O1s, and S2p elemental information while rastering over an area with a diameter of 1.2 mm. Depth profiling was accomplished using the instrument's Ar^+ ion source operated at 12 keV. The collected data were charge-corrected, referencing the binding energy of the carbon-carbon bond to 284.8 eV.

3.2.6 Membrane Filtration Performance

Membrane filtration performance was evaluated using a crossflow filtration set-up. Each membrane coupon, with an effective area of 8 cm^2, was tested at 5 bar and a crossflow velocity of 26.7 cm s^{-1}. The membrane was compacted by pure water under a pressure of 5 bar for 2 hours before the permeability/rejection experiment. The weight of the permeate was measured using an automatic electronic balance (Ohaus, SPX2201) at a 60 s interval for 30 min. The pure water permeability (J_w, $L \cdot m^{-2} \cdot h^{-1} \cdot bar^{-1}$) was calculated by the Eq. (3.1):

$$J_w = \frac{V}{\Delta P \times A \times \Delta t} \tag{3.1}$$

where ΔP (bar) is the trans-membrane pressure, A is the effective filtration membrane area (m^2), and V is the volume (L) of permeate collected over an operating time (Δt (h)).

The MWCO values of the membranes were determined by fitting the rejection curve of PEG with different molecular weights (200, 400, 1000, 1500, 2000, and 6000 Da). The concentrations of the solutes were measured using a TOC analyzer (Shimadzu, Japan). The feed solution of each sugar was 100 mg TOC L^{-1}. The solutes and salt rejection, R (%), was calculated using Eq. (3.2):

$$R = \left(1 - \frac{C_p}{C_f}\right) \times 100\% \tag{3.2}$$

where C_p is the permeate concentration and C_f is the concentration of the feed solution. The data is an average value from measuring at least three samples of each kind of membrane.

3.3 Results and Discussion

3.3.1 Polyelectrolyte Aerosol Characterization

PE solutions were aerosolized using a Collison nebulizer, which breaks the liquid into fine droplets through high-velocity gas flow. The droplet size distribution varied among different PEs (Figure 3.1a). The corresponding volumetric median diameters (Dv_{50}) of the PEI, PAH, PDDA, and PSS aerosols followed the order PEI > PAH > PDDA > PSS (Figure 3.1b). Specifically, the Dv_{50} values were 2.91 μm for PEI, 2.84 μm for PAH, 2.77 μm for PDDA, and 2.45 μm for PSS. These differences in droplet size can be explained by the variations in solution viscosity and surface tension, which are critical factors in the atomization process (Mc Callion et al., 1996; McCallion et al., 1995; Steckel and Eskandar, 2003).

The viscosities of the PEI, PAH, PDDA, and PSS solutions were 4.9, 5.7, 9.6, and 18.7 mPa s (Figure 3.1c), respectively. During nebulization, higher solution viscosity increases the liquid hold-up in the siphon. This increased hold-up narrows the effective diameter of the jetting channel, leading to an increase in suction pressure and a higher gas velocity through the nozzle (Feng et al., 2021). The elevated gas velocity promotes more intense atomization of the liquid stream, breaking

it into smaller droplets (Davis, 1978). Because PSS has the highest viscosity, it produced the smallest droplets. Surface tension also influences droplet formation by affecting the ease with which a liquid jet breaks into smaller droplets. Surface tension values were 79.26 mN m^{-1} for PEI, 79.40 mN m^{-1} for PAH, 77.51 mN m^{-1} for PDDA, and 72.32 mN m^{-1} for PSS (Figure 3.1d). Lower surface tension reduces the energy required to break up the liquid stream into droplets, promoting the formation of finer aerosols (Modi et al., 2023). Accordingly, the PSS solution, having the lowest surface tension among these four PE solutions, generates the smallest droplets, whereas PEI and PAH solutions with comparatively higher surface tensions result in moderately larger droplets.

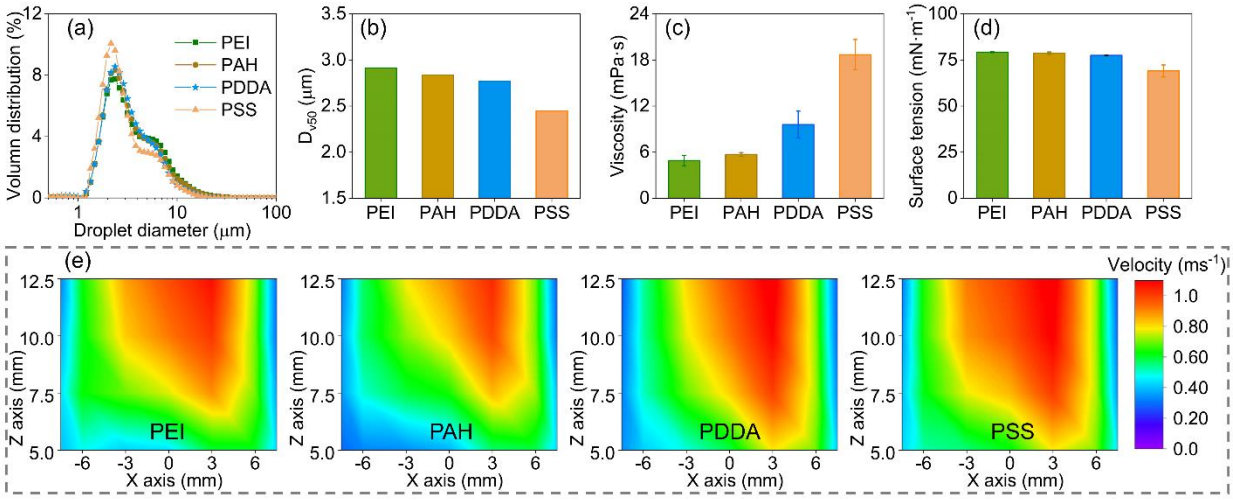

Figure 3.1 (a) Droplet size distribution of PEI, PAH, PDDA, and PSS droplets, (b) Dv_{50} of PEI, PAH, PDDA, and PSS droplets, (c) viscosity of PEI, PAH, PDDA, and PSS solutions, (d) surface tension of PEI, PAH, PDDA, and PSS solutions, and (e) the vertical velocity distribution field of PEI, PAH, PDDA, and PSS aerosols under nebulizer pressure of 1 bar.

The 2D vertical velocity distribution field of the aerosol flow from the nozzle to the substrate was measured by LDV (Figure 3.1e). In the velocity field, the zero point was defined at the center

of the substrate. After exiting the nozzle (z = 15 mm), the velocity field exhibits a trend where the maximum velocity is initially attained at the nozzle exit, followed by a deceleration caused by air drag (Chen et al., 2018). Under the operating pressure of 1 bar, the velocities of PEI and PAH aerosols were approximately 1.0 m s^{-1} at the nozzle exit, while PDDA and PSS aerosols had higher velocities around 1.1 m s^{-1} (Figure 3.1e). These velocity differences can be explained by the earlier-discussed viscosity effects. The higher viscosities of PDDA and PSS solutions (Figure 3.1c) led to greater liquid hold-up in the Collison nebulizer, narrowing the jetting channel and increasing the gas velocity. As the droplets traveled toward the substrate, their velocities decreased due to air drag and dispersion. At a distance of 5 mm from the substrate (i.e., the lowest height that can be measured by the LDV due to limited laser angle), the velocities of PEI and PAH aerosols dropped to approximately 0.6 m s^{-1}, while PDDA and PSS aerosols had higher velocities around 0.8 m s^{-1} (Figure 3.1e).

3.3.2 PE Aerosol Deposition and Multilayer Formation

After droplets were deposited on the membrane substrate, the water solvent in the PE droplets evaporated, and the dried PE particles were assembled on the membrane surface. The diameter of the (completely dried) PEI particle from a droplet can be roughly estimated by the one-droplet-one-particle (ODOP) principle based on mass conservation (Wang et al., 2012; Wang et al., 2009; Wang et al., 2007).

$$D_p = D_d(C/\rho)^{1/3} \tag{3.3}$$

where D_d and D_p are the diameters of the droplet from the nebulizer and the dried particle, respectively, C is the concentration of the precursor PE solution, and ρ is the density of that PE.

Based on Eq. 3.3, a 2.91 μm PEI droplet corresponded to a PEI particle size of 576 nm, a 2.84 μm PAH droplet corresponded to a PAH particle size of 542 nm, a 2.77 μm PDDA droplet

corresponded to a PDDA particle size of 538 nm, and a 2.45 μm PSS droplet corresponded to a PSS particle size of 665 nm. These four dried PE particles were characterized by AFM (Figure 3.2a-d). The phase image obtained by AFM can distinguish the PE and silicon regions because of their different mechanical properties. The dark areas with a low phase shift represent silicon, while light-colored regions with higher phase shifts represent the PE matrix. From AFM, the counted PEI, PAH, PDDA, and PSS particles had peak diameters of approximately 14, 6, 6, and 12 nm (Figure 3.2a-d), respectively. The particle sizes measured by AFM were smaller than those calculated based on the ODOP principle, suggesting that the droplets do not fully evaporate before reaching the membrane surface. Instead, upon impact, the droplets spread across the substrate, leading to the distribution of polyelectrolytes and the formation of smaller particles.

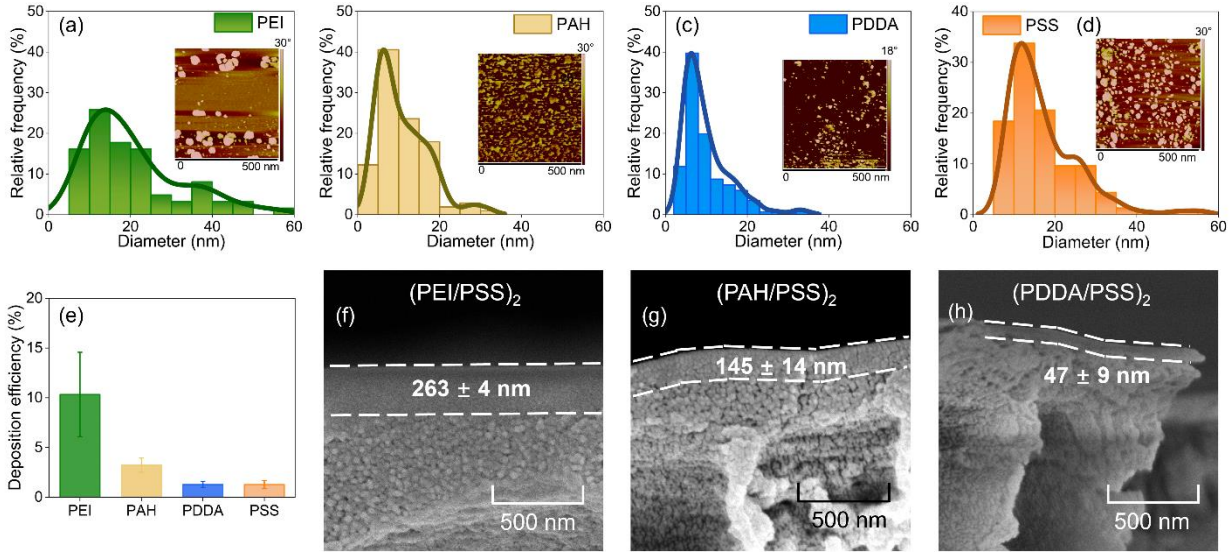

Figure 3.2 (a-d) Size distribution of deposited PEI, PAH, PDDA, and PSS particles on the silicon wafer, and the inset figures are representative phase, (e) comparison of PEI, PAH, PDDA, and PSS deposition efficiency under 1 bar nebulizer pressure and (f-h) cross-section SEM images of $(PEI/PSS)_2$, $(PAH/PSS)_2$, and $(PDDA/PSS)_2$ membranes, respectively.

By continuous spraying, more PEs were deposited over the substrate. The deposition efficiency, defined as the ratio of the deposited mass to the sprayed mass, was quantified for each PE: PEI, PAH, PDDA, and PSS, exhibiting deposition efficiencies of 10.3%, 3.2%, 1.3%, and 1.3% (Figure 3.2e), respectively. Because of the larger droplet size, the PEI droplets have greater momentum, resulting in larger deposition mass on the substrate than the other PE droplets. Notably, even when using the same PE, the deposition efficiency can vary depending on the substrate area. For the smaller area (4×4 cm^2), the deposition efficiency of PEI is ca. 12% which is smaller than that for the larger area (ca. 33%; 7×13 cm^2) (Figure S3.3). This difference arises from particle flow dynamics during aerosol transport and deposition. When aerosolized droplets encounter an obstacle, larger and heavier droplets tend to maintain a straight trajectory due to their higher momentum and gravitational settling, resulting in more efficient capture on the target surface. In contrast, smaller or lighter droplets are more easily carried along the curved airflow streamlines, which can lead to their deflection or resuspension. For a small area, the measured deposition efficiency mainly reflects the direct capture of sufficiently large droplets. In a larger sprayed area, however, some of the smaller droplets that were initially deflected or resuspended can eventually slow down, escape the influence of the airflow, and redeposit onto the substrate, thereby increasing overall deposition efficiency.

As PE droplets were continuously sprayed onto the substrate, they underwent physical impaction and spreading, gradually accumulating to form distinct PE layers. Through repeated deposition of oppositely charged PEs, a multilayer structure was built up via the layer-by-layer assembly process. Cross-sectional FESEM images reveal differences in the thickness of the various two-bilayer PEMs (Figure 3.2f-h). The resulting multilayer thicknesses were 263 ± 4 nm for PEI-PSS multilayers, 145 ± 14 nm for PAH-PSS multilayers, and 47 ± 9 nm for PDDA-PSS

multilayers. These variations correspond well with the deposition efficiencies of the respective polycations. The deposition efficiency followed the order PEI > PAH > PDDA. In sum, the larger droplet size imparts greater momentum, enhancing its deposition efficiency and leading to a thicker multilayer structure. This highlights the pivotal role of droplet dynamics in governing deposition behavior and ultimately shaping the final membrane architecture.

3.3.3 Characteristics of Polyelectrolyte Multilayer Membranes

The surface charge nature of PEM membranes was evaluated by measuring streaming potential to further monitor the assembly process (Figure 3.3a). The HPAN substrate had a negative zeta potential of -10.5 mV. Upon deposition of the polycation layer, the surface charge shifted to positive, while subsequent deposition of the polyanion PSS reversed the charge to more negative values. This alternating charge pattern continued with each successive layer, producing a characteristic zigzag profile. The observed odd-even variation in zeta potential reflects the surface dominance of the terminal PE, further confirming the successful layer-by-layer assembly of the PEM membranes (Ilyas et al., 2015; Wang et al., 2010). The PSS-dominated capping layers result in stable negative surface charges, which are expected to enhance the rejection of anionic solutes via electrostatic repulsion.

The water contact angle measurements reflect the evolving surface hydrophilicity of the membranes during the layer-by-layer assembly process. The alternating deposition of polycations and polyanions also resulted in an odd-even pattern in the contact angle values (Figure 3.3b). The contact angles of the PSS-terminated layer were significantly lower compared to those of polycation-terminated layers (PEI-terminated layer, PAH-terminated layer, and PDDA-terminated layer), suggesting the PSS layer is more hydrophilic than the PEI, PAH, and PDDA layers (Liu et

al., 2015; Qi et al., 2012). The sulfonate ($-SO_3^-$) groups in PSS carry a permanent negative charge and contain highly electronegative oxygen atoms, which strongly attract water molecules through ion-dipole interactions and hydrogen bonding. In contrast, the cationic functionalities in PEI, PAH, and PDDA are based on nitrogen atoms, which are less electronegative than oxygen and thus form weaker hydrogen bonds with water. The presence of hydrophilic functional groups in the active layer enhances membrane hydrophilicity, improves the surface's affinity for water, and facilitates mass transfer within the membrane pores (Wang et al., 2022c).

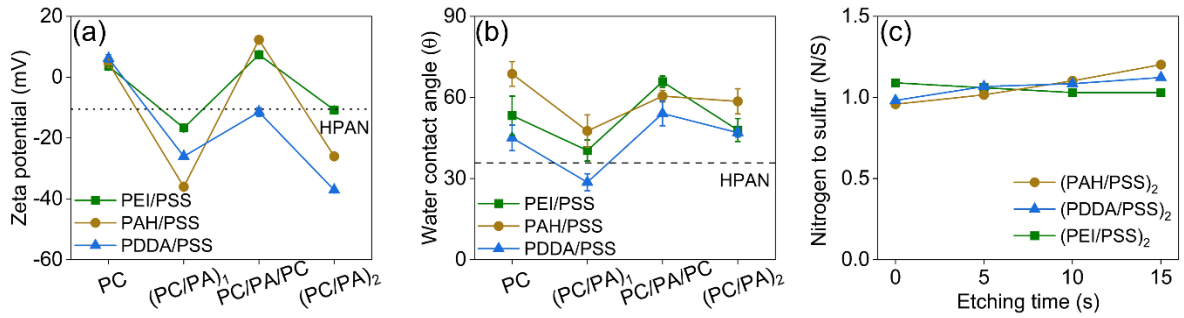

Figure 3.3 Surface characterization of the different PEM membranes including PEI/PSS, PAH/PSS, PDDA/PSS membranes and hydrolyzed polyacrylonitrile (HPAN) substrate: (a) surface zeta potential evolution at pH 7 during LbL deposition of polycation (PC) and polyanion (PA), (b) water contact angle evolution during LbL deposition of PC and PA, and (c) ratios of elemental fraction of nitrogen (N) to sulfur (S) of the $(PEI/PSS)_2$, $(PAH/PSS)_2$, and $(PDDA/PSS)_2$ membranes determined from the XPS depth profiling analysis.

Based on the surface properties observed during the alternating deposition of polycations and polyanions, the PEM initially appears to form a typical LbL structure. The top-view SEM images (Figure S3.4) showed the morphology of different PEM membrane surfaces. The $(PEI/PSS)_2$ membrane has the smoothest and most compact surface, followed by $(PDDA/PSS)_2$ with moderate

roughness, while $(PAH/PSS)_2$ exhibits a rough and irregular morphology. However, post-deposition diffusion of the polyelectrolytes leads to significant interpenetration between the layers, resulting in the formation of a PEC (Gilbert et al., 2013; Jean et al., 2008). To further investigate the internal structure of PEM membranes with different compositions, X-ray photoelectron spectroscopy (XPS) depth profiling was conducted on membranes assembled from PEI/PSS, PAH/PSS, and PDDA/PSS using three printing scans and two bilayers.

Nitrogen was used as an indicator for polycations, since all selected polycations, including PDDA, PAH, and PEI, contain nitrogen through their functional groups (Figure S3.1). PDDA contains quaternary ammonium groups, while PAH and PEI contain amine groups. The polyanion PSS contains sulfonate groups, which are represented by sulfur. Therefore, the nitrogen-to-sulfur (N/S) atomic ratio was used to assess the relative distribution of polycations and polyanions within their structure. The underlying HPAN substrate was reached at an etching time of approximately 20 s when the PEM layer had a thickness of a few hundred nanometers. Therefore, to investigate the elemental composition at different depths within the different PEM, XPS depth profiling was conducted at etching times of 5, 10, and 15 s. The N/S ratios of the $(PEI/PSS)_2$ membrane, $(PAH/PSS)_2$ membrane, and $(PDDA/PSS)_2$ membrane were consistent at ca. 1.0 from 0 to 15 s of etching (Figure 3.3c). These results indicate that, regardless of the specific polycation-polyanion pair used, the components were uniformly distributed throughout the PEM structure when assembled using the AAP method. This uniform elemental distribution suggests the formation of a well-intermixed and homogeneous PEC within the PEM internal structure.

3.3.4 Membrane Filtration Performance

The pure water permeability of the PEM membranes was evaluated to assess their hydraulic performance (Figure 3.4a). The $(PEI/PSS)_2$ membrane exhibited the lowest permeability at 11.8 L

m^{-2} h^{-1} bar^{-1}, while the $(PAH/PSS)_2$ and $(PDDA/PSS)_2$ membranes showed significantly higher values of 26.7 and 28.5 L m^{-2} h^{-1} bar^{-1}, respectively. This is in accordance with the increase in the layer thickness (Figure 3.2f-h), thereby engendering higher overall hydraulic resistance. The thicker $(PEI/PSS)_2$ membrane imposed greater hydraulic resistance to water flow, resulting in lower permeability. In contrast, the thinner $(PDDA/PSS)_2$ membranes offered less hydraulic resistance, enabling higher water permeability under the same pressure conditions.

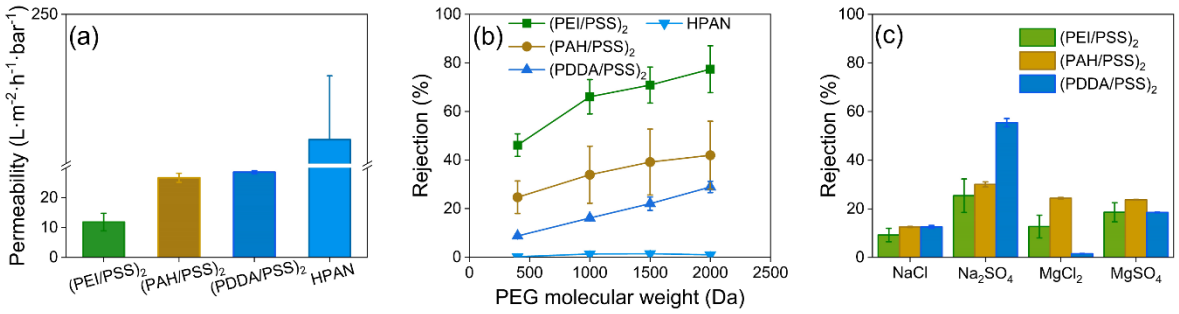

Figure 3.4 Filtration performance of $(PEI/PSS)_2$, $(PAH/PSS)_2$, and $(PDDA/PSS)_2$ membranes and HPAN substrate: (a) pure water permeability, (b) PEG rejection curve; and (c) Salt rejection of $(PEI/PSS)_2$, $(PAH/PSS)_2$, and $(PDDA/PSS)_2$ membranes.

Moreover, the rejections of neutral organic compounds of increasing molecular weights were evaluated (Figure 3.4b). All of these three PEM membranes exhibited MWCO exceeding 2000 Da, indicating average pore sizes greater than 1 nm. The PEG rejection of $(PEI/PSS)_2$ membrane was much higher than that of $(PAH/PSS)_2$ and $(PDDA/PSS)_2$ membranes, indicating a denser structure (smaller pore sizes) of the $(PEI/PSS)_2$ membrane. The PEG rejection curve of the $(PAH/PSS)_2$ membranes appeared higher than that of $(PDDA/PSS)_2$ membranes because of the higher charge density (number of ion pairs per number of carbon atoms) of the PE pair in the corresponding PEM membrane (Reurink et al., 2020). For PE pairs, charge density is defined as a couple of cationic

and anionic monomers per number of carbon atoms (Regenspurg et al., 2024). The charge densities of the PEI/PSS, PAH/PSS, and PDDA/PSS pairs are 1/10, 1/11, and 1/16, respectively. A denser membrane would be obtained due to a higher degree of ionic crosslinking per unit of volume. The relatively higher charge density in the PEI/PSS pair facilitates stronger electrostatic binding during assembly, resulting in a more compact and selective membrane. Additionally, a higher charge density likely enhances deposition efficiency because more binding sites are available for electrostatic attraction. Thus, the higher charge density of PEI/PSS pairs contributes to the formation of thicker and denser PEM compared to PAH/PSS and PDDA/PSS.

We further evaluated the rejection of various salts by these PEM membranes, and the results confirmed the significant role of electrostatic repulsion in ion rejection. For the $(PEI/PSS)_2$ membrane, the NaCl rejection was 9%, the rejections of Na_2SO_4 and $MgSO_4$ were 25% and 19%, respectively, and the $MgCl_2$ rejection was 13% (Figure 3.4c). Given that the hydrated radii of Na^+ (0.36 nm), Mg^{2+} (0.42 nm), and SO_4^{2-} (0.38 nm) (Liang et al., 2020) were significantly smaller than the membrane's average pore size (greater than 1 nm), all these ions can readily pass through the membrane pores with minimal steric hindrance. As the $(PEI/PSS)_2$ membranes were negatively charged under pH 7, they were more effective in rejecting salts with divalent anions than cations. The negatively charged top PSS layer of the PEM membranes facilitated the transport of Mg^{2+} ions, resulting in a low rejection of $MgCl_2$.

Notably, the $(PDDA/PSS)_2$ membrane exhibited the highest Na_2SO_4 rejection, reaching 55%, outperforming both the $(PEI/PSS)_2$ (25%) and $(PAH/PSS)_2$ (30%) membranes (Figure 3.4c). This higher Na_2SO_4 rejection can be attributed to the more negative charge present in the $(PDDA/PSS)_2$ membrane surface (Figure 3.3a), which can repel divalent anions like SO_4^{2-} via Donnan exclusion. Despite its thinner layer with a thickness of 47 nm, the $(PDDA/PSS)_2$ membrane demonstrates that

electrostatic repulsion can play a dominant role in ion rejection, even when the polymer structure is loose. In contrast, the thicker $(PEI/PSS)_2$ membrane, though with higher PEG rejection due to its dense structure (size exclusion), exhibited lower Na_2SO_4 rejection, due to its relatively less negative charge. This result emphasizes that, in addition to membrane thickness, surface charge characteristics are critical for achieving high ionic rejection

3.4 Conclusion

In this study, we used the AAP method to fabricate three PEM membranes, with a particular focus on the influence of different polycations (PEI, PAH, and PDDA) on spray dynamics, membrane assembly, and final membrane performance. Our results show that the viscosity and surface tension of the polycation solutions critically influence the atomization process. PEI, with the highest viscosity among the tested polycations, produced larger droplets with higher momentum, thereby increasing deposition efficiency and resulting in thicker multilayers. The resulting multilayer thicknesses were 263 ± 4 nm for $(PEI/PSS)_2$, 145 ± 14 nm for $(PAH/PSS)_2$, and 47 ± 9 nm for $(PDDA/PSS)_2$ membranes, confirming the direct impact of aerosol dynamics on film growth.

The $(PEI/PSS)_2$ membranes, due to their thicker and denser structure, exhibited the lowest water permeability but higher rejection of neutral organic solutes. The $(PDDA/PSS)_2$ membranes exhibited a more negatively charged surface, as confirmed by zeta potential measurements, which enhanced electrostatic repulsion against multivalent anions and resulted in the highest Na_2SO_4 rejection among the three PEM membranes. The $(PAH/PSS)_2$ membrane showed intermediate performance in both permeability and selectivity. Overall, this work highlights the role of different PEs in governing spray atomization, multilayer formation, and membrane separation properties. These insights offer practical guidance for tailoring membrane performance via rational selection

of polyelectrolyte pairs and optimized AAP processing, providing a foundation for the scalable production of next-generation PEM NF membranes for water treatment.

Acknowledgement

This work was supported by Hong Kong Research Grants Council's General Research Fund Scheme (15214222) and Science, Technology and Innovation Commission of Shenzhen Municipality (SGDX20210823103401009).

Appendix A: Supporting Information for Chapter 3

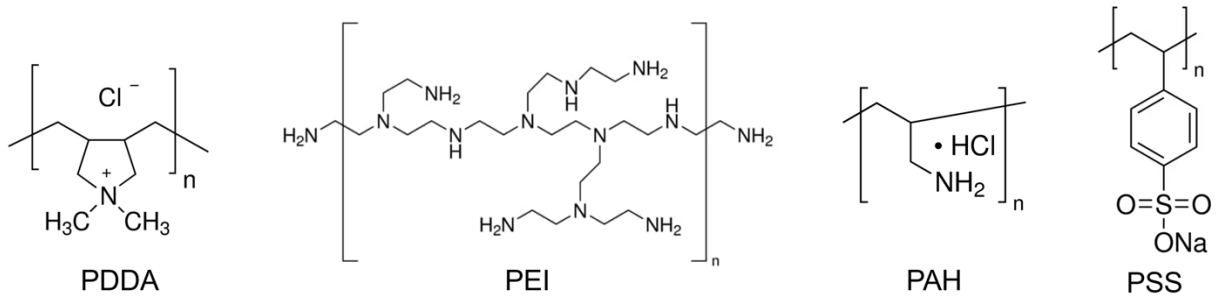

Figure S3. 1 Molecular structure of PEI, PAH, PDDA, and PSS.

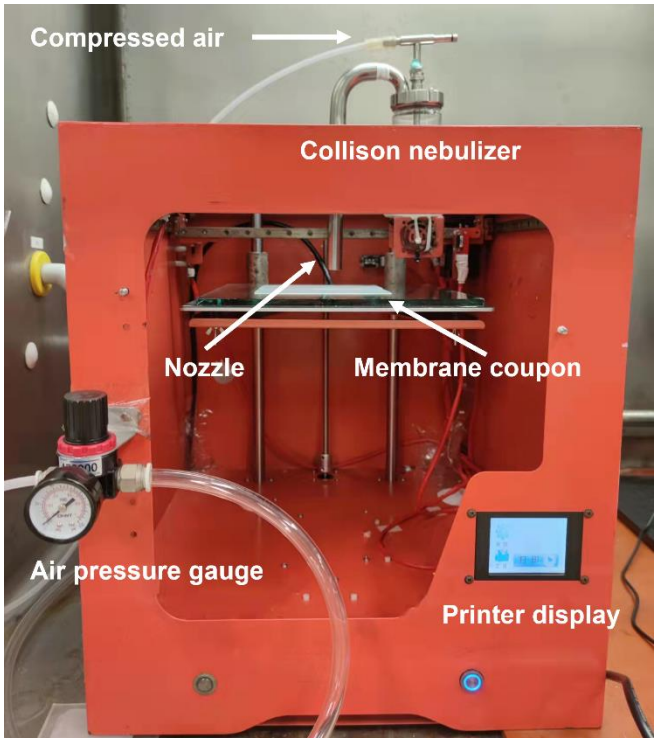

Figure S3.2 A photo of the AAP system by modifying the commercial 3D printer with a Collison nebulizer.

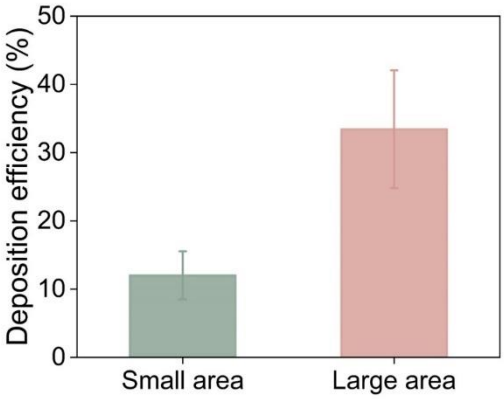

Figure S3.3 Comparison of deposition efficiency comparison of PEI sprayed on small area (4×4 cm^2) and large area (7×13 cm^2) under the printing mode. The nebulizer pressure is set to be 1 bar, and the concentration of PEI solution is 8 g L^{-1}.

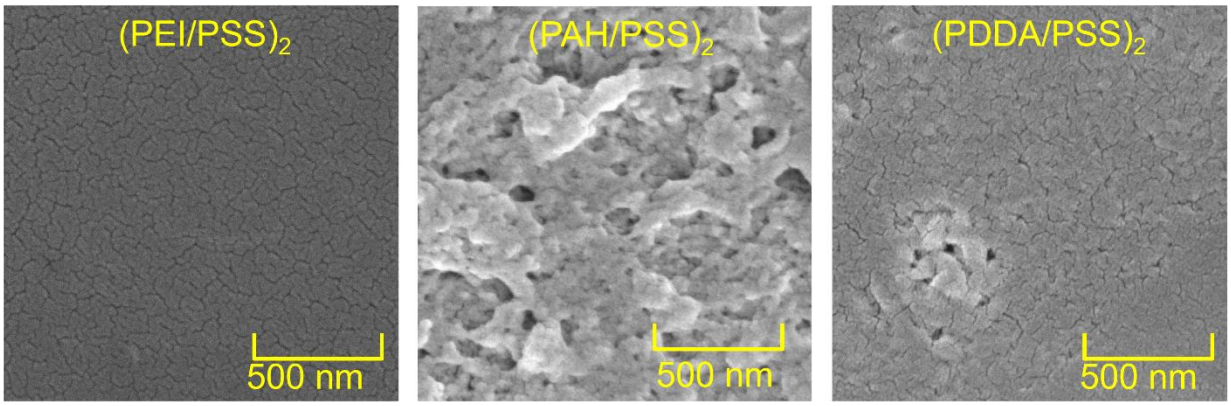

Figure S3.4 SEM images of $(PEI/PSS)_2$, $(PAH/PSS)_2$, and $(PDDA/PSS)_2$ membrane surfaces, respectively.

Chapter 4. Tailoring Polyelectrolyte Multilayer Nanofiltration Membranes by Aerosol-Assisted Printing: Insights into Membrane Formation Mechanisms

(This chapter is based on L. Gan, J. Zhang, Y. Wu, Z. Chen, Z. Zhao, S. Lin, Y. Jiang, Tailoring Polyelectrolyte Multilayer Nanofiltration Membranes by Aerosol-Assisted Printing: Insights into Membrane Formation Mechanisms, Environmental Science & Technology 59(1) (2025) 913-923. DOI: 10.1021/acs.est.4c08638)

Abstract

Polyelectrolyte multilayer (PEM) membranes, with advantageous features of versatile chemistry and structures, are driving the development of advanced NF membranes with exceptional performance. While developing a printing method holds great promise for the eventual mass production of these membranes, reports on the printing method and the underlying mechanisms of membrane formation are currently scarce. Herein, we develop an aerosol-assisted printing (AAP) system for fabricating PEM NF membranes with highly tunable separation characteristics. Our study unveils the three stages of membrane formation from assembly of polyethyleneimine (PEI)/poly(sodium 4-styrenesulfonate) (PSS): aerosol deposition, single PE layer formation, and PEM assembly. The droplet deposition is governed by inertial impaction, and the deposited PEs migrate/entangle to form a single PE layer. The thicknesses of the PE layer and PEM exhibit linear growth as the number of printing scan increases. Furthermore, PE interdigitation forms an effective polymeric network barrier, which increases the resistance to solute and water transport. By manipulating the PE deposition mass and layering, PEM membranes with tunable pore radii (0.40-0.56 nm) and water permeability (5-60 $L \cdot m^{-2} \cdot h^{-1} \cdot bar^{-1}$) were obtained for various water treatment

applications, ranging from micropollutant removal to humic acid filtration. Our study offers valuable mechanistic insights into the PEM formation and precise structural adjustment via printing, thus facilitating scalable manufacturing and widespread applications of the PEM NF membranes.

4.1 Introduction

Nanofiltration (NF) is an attractive pressure-driven membrane process for advanced water treatment because it can remove all pathogens and most organic and inorganic contaminants in a single treatment step. Polyelectrolyte multilayer (PEM) membranes represent a distinct category of NF membranes as compared to commercial polyamide-based membranes, featuring a selective layer composed of alternatively charged polyelectrolytes (PEs) assembled in a layer-by-layer (LbL) fashion. PEM membranes are attractive because of their versatile chemistry and structures, which enable the creation of advanced NF membranes with excellent permselectivity (e.g., divalent over monovalent cations (Durmaz et al., 2021), organic contaminant over cations , chemical stability (e.g., much higher chlorine or acid/base resistance than polyamide membranes , and fouling resistance . These distinctive features offer new possibilities for chemical separations that are challenging for conventional polyamide membranes.

The past two decades have witnessed a keen interest in developing and applying PEM membranes in water treatment. However, despite numerous research with regard to their principles and applications, there has not been a viable technical route for those membranes to be made at an industrial scale and with easiness in controlling their fabrication and structure at a large manufacturing scale. The current method to assemble PEM is dip coating, which cycles a substrate between two reservoirs containing aqueous solutions of PEs of opposite charges. In dip coating-based LbL deposition, a layer of PE adds to the oppositely charged substrate or the previously deposited layer via electrostatic force. The method usually takes a few hours to several days to achieve enough bilayers due to the diffusive time scale (Li et al., 2020). As a result, it is almost impossible for the dip coating method to be scaled up for high-throughput using roll-to-roll

fabrication. Also, the dip coating method requires a large reservoir of PE for immersion, which results in a significant waste of chemicals.

A printing method that utilizes the spray of PE droplets holds great promise for the mass production of PEM. Due to the improved means of mass transfer, the membrane preparation time can be drastically decreased, and much smaller solution quantity can be used (Ma et al., 2021; Zhao et al., 2022). Schlenoff et al. (2000) have suggested that the morphology, uniformity, and chemical composition of sprayed PEM, as well as the selective membrane properties, are virtually identical to those prepared by dip coating. Cho et al. (2014) demonstrated an NF membrane via spray coating of an active layer of poly(acrylic acid) (PAA) and PAH. The membrane can reject up to 80% $CaCl_2$ and 50% NaCl, with a water flux of 1.1-2.3 L m^{-2} h^{-1} bar^{-1}. The spray technique was further used to deposit an ultrathin (ca. 70 nm) active layer consisting of PAH and poly(sodium 4-styrenesulfonate) (PSS), which showed 94% rejection of NaCl with a permeate flux of 0.75 L m^{-2} h^{-1} bar^{-1} (Li et al., 2018).

Despite these early demonstrations, there remain critical knowledge gaps in how a PEM membrane forms during printing. The membrane printing process is complex and involves droplet deposition (aerosolization, transport, impingement, and possible resuspension of droplets), building block assembly, and subsequent evolution into a hierarchical structure (Felton, 2013). One notable influencing factor is the droplet size. Previous studies on spray/droplet-based PEM membrane preparation have primarily involved the use of a spray gun in a fixed position, and the droplets examined in these studies are typically large, ranging from 30 to 50 μm in size. This size limitation hampers the ability to finely tune the membrane structure, including its thickness and pore size. Large droplets result in a high mass deposition on the substrate over a very short time (a few seconds), consequently leading to the formation of thick PE layers (Xiang et al., 2015). As a

result, the dense nature of the deposited layers leads to a low water permeability. Moreover, the drying of these large droplets causes uneven distribution of PEs over the substrate, inducing poor homogeneity and high surface roughness, primarily due to the coffee-ring effect (Bose et al., 2013; Yunker et al., 2011). Droplet velocity is another factor that could have an influence on the kinetic energy of the droplets and thus the impingement of the droplets on the membrane surface. Finally, there remains no information on how the deposited PE molecules assemble into a layer and subsequently a PEM. This is primarily due to a lack of essential experimental data on the deposition of the droplets. Therefore, achieving precise control over droplet generation and deposition becomes critical to finely tuning the membrane's structure and separation properties.

In this study, we develop an AAP system by modifying a commercial 3D printer with a Collison nebulizer. The Collison nebulizer, a well-established aerosol generation instrument known for its high reproducibility and wide range of applications, is selected as the standard droplet generation setup (Hart et al., 2020; Jiang et al., 2014; May, 1973; Wang et al., 2012). The produced aerosols are water droplets with a narrow and small size distribution (mainly 3-5 μm). This choice enables us to not only delicately control the PEM structure and property, but also conveniently construct a conceptual model of the membrane formation. Additionally, we demonstrate the printing of PEM membranes with a large area of 160 cm^2 with a 3D printer. The printing process involves the use of PEI as the polycation and PSS as the polyanion. The deposition of the PE aerosols is characterized by using a suite of state-of-the-art in-line techniques, including laser diffraction size analyzer (LDSA), laser doppler velocimetry (LDV), and is modeled by COMSOL simulation. These characterization and modeling provide new information on the droplet size and velocity for understanding the membrane formation (i.e., the growth of the PEM). By changing the printing process parameters, including per-layer scan number and bilayer number, a spectrum of membrane

separation performance, spanning from loose to dense NF, is achieved. Consequently, our study presents novel mechanistic insights into the formation and precise adjustment of a PEM selective layer using the printing method. This significant contribution expands the current understanding of PEM membrane fabrication techniques, opening up new avenues for advancements in the field.

4.2 Experimental

4.2.1 Materials and Chemicals

A polyacrylonitrile (PAN) membrane (PX, Sterlitech) with a nominal MWCO of 400 kDa was used as the substrate. PEI (MW 750 kDa, Sigma-Aldrich) and PSS (MW 1000 kDa, Sigma-Aldrich) were used as the polycation and polyanion, respectively. A commercial NF membrane (NF270, Dow-Filmtec) was used as a reference membrane for performance comparison. NaOH was purchased from Unichem, and Na_2SO_4 was from J&K Scientific. Humic acid (HA), $MgSO_4$, $MgCl_2$, and NaCl were purchased from Sigma-Aldrich. Erythritol, xylose, glucose, and sucrose (Aladdin) were used as the reference organic solutes to evaluate the dependence of rejection on solute size. Bisphenol A (BPA, J&K Scientific), antipyrine (AP, Sigma-Aldrich), ofloxacin (OFX, Sigma-Aldrich), and ciprofloxacin (CIP, Sigma-Aldrich) were selected micropollutants to test the rejection performance of prepared membranes. Pure water (Milli-Q plus system, Millipore) was used for preparing solutions and testing membrane water permeability.

4.2.2 Polyelectrolyte Multilayer Membrane Fabrication

The PAN substrate was soaked in ethanol and rinsed with pure water to remove the preservatives. Afterwards, the PAN substrate was hydrolyzed in a 2.0 M NaOH solution at ambient temperature for 2 hours. After removing excessive NaOH by rinsing the substrate with pure water, the hydrolyzed PAN (HPAN) substrate was kept in pure water for further PEM membrane preparation. The schematic of membrane printing is shown in Figure 4.1a, and the PEM membrane formation

is further schemed in Figure 4.1b. The complete movement of the nozzle over the entire substrate area was denoted as one scan, and 1-5 scans were conducted to form a single layer with different deposition masses. More printing scans result in more deposited PE mass for a single PE layer. The resultant layer was denoted as PEI_n or PSS_n (n represents scans, n=1-5). A PE bilayer was formed by cycling deposition of the positively charged PEI and negatively charged PSS layers. The resultant membrane with one bilayer was denoted as $(PEI_nPSS_n)_1$. For example, $(PEI_3PSS_3)_1$ indicates the membrane with one PEI/PSS bilayer whose terminating layer is PSS, and both the PEI and PSS layers were printed with three scans of the PE deposition. A series of PEM membranes were prepared with varied scans (1-5) and bilayer numbers (1-2).

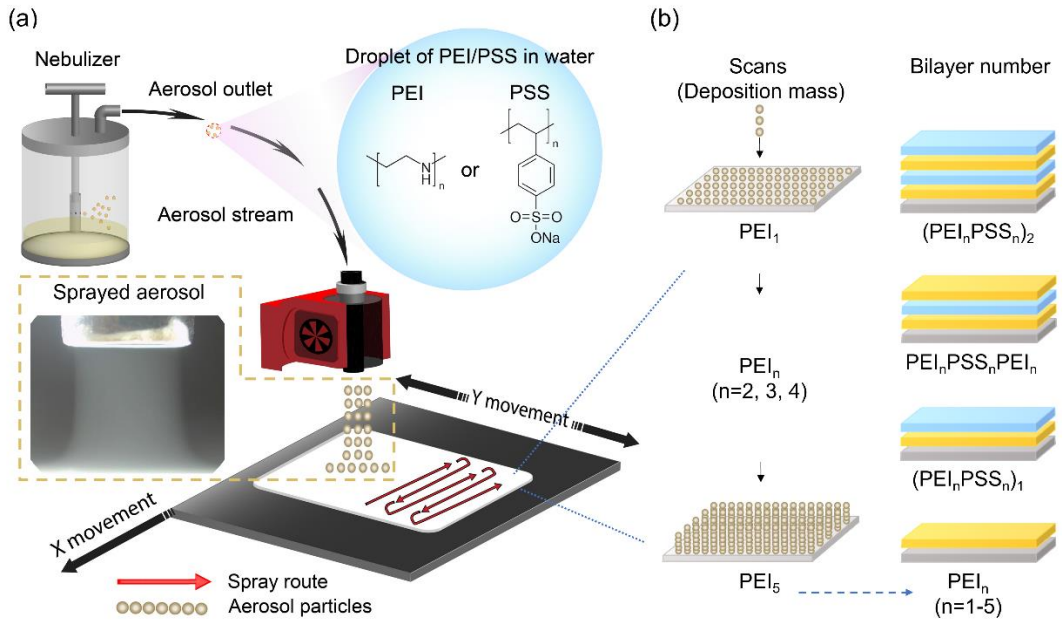

Figure 4.1 Schematics of (a) the PEM membrane fabrication process via aerosol-assisted printing and (b) formation of the $(PEI_nPSS_n)_x$ membrane with various scans and bilayer numbers. Note: n represents n scans for each PEI or PSS layer (n =1-5).

4.2.3 Characterization of Aerosol Deposition Process

Advanced in-line and off-line characterization and modeling techniques were used to analyze the aerosol/PE deposition process. The velocity field of the aerosol flow was monitored by a 2D mini laser Doppler velocimeter (LDV, Measurement Science) as detailed in Text S4.2. A schematic diagram of the measurement positions of the Collison nebulizer is shown in Figure S4.2a. A laser diffraction size analyzer (Winner 311XP, Jinan Winner) was used to determine the size distribution of droplets produced by the Collison nebulizer. To obtain the size distribution and microscopic morphology of the deposited, dried PE particles, a trace amount of the PE was deposited on a silicon surface for atomic force microscopy (AFM, NanoScope 8, Bruker) or on a transmission electron microscope (TEM) grid for TEM (JEM-2010, JEOL) analysis, respectively. The dried PE particle size distribution was analyzed from the AFM phase images using the ImageJ software. Deposition efficiency was determined as the ratio of the PE mass deposited over that delivered out of the nebulizer.

4.2.4 COMSOL Simulation

The fluid flow and mass transport processes were simulated utilizing COMSOL Multiphysics version 6.1. A two-dimensional axisymmetric model was developed to simulate the aerosol flow out of the spray nozzle. This model replicates the spatial configuration of the actual spray setup, focusing on a 2D region measuring 60 mm in length and 15 mm in height, which bisects the aerosol flow along its central axis and is oriented vertically to the membrane substrate. The velocity distribution obtained by LDV (Figure S4.2) was employed as the velocity boundary condition for the computational fluid dynamics (CFD) simulation. For the turbulence calculation, the k-ε model within the Reynolds-Averaged Navier-Stokes (RANS) framework was utilized to simulate the

velocity distribution of the airflow field. The environmental conditions for the CFD simulation were set to a temperature of 293.15 K and an atmospheric pressure of 101.325 kPa.

4.2.5 Membrane Characterization

The membrane coupons were air-dried at ambient temperature before characterization. Attenuated total reflection Fourier transform infrared spectroscopy (ATR-FTIR, PerkinElmer Spectrum Two) was used to investigate the surface chemistry evolution during the PEM assembly, with a resolution of 4 cm^{-1} and a wavenumber range from 4,000 to 400 cm^{-1}. Membrane surface zeta potential was measured using a streaming potential analyzer (SurPASS electrokinetic analyzer, Anton Paar) with 1 mM KCl solution as the background electrolyte. The distribution of deposited PEI and PSS on the membrane surface was characterized using Raman mapping (inVia Micro-Raman microscope, Renishaw). A laser with a 785 nm wavelength was used as the excitation source. Surface and cross-sectional images of the PEM membranes were obtained using the field emission scanning electron microscope (FESEM, Tescan MAIA3) after sputter coating the samples with gold (MCM-200 ion sputter coater, Micro Optics), and the PEM thickness was measured from these images using ImageJ. Membrane surface roughness was evaluated by using AFM in a tapping mode. The X-ray photoelectron spectroscopy (XPS, Nexsa G2 surface analysis system, Thermo Fisher Scientific) combined with depth profiling was used to obtain a detailed chemical analysis of PEM membranes. Detailed XPS information can be found in Text S4.3.

4.2.6 Membrane Filtration Performance Evaluation

Membrane filtration performance was evaluated using a crossflow filtration setup (FlowMEM-0021-HP, FMT). Each membrane coupon, having an effective area of 64.8 cm^2, was tested at 5 bar and a crossflow velocity of 38.5 cm s^{-1}. The membrane was compacted by pure water under a pressure of 5 bar for 2 hours before collecting data for separation performance. The weight of the

permeate was measured using an automatic electronic balance (Ohaus, SPX2201) at a 60 s interval for 30 min.

The MWCO values of the membranes were determined by fitting the intrinsic rejection curve of neutral sugars of various molecular weights (erythritol 122 Da, xylose 150 Da, glucose 180 Da, sucrose 342 Da). The concentrations of the solutes were measured using a total organic carbon (TOC) analyzer (TOC-L, Shimadzu, Japan). The feed solution of each sugar was 50 mg TOC L^{-1}. To account for the concentration polarization effect, mass transfer coefficients were obtained based on fitting the experimental data and used to obtain the intrinsic rejection (Text S4.4) (Bason et al., 2010). The average pore sizes of the PEM membranes with different scans and bilayer numbers were estimated from the steric hindrance pore model (Text S4.5) using intrinsic rejections of the reference organic solutes mentioned above (Boo et al., 2018b; DuChanois et al., 2019). Rejection of micropollutants including BPA, AP, OFX, and CIP were tested using feed solutions containing 0.5 mg L^{-1} of each micropollutant at pH 6, and their concentrations were measured using high-performance liquid chromatography (HPLC) as detailed in Text S4.3.

4.3 Results and Discussion

4.3.1 Polyelectrolyte Aerosol Generation, Characterization, and Deposition

4.3.1.1 Polyelectrolyte Droplet Generation by Aerosolization

The aerosolization was accomplished by the Collison nebulizer where the liquid was broken up into droplets by high-speed gas flow. The size distribution of water droplets was mainly in the range of 3-5 μm with a volumetric median diameter (D_{v50}) of ca. 3.8 μm (Figure S4.3), which is consistent with our previous study (Wang et al., 2012). The ultrafine droplets sprayed by the current system, due to their faster evaporation, can effectively hinder PE aggregation at the droplet edge (Bigioni et al., 2006) and promote even distribution on the surface. The aerosol diameter can

be adjusted by applying varied nebulizer pressures (Figure 4.2a, b). With an increase of nebulizer pressure from 0.5 to 1.5 bar, the D_{v50} of PEI droplets decreased from 3.6 to 2.4 μm and the D_{v50} of PSS droplets decreased from 3.1 to 2.3 μm (Figure 4.2c). The D_{v50} of PEI droplets was larger than that of PSS droplets generated at the same nebulizer pressure due to the different viscosities of their solutions (5 and 20 mPa·s, respectively). Higher viscosity increases liquid retention in the nebulizer transfer channel, while the reduced channel diameter boosts gas velocity, leading to finer atomization of the liquid stream into smaller droplets compared to low-viscosity liquids (Modi et al., 2023).

4.3.1.2 PE Aerosol Transport

The 2D vertical velocity distribution field of the aerosol flow from the nozzle to the substrate as measured by LDV is shown in Figure S4.2b-f. The velocity field exhibited a trend where the maximum velocity was initially attained at the nozzle exit, followed by a deceleration caused by air drag (Chen et al., 2018). Under the operating pressure of 1 bar, the droplet velocity at the nozzle exit was ca. 1.1 m s^{-1}, and the velocity of aerosols reduced to ca. 0.6 m s^{-1} at 5 mm from the substrate (i.e., the lowest height that can be measured by the LDV due to limited laser angle). As the operating pressure increased from 0.5 to 1.5 bar, the velocity at the nozzle exits increased from 0.7 to 1.3 m s^{-1} (Figure 4.2d).

To enable a more in-depth analysis of aerosol transport, COMSOL software was used to simulate the velocity field that was not detected by LDV. In the simulated velocity field, the vertically downward airflow started to form an abrupt bend in the streamlines. This bending stream encountered the substrate again, causing it to change direction and bend upwards (Figure 4.2e). As shown in Figure S4.4, the velocity of upward airflow under nebulizer pressure of 1.5 bar was ca. 1.0 m/s at the coordinates (x = ±25 mm, z = 7 mm). This velocity was notably higher than the

velocity under 1.0 bar (ca 0.6 m/s), as shown in Figure 4.2e. In general, increasing nebulizer pressure increased both downward and upward aerosol velocities.

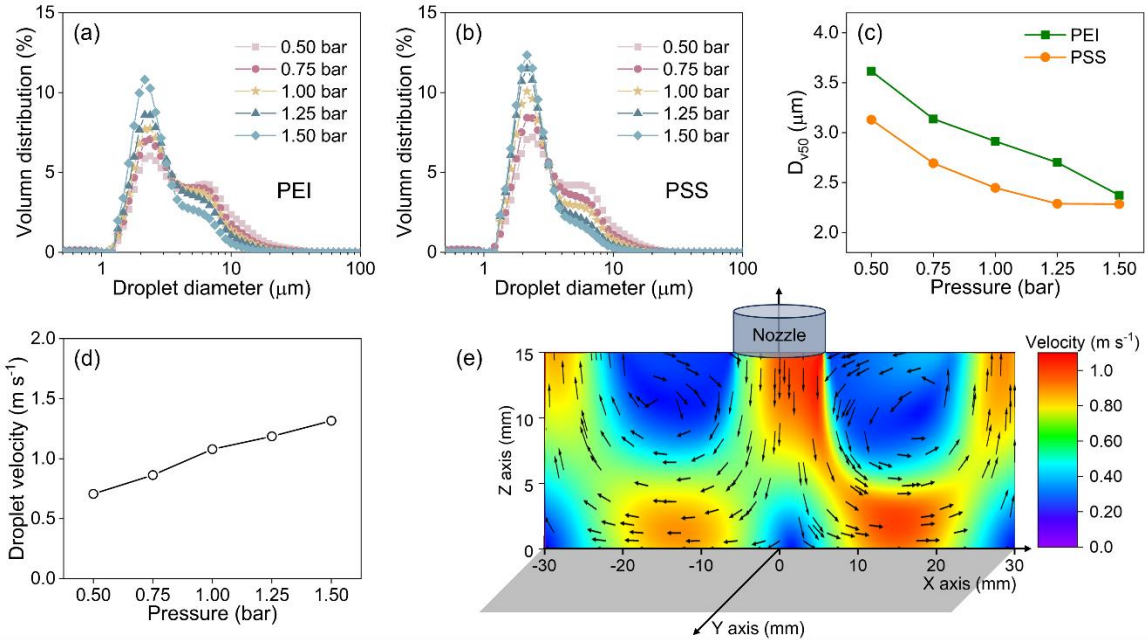

Figure 4.2 Droplet and particle size measurement: size distribution of (a) PEI and (b) PSS droplets generated under different nebulizer pressure; (c) the D_{v50} of PEI and PSS droplets under different nebulizer pressure; (d) droplet velocity of PEI aerosols at the nozzle exit under different nebulizer pressure; (e) velocity distribution field under 1 bar nebulizer pressure from the COMSOL simulation.

4.3.1.3 Aerosol Deposition Mechanism

The effluent stream of PE aerosols was directed towards a flat membrane surface, causing the flow to deflect and creating a curvilinear flow shape (Figure 4.2e). Curvilinear motion is characterized by a dimensionless number called Stokes number (S_{tk}) (Hinds, 1999) which is an indicator of a droplet's tendency to deposit on a surface (Friedlander and Smoke, 2000). A droplet

with a low S_{tk} follows the fluid streamlines, while a particle with a larger S_{tk} can be dominated by its inertia and continues along its initial trajectory.

Based on the S_{tk} (Eq. 2.1), the aerosol size and velocity are the two main factors affecting the inertial deposition efficiency. Increasing PEI droplet velocity at the nozzle exits from 0.7 to 1.3 m s^{-1} (Figure 4.2d) could promote its deposition from 6.6% to 12.0% (Figure S4.5a). Furthermore, due to the larger size and consequent greater momentum, PEI droplets exhibited a 12.0% deposition efficiency compared to 1.2% for PSS droplets (Figure S4.5b).

We then estimated the diameter of a (completely dried) PE particle from a droplet by the one-droplet-one-particle (ODOP) principle based on mass conservation (Wang et al., 2012; Wang et al., 2009; Wang et al., 2007).

$$D_p = D_d(C/\rho)^{1/3} \tag{4.1}$$

where D_d and D_p are the diameters of the droplet from the nebulizer and the dried particle, respectively, C is the concentration of the precursor PE solution, and ρ is the density of that PE.

Based on Eq. 4.1, a 2.9 μm PEI droplet corresponds to a PEI particle diameter of 574 nm, while a 2.4 μm PSS droplet corresponds to a PSS particle diameter of 651 nm. We then measured the sizes of the deposited PE particles by AFM (Figure 4.3b) and TEM (Figure S4.6). The AFM analysis shows the PEI particles have a peak diameter of ca.14 nm, and the deposited PSS particles have a peak diameter of ca. 12 nm. Obviously, the measured sizes from AFM (also those estimated from the TEM images) were smaller than the calculated sizes from the ODOP principle, suggesting that the droplets do not evaporate completely when they reach the substrate. Instead, the droplets spread upon their impaction on the substrate, leading to the distribution of the PE over the surface, thereby forming smaller PE particles.

4.3.2 Membrane Formation Mechanism

4.3.2.1 Formation of a Polyelectrolyte Layer

Based on the above aerosol deposition analysis, we prepared PEM membranes under the optimal condition of maximum deposition efficiency (i.e., 1 bar). By continuous spraying, more PEs were deposited over the substrate, leading to the gradual formation of a PE layer (Figure 4.3a). We measured the growth kinetics of the PE layer with scan numbers by analyzing the corresponding cross-sectional SEM images (Figure S4.7). As the scan number increased, the deposited PE amount also increased, resulting in a proportional increase in the thickness of the PE layer (Figure 4.3c). To better understand the PE layer structure, two conceptual structural models were established, as schemed in Text S4.6. The first model is a solid film made of PEs (solid film model), devoid of any porosity; the other model is a film of orderly packed PE spheres (packed sphere model), with a theoretical void space of 48% (Figure S4.8). The calculated thicknesses of the PEI_3 layer in the solid film and packed sphere models were 98 nm and 188 nm, respectively; and the thicknesses of the PSS_3 layer in the solid film and packed sphere models were 56 nm and 107 nm, respectively (Table S4.1). The thicknesses of the PEI_3 and PSS_3 layers were measured to be 109 ± 26 nm and 96 ± 17 nm, respectively, from the SEM images (Figure S4.7), falling within the range between those of the solid film and packed sphere models. Based on the conceptual models, the actual PE layer structure is tightly packed. After impingement, the droplets spread, and the deposited PE within the droplets undergoes migration due to diffusion and/or electrostatic attraction (Haynie et al., 2011). They eventually assemble into a thin film (Felton, 2013). Moreover, the growth of the PEI or PSS layer followed a linear pattern (Figure 4.3c, R^2 = 0.96-0.99), with a rate of ca. 44 nm/scan, suggesting uniform intermolecular interactions along the depth of the layer. Porcel et al. (2005) have also reported that the layer thickness increases linearly with the spraying time.

Although the PEM may shrink in thickness due to water removal under the vacuum condition for SEM, the linear increase trend in thickness matches the ellipsometry measurements in air (Azinfar et al., 2021; Cranston and Gray, 2006).

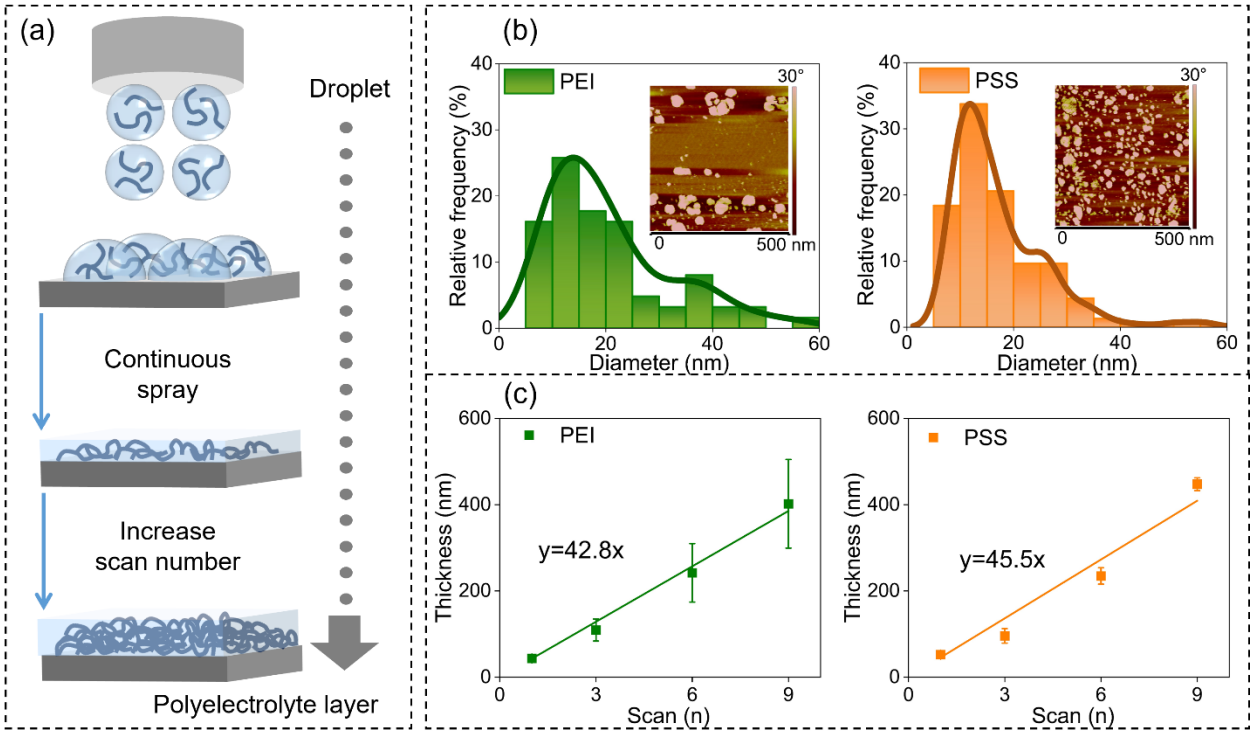

Figure 4.3 (a) Schematic of a PE layer formation showcasing the transformation from droplets into a complete PE layer; (b) size distribution of deposited PEI and PSS particles on the silicon wafer, and the inset figures are representative phase AFM images; (c) variation in the thickness of the PEI and PSS layers with different scans obtained from analysis of cross-sectional SEM images.

Another interesting observation is that the printing mode by moving the nozzle resulted in even deposition of PEs. To visualize the difference, we deposited polyethylene blue dyes on the substrate in both fixed and moving nozzle modes. There was an uneven deposition of dyes under the fixed nozzle mode, showing a ring-shaped pattern (Figure S4.9a), with more deposition on the

right side than on the left side. This result is consistent with the simulation result (Figure 4.2e), which shows that the higher velocity on the right side leads to increased momentum and, consequently, more significant deposition in that area. This non-uniform distribution of momentum is due to the bending of the spray tube. In the printing mode, however, the center of the nozzle passed over the entire substrate, resulting in even deposition of droplets (Figure S4.9b).

4.3.2.2 Polyelectrolyte Multilayer Assembly

The PEM assembly was monitored by ATR-FTIR (Figure 4.4a). The peak at approximately 1690 cm^{-1} corresponds to the C=O bond in the COO^- group, which results from the hydrolysis of the C≡N groups under alkaline conditions (Zhao and Wang, 2017). This characteristic peak became less intensive when the amount of deposited PEI and PSS increased (Figure 4.4a). The peaks at 1178, 1124, 1035, and 1007 cm^{-1} are assigned to the asymmetric and symmetric stretching of S=O in PSS (Alemu et al., 2012). The existence of these peaks verifies the successful deposition of PSS onto the membrane. Raman mapping images offer visible information about the distribution of PEs on the surface, displaying alternating assembly and even dispersion of oppositely charged PEs as illustrated in Figure S4.10. The streaming zeta potential became more positive after PEI deposition and more negative after PSS deposition (Figure S4.11). Moreover, the change of water contact angle followed a similar zig-zag pattern (Figure S4.12). The PSS-terminated PEM membranes were more hydrophilic than the PEI-terminated PEM membranes, because the negatively charged $-SO_3$ functional groups tend to form hydrogen bonds with water, leading to a lower water contact angle (Liu et al., 2015; Qi et al., 2012).

The top-view FESEM images (Figure 4.4b) show the morphology of the pristine substrate and the PEM membranes. For the $(PEI_3PSS_3)_1$ membrane, smaller pores can be apparently observed when compared with the HPAN substrate. For the $(PEI_3PSS_3)_2$ membrane, the surface layer

became much denser without obvious defects. Furthermore, the $(PEI_3PSS_3)_2$ membrane exhibited a smooth and compact surface (Figure S4.13). The ultrafine droplets were evenly distributed on the substrate, leading to uniform coverage. Other spray methods, such as spray gun and airbrush, generate larger droplets which lead to island-shaped deposition on a substrate and cause larger roughness (e.g., Ra is ca. 15 nm) (Xiang et al., 2015).

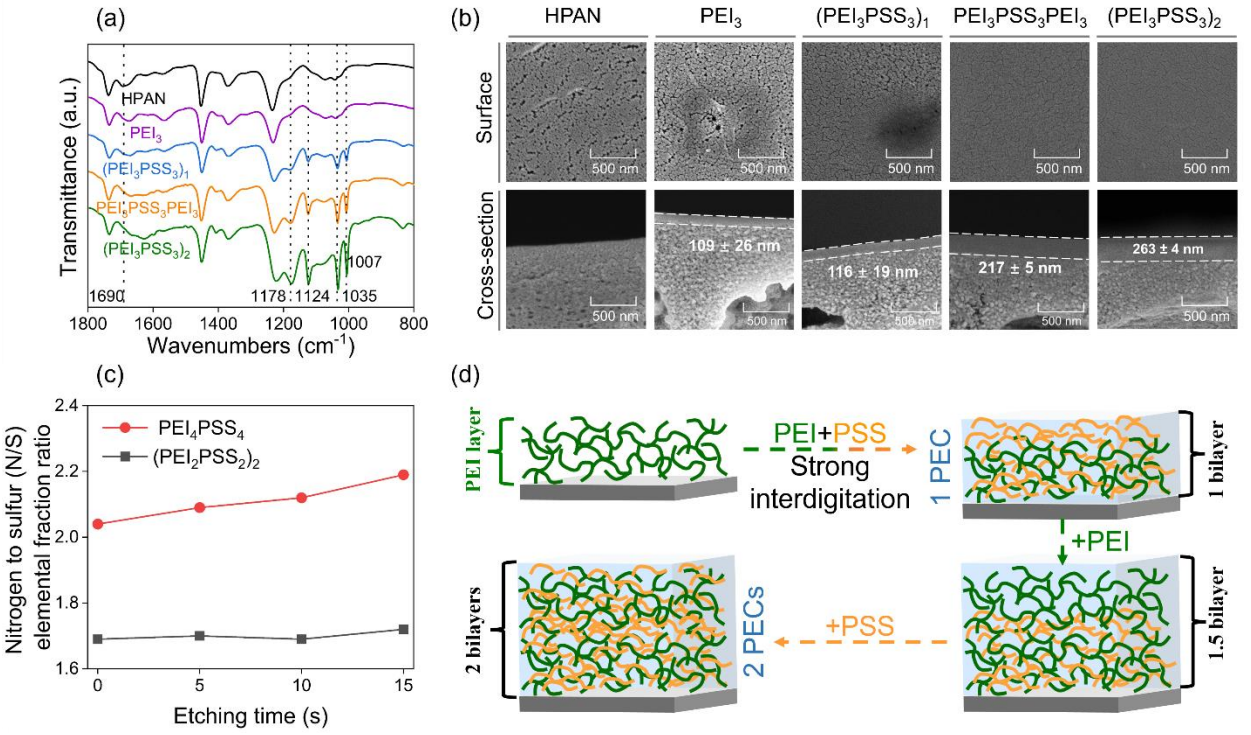

Figure 4.4 Surface characterization of the $(PEI_nPSS_n)_x$ membranes with different bilayer numbers and scans for each single layer. (a) FTIR spectra, (b) surface and cross-section SEM images, (c) the ratios of elemental fraction of nitrogen (N) to sulfur (S) of the $(PEI_2PSS_2)_2$ and PEI_4PSS_4 membranes determined from the XPS depth profiling analysis, and (d) corresponding schematic of PEM assembly.

The measurement of the thickness of the PEM from the cross-section SEM images reveals the thickness grows with layering (Figure S4.14a, b). However, as shown in Figure 4.4b, the PEI_3 layer

has a similar thickness (109 ± 26 nm) to the PEI_3PSS_3 membrane (116 ± 19 nm), and the $PEI_3PSS_3PEI_3$ membrane thickness (217 ± 5 nm) approaches that of the $(PEI_3PSS_3)_2$ membrane (263 ± 4 nm). The data shows that the addition of a PSS layer does not double the thickness of the PEM, but instead, only increases the thickness by ≤ 20%. Moreover, for the one-bilayer membranes, the thickness growth shows a linear pattern with a rate of ca. 46 nm/scan (Figure S4.14c, $R^2 = 0.99$), which is about half the combined thickness of the PEI layer plus the PSS layer (88 nm/scan, Figure 4.3c); for the two-bilayer membranes, the thickness exhibits also a linear growth from one to five scans with a rate of ca. 87 nm/scan (Figure S4.14d, $R^2 = 0.99$), also about half the combined thickness of (PEI+PSS+PEI+PSS) (i.e., 177 nm/scan, Figure 4.3c). Regardless of the number of scans, the thickness of the two-bilayer membrane is approximately twice that of the one-bilayer membrane (Figure S4.14). The occurrence of this unique growth pattern is attributed to the interdigitation of PEI and PSS within the PEM structure. We speculate that during the PEM assembly, two adjacent oppositely charged PE layers are strongly interdigitated (Castelnovo and Joanny, 2000), forming a polyelectrolyte complex (PEC) layer instead of a perfect layer-by-layer assembly. This strong interdigitation is likely due to the deep penetration of PSS. The diffusion of PE molecules within the PEM is a widely observed phenomenon (Gilbert et al., 2013; Picart et al., 2002; Sill et al., 2019; Sill et al., 2021; Taketa et al., 2020; Zacharia et al., 2007). For example, Gilbert et al. (2013) have used XPS depth profiling to prove the diffusion of chitosan within the PEM of PAA and poly(ethylene oxide). Taketa et al. (2020) have also found that PSS can diffuse within carboxymethyl cellulose/chitosan multilayers through XPS depth profiling.

To explore the internal architecture of the PEM, especially the interdigitation between PEI and PSS, XPS depth profiling was employed to examine the $(PEI_2PSS_2)_2$ and PEI_4PSS_4 membranes, two membranes with theoretically the same material but different assembled structures. The

nitrogen (N) and sulfur (S) elements were used to represent the PEI and PSS, respectively, and their N/S atomic ratio was analyzed to evaluate the relative distribution of PEI and PSS within the PEM structure. After optimization, the XPS depth profiling was conducted at the etching time of 5 s, 10 s, 15 s, and 20 s to obtain elemental information at different depths of the PEM's internal structure. The N/S ratios of the $(PEI_2PSS_2)_2$ membrane were consistent at ca. 1.7 from 0 to 15 s (Figure 4.4c), indicating a uniform distribution of the PEI and PSS components throughout the PEM structure. This observation suggests the formation of a well-intermixed and homogeneous PEC within the $(PEI_2PSS_2)_2$ multilayer. However, for the PEI_4PSS_4 membrane, the N/S ratios increased from 2.0 to 2.2 with increasing etching time from 0 to 15 s (Figure 4.4c). The increased N/S ratios for the PEI_4PSS_4 membrane suggest a reduced degree of penetration of PSS from the top. This difference is understandable because it is more difficult to well mix two thicker polyelectrolyte layers (i.e., a PEI_4 layer and a PSS_4 layer). At the etching time of 20 s, the N/S ratios of $(PEI_2PSS_2)_2$ and PEI_4PSS_4 membranes increased significantly to 2.7 and 5.0, respectively, indicating the reaching of the underlying HPAN substrate. In conclusion, the XPS depth profiling analysis confirms the formation of interdigitated PECs as illustrated in Figure 4.4d.

4.3.3 Membrane Filtration Performance

4.3.3.1 Water Flux and Molecular Weight Cut Off

The PE deposition mass increases with more scans, which expectedly increases overall membrane resistance and decreases PWP (Figure 4.5a). The HPAN substrate had a PWP of 208.8 ± 21.4 L m^{-2} h^{-1} bar^{-1}. When the PEI layer was the terminal layer, the PWP did not decrease with increased scans, because the PEI layer did not exert significant resistance to water transport due to its swelling in water (Scheepers et al., 2023; Zhu et al., 2006). Following subsequent PSS and PEI alternative deposition, the PWP decreased as the bilayer number increased (Figure 4.5a). The PWP

decreased from 12.0 ± 0.8 L m^{-2} h^{-1} bar^{-1} (one-bilayer membranes) to 5.4 ± 1.3 L m^{-2} h^{-1} bar^{-1} (two-bilayer membranes) under three scans condition. For the two-bilayer membranes, the PWP of PEM membranes decreased from 13.3 to 3.3 L m^{-2} h^{-1} bar^{-1} when the scan number increased from one to five. The PWP reduction is attributed to the effective barrier generated by the interdigitated PEI and PSS chains on the substrate surface (Ng et al., 2013). This is in accordance with the fact that the thickness of the layers increases with more bilayers (Figure 4.4b), thereby engendering higher overall hydraulic resistance.

Moreover, the observed rejections (R_{obs}) of neutral organic compounds of increasing molecular weights were evaluated (Figure S4.15a, b), and the intrinsic rejections were calculated based on the experimentally obtained mass transfer coefficients (details in Text S4.4, and data in Table S4.2) (Bason et al., 2010). The MWCO values were determined from the rejection curves as the molecular weight corresponding to a 90% rejection, and the intrinsic rejections were fitted by the steric hindrance pore model to obtain the pore size of the PEM membranes (Text S4.5) (Boo et al., 2018b; DuChanois et al., 2019). The pore sizes estimated from the test of each organic solute were averaged to obtain the pore size for each membrane (Boo et al., 2018b; Dang et al., 2014). Overall, the MWCO of the PEM membranes decreased with the increase of scan numbers, and the MWCO of all the one-bilayer membranes was larger than 342 Da (Figure 4.5b, c). As the scan number increased from one to five, the corresponding mean pore radii of the one-bilayer membranes decreased from 0.56 to 0.46 nm (Figure 4.5d). As the scan number increased from one to three, the mean pore radii of the two-bilayer membranes decreased from 0.56 to 0.40 nm (Figure 4.5d), which falls within the range for NF membranes (Zhao et al., 2021). There was little difference among $(PEI_3PSS_3)_2$, $(PEI_4PSS_4)_2$, and $(PEI_5PSS_5)_2$, whose average pore radii were ca. 0.40 nm. The two-bilayer membranes had a smaller pore radius than the one-bilayer membranes when the

scan number was the same (n=2-5), except in the case of one scan (Figure 4.5d). This was likely due to too few PE materials deposited under one scan, which did not form a selective PE layer. The observed trend of decreasing PWP with increasing bilayer number can be attributed to the smaller pore radius and increased thickness of the PEM with repeated LbL deposition cycles.

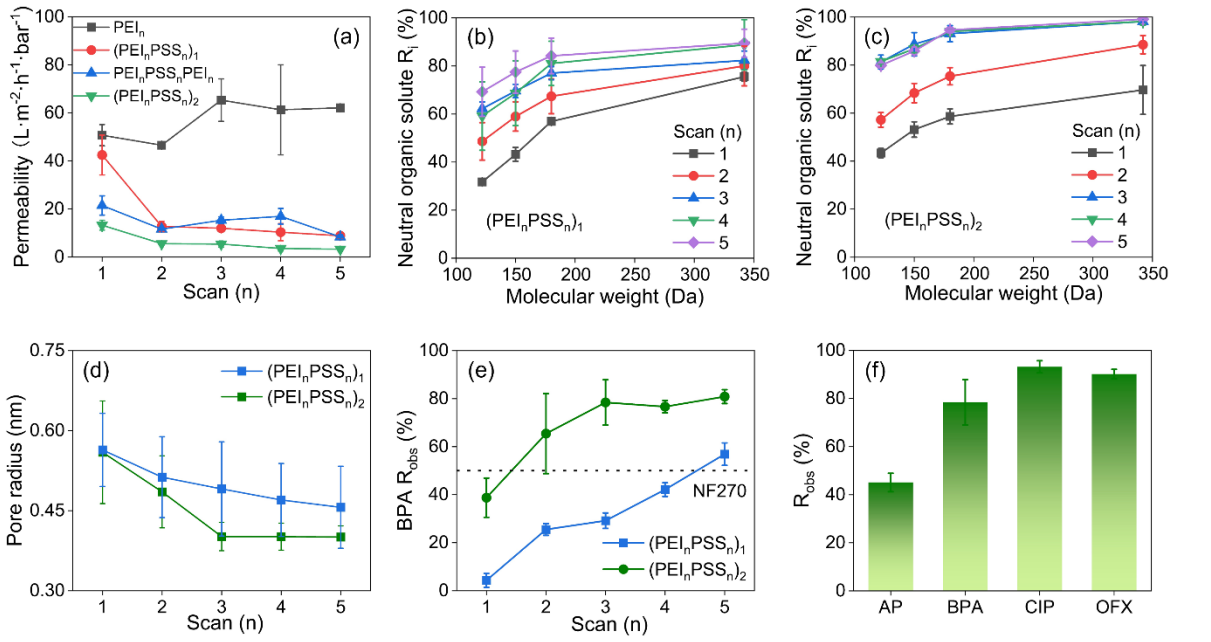

Figure 4.5 Filtration performance and pore characteristics of the $(PEI_nPSS_n)_x$ membranes with different bilayer numbers and scans: (a) PWP, (b) intrinsic rejection (R_i) of neutral organic solutes by the one-bilayer $(PEI_nPSS_n)_1$ membranes, (c) intrinsic rejection (R_i) of neutral organic solutes by the two-bilayer $(PEI_nPSS_n)_2$ membranes, (d) estimated mean pore radius, (e) observed rejection of BPA (BPA R_{obs}), and (f) observed rejection (R_{obs}) of AP, BPA, CIP, and OFX by the $(PEI_3PSS_3)_2$ membrane.

The Na_2SO_4 rejection of the one-bilayer membranes increased from 16% to 55% when the printing scan increased from one to five (Figure S4.16a). The Na_2SO_4 rejection of the two-bilayer

membranes ranged from 47% to 58%. The respective hydration radii of 0.36 and 0.38 nm for Na^+ and SO_4^{2-} (Liang et al., 2020) are smaller than the smallest pore radius (0.40 nm) of all the PEM membranes in our study. The Na_2SO_4 rejection by the resultant PEM membranes is predominantly governed by electrostatic repulsion. We further evaluated the rejection of various salts by the $(PEI_3PSS_3)_2$ membrane, and the results further confirmed the significant role of electrostatic interactions in ion rejection. The NaCl rejection was 22%, the rejections of Na_2SO_4 and $MgSO_4$ were 58% and 34%, respectively, and the $MgCl_2$ rejection was 13% (Figure S4.16b). As the $(PEI_3PSS_3)_2$ membranes are negatively charged, they are effective in rejecting salts with divalent anions. The negatively charged top PSS layer of the PEM membranes facilitates the transport of Mg^{2+} ions, resulting in a low rejection of $MgCl_2$. The Na_2SO_4 rejection of $(PEI_3PSS_3)_2$ membrane in Chapter 4 was 58%, significantly higher than the 25% obtained in Chapter 3. The membrane area was scaled up from 8 cm^2 in Chapter 3 to 64.8 cm^2 in Chapter 4. Despite employing the same printing scan strategy and bilayer number, the larger sprayed substrate resulted in higher material deposition (Figure S3.3), which likely contributed to the enhanced salt rejection

The one-bilayer PEM membranes can effectively retain pollutants with large molecular weight like humic acid (> 90% rejection regardless of the scan numbers, Figure S4.17) while maintaining high water permeability. The two-bilayer PEM membrane can remove various types of micropollutants. Furthermore, in the long-term filtration process lasting 96 h, the $(PEI_3PSS_3)_2$ membrane maintained a steady state in terms of pure water permeability and the rejection of glucose and Na_2SO_4 (Figure S4.18). The above results show that the filtration performance and mean pore radius of the PEM membranes can be tailored by simultaneously tuning the scan and bilayer numbers.

4.3.3.2 Retention of Micropollutants

As the scan number increased from one to five, the BPA rejection of the one-bilayer membranes increased from 12.7 % to 67.9% (Figure 4.5e). Furthermore, the enhanced rejection performance with increased bilayer number was more obvious than with increased scans. As for the two-bilayer membranes, the BPA rejection increased from 38.7% to 80.8% with scans increasing from one to five. The highest BPA rejection of the two-bilayer membranes was 80.8%, which is superior to that of the commercial NF270 membranes (ca. 40%) (Zhang et al., 2019), (Yuksel et al., 2013). To elucidate the mechanisms underlying the enhanced BPA rejection, we also conducted similar experiments to obtain the mass transfer coefficient of the NF270 membrane and its intrinsic rejections of neutral solutes. The MWCO of NF270 was ca. 290 Da based on observed rejections of these sugars, which is consistent with the literature values (Gao et al., 2022; Wang et al., 2022b). Based on intrinsic rejections, its MWCO was ca. 160 Da (Figure S4.15c), which was similar to that of the $(PEI_3PSS_3)_2$ membrane. However, the intrinsic rejection of BPA by the $(PEI_3PSS_3)_2$ membrane was still higher than that by the NF270 membranes (Figure S4.19), which suggests size exclusion is not the only factor determining its rejection. Since the charge of BPA is neutral at pH 7 (pK_{a1} = 9.6, and pK_{a2} = 10.2) (Choi and Lee, 2017). The electrostatic repulsion effect is considered negligible in this case. Therefore, the lower rejection of BPA by the NF 270 membrane is likely because the rates of sorption and transmission of BPA across a (more) hydrophobic NF270 membrane are considerably increased by hydrophobic interactions (Guo et al., 2016).

We further evaluated the rejection of the AP (188 $g \cdot mol^{-1}$), BPA (228 $g \cdot mol^{-1}$), CIP (331 $g \cdot mol^{-1}$), and OFX (361 $g \cdot mol^{-1}$) by the $(PEI_3PSS_3)_2$ membrane. The rejection trend of these four micropollutants followed the size exclusion mechanism in accordance with the MWCO (294 $g \cdot mol^{-1}$ based on observed rejections) of the membrane. As shown in Figure 4.5f, only 45.1% of

AP was retained, while CIP and OFX exhibited rejection exceeding 90%. This high rejection of CIP and OFX demonstrates the $(PEI_3PSS_3)_2$ membrane to be defect-free.

4.4 Conclusion

Our AAP method has the advantage of low time and material consumption compared to the conventional dip coating. For example, the $(PEI_3PSS_3)_2$ membrane with an area of 64.8 cm^2 was fabricated using only 18 min (Text S4.1) and 6 mL of the PE solution. And the fabrication time can be further decreased by using more spray nozzles. In contrast, using dip-coating to obtain a two-bilayer PEM membrane requires a minimum of several hours and hundreds of milliliters of solution (Gopalakrishnan et al., 2024; Liang and Lin, 2021; Scheepers et al., 2023). The rapid, controlled, and efficient deposition of polyelectrolytes is a key advantage of our AAP method, making it promising for various applications requiring thin, uniform coatings. The obtained membranes have comparable structure and separation performance to those obtained via dip coating. Ranging from loose to dense NF, these membranes are well-suited for various water treatment applications, from micropollutant removal to humic acid filtration.

Future efforts can be devoted to adjusting the PEM structure to achieve synergistic control of pore and charge properties. The current PEM membranes exhibit a mild negative charge and thus a moderate Na_2SO_4 rejection of ca. 60% (Figure S4.16), due to low PSS deposition. By adjusting the composition and layering of PEs, the desirable separation of charged ions can be obtained. Furthermore, incorporating additives into PE solutions allows additional functionalities and further improvement of membrane properties (e.g., permeability, selectivity, stability, and chlorine resistance). Lastly, the AAP method enables the deposition of PE and other materials onto complex geometries, including three-dimensional structures. This capability opens up possibilities for manufacturing membranes with intricate designs.

Acknowledgement

This work was supported by Hong Kong Research Grants Council's General Research Fund Scheme (15214222) and Science, Technology and Innovation Commission of Shenzhen Municipality (SGDX20210823103401009).

Appendix B: Supporting Information for Chapter 4

Test S4.1 Aerosol-assisted printing (AAP) method

The AAP process was invented to produce an evenly distributed surface coating in a step-by-step fashion with a high degree of reproducibility. Here, line-by-line and column-by-column procedures are denoted as one scan, which is used for the polyelectrolyte (PE) coating on substrates. As shown in Figure S4.1a, the line-by-line procedure began along the x-axis, with the nozzle moving from the right end of the substrate to the left end. After completing each line, the nozzle moved 7 mm below the y-axis to start the next line, repeating this pattern until the entire substrate was covered. Subsequently, column-by-column procedures started in the y-axis direction (Figure S4.1b). The nozzle started from the top of the substrate and moved continuously towards the bottom until reaching the end. After each column was completed, the nozzle moved 7 mm along the x-axis to begin the next column, following the same pattern until the coverage of the entire substrate was completed. This printing procedure ensures that the entire substrate is coated in a stripwise manner, resulting in a homogenous coating across the entire surface. Moreover, the overlapping region between adjacent spray lines is carefully defined to ensure consistent coverage and uniformity.

The substrate length is 108 mm, and the width is 60 mm. According to the line-by-line procedure, the calculation process of the total time required for one scan is shown as follows:

$$T = T_x + T_y \quad \text{(S4.1)}$$

$$T_x = \frac{L_s}{v} \times \frac{W_s}{d} + \frac{2W_s}{v} \quad \text{(S4.2)}$$

$$T_y = \frac{W_s}{v} \times \frac{L_s}{d} + \frac{2L_s}{v} \quad \text{(S4.3)}$$

in which T_x and is T_y the required time for the nozzle moving the entire substrate when it begins in the x-axis and y-axis direction, respectively. L_s and W_s are the substrate length and width, respectively. The v is the nozzle moving speed and d is the line spacing.

Text S4.2 Aerosol deposition characterization

Advanced in-line and off-line characterization and modelling techniques were used to analyze the PE deposition process. The velocity field of the aerosol flow was monitored by a 2D mini laser Doppler velocimetry (LDV). The continuous output beam was divided into two beams of equal intensity by a beam splitter. The laser in channel 1 was performed at a 658 nm wavelength and used for aerosol velocity measurement in a vertical direction. The laser in channel 2 was performed at an 830 nm wavelength and used for aerosol velocity measurement in a horizontal direction. A schematic diagram of the aerosol flow with the measurement points was shown in Figure S4.2.

Text S4.3 Chemical analysis and membrane composition analysis.

The concentration of micropollutants was detected by a high-performance liquid chromatography (HPLC) instrument equipped with a Waters 515 pump, a Waters 2489 dual absorbance detector, a Waters 717 plus autosampler, and a photodiode array UV-vis detector. A sample volume of 40 μL was injected into an Agilent ZORBAX Extend-C18 column (4.6 × 250

mm, 5 μm). HPLC-grade acetonitrile (ACN), methanol (MeOH), and pure water (MiliQ) were used as the mobile phases (Regents DUKSAN). BPA concentration was measured at a 225 nm wavelength and using a mobile phase containing 75% water and 25% MeOH. AP concentration was detected at the wavelength of 261 nm and a mobile phase containing 75% water and 25% ACN. OFX concentration was determined at the wavelength of 294 nm and a mobile phase containing 74.9% water, 25% ACN, and 0.1% formic acid. CIP concentration was measured at the wavelength of 276 nm and a mobile phase containing 64.5% water, 20% ACN, 0.5% formic acid, and 15% MeOH. Single salt rejections were evaluated using 100 mg L^{-1} of NaCl, Na_2SO_4, $MgCl_2$, and $MgSO_4$ solutions. The conductivity of the feed and permeate solutions was determined using a conductivity meter (FE38, Mettler Toledo).

The elemental composition of the PEM membrane was analyzed using X-ray photoelectron spectroscopy (XPS, Nexsa G2 surface analysis system, Thermo Fisher Scientific). The XPS survey spectra was collected using scanning monochromated Al source (1486.6 eV; 72 W; 400 μm spot size). The takeoff angle was 60° from the vertical direction, and the X-ray beam collected C1s, N1s, O1s, and S2p elemental information while rastering over an area with a diameter of 1.2 mm. Depth profiling was accomplished using the instrument's Ar^+ ion source operated at 12 keV. The collected data were charge-corrected, referencing the binding energy of the carbon-carbon bond to 284.8 eV.

Text S4.4 Concentration polarization analysis

Concentration polarization (CP) always occurs in the membrane separation process where the concentration of solutes near the membrane surface significantly differs from that in the bulk solution. As a result, a layer of a higher concentration, or a concentration gradient forms on the

feed side of the membrane surface which is confined to the boundary layer. The boundary layer can significantly affect membrane NF performance such as permeability and selectivity alteration (Bason and Freger, 2010; Bason et al., 2010).

The mass balance equation (Eq. S4.4) can be integrated over the boundary layer to give the well-known polarization equation and is shown as follows:

$$\frac{C_m - C_p}{C_b - C_p} = \exp\left(\frac{J_v}{K_m}\right) \quad \text{(S4.4)}$$

where C_m is the concentration of solute in the feed solution at the membrane surface, C_p is the permeate concentration, C_b is the bulk solution concentration, J_v is the volume flux in the boundary layer generated by permeate flow through the membrane. And K_m is the mass transfer coefficient.

An alternative form of Eq. S4.4 replaces the concentration terms by the rejection R. The observed rejection (R_{obs}) is $1-C_p/C_b$, the intrinsic rejection (R_i) is $1-C_p/C_m$, and Eq. S4.4 can be written as follows:

$$\frac{(1 - R_{obs})/R_{obs}}{(1 - R)/R} = \exp\left(\frac{J_v}{K_m}\right) \quad \text{(S4.5)}$$

$$\ln\frac{(1 - R_{obs})}{R_{obs}} = \ln\frac{1 - R_i}{R_i} + \frac{J_v}{K_m} \quad \text{(S4.6)}$$

Further, K_m can be calculated using the following equation:

$$K_m = v^{1/2} D^{2/3} K^* \quad \text{(S4.7)}$$

where v is the cross-flow velocity, D is the diffusion coefficient of the solute in water, and K^* is the "normalized" parameter which is calculated from plots of $\ln[(1-R_{obs})/R_{obs}]$ versus $J_v/v^{1/2}D^{2/3}$ and averaged for all experiments.

The mass transfer coefficients K_m were determined as described above to obtain the R_i for organic solutes, including erythritol, xylose, glucose, and sucrose. At constant feed composition and transmembrane pressure of 5 bar, the cross-flow velocity varied from 38.5 to 106.8 cm s^{-1}.

The corrected feed concentration C_m is obtained using the following equation:

$$C_m = (C_b - C_p) \exp\left(\frac{J_v}{K_m}\right) + C_p \quad \text{(S4.8)}$$

Text S4.5 Membrane pore size analysis.

In the steric hindrance pore model, the membrane pores are modeled as cylindrical capillary tubes having an identical radius (Deen, 1987; Nghiem et al., 2004). The uncharged solutes are assumed to be spherical solute particles, and only the diffusive and convective flows affect the transport of solutes inside the membrane. The average pore size of the polyelectrolyte multilayer (PEM) can be estimated theoretically by fitting the rejection of four reference organic solutes (erythritol, xylose, glucose, and sucrose) using the following equation.

$$R = 1 - \frac{\Phi K_C}{1 - \exp(-Pe)(1 - \Phi K_C)} \quad \text{(S4.9)}$$

in which K_c is the hindrance factor and Φ is the distribution coefficient, which depicts the solute particle distribution at the solution-membrane pore interface.

$$\Phi = \frac{c_s}{c} = (1 - \lambda)^2 = (1 - \frac{r_s}{r_p})^2 \quad \text{(S4.10)}$$

in which c_s is the average solute concentration within the pore, c is the concentration outside the pore and λ is the ratio of the solute Stokes radius (r_s) to the membrane average pore radius (r_p).

For uncharged solutes, only the diffusive and convective flows affect the transport of solutes inside the membrane. The Peclet number (Pe) is defined as

$$Pe = \frac{K_c J_w \delta}{K_d D_\infty \varepsilon} \quad \text{(S4.11)}$$

where J_w is the permeate flux, K_d is the diffusion hindrance coefficient, D_∞ is the solute diffusion coefficient in water, δ and ε are the thickness and porosity of the membrane active layer, respectively. The two hindrance coefficients K_c and K_d (Liu et al., 2019), could be calculated by

$$K_c = 1.0 + 0.054\lambda - 0.988\lambda^2 + 0.0441\lambda^3 \ (\lambda \leq 0.8) \quad \text{(S4.12)}$$

$$K_c = -6.830 + 19.348\lambda - 12.518\lambda^2 \ (0.8 < \lambda \leq 1) \quad \text{(S4.13)}$$

$$K_d = 1.0 - 2.30\lambda + 1.154\lambda^2 + 0.224\lambda^3 \ (\lambda \leq 0.8) \quad \text{(S4.14)}$$

$$K_d = -0.105 + 0.318\lambda - 0.213\lambda^2 \ (0.8 < \lambda \leq 1) \quad \text{(S4.15)}$$

The relationship between the pure water flow and the applied pressure (ΔP) across the membranes is given by the Hagen-Poiseuille equation (Bowen and Mohammad, 1998; Nakao and Kimura, 1981).

$$Jw = \frac{{r_p}^2 \Delta P}{8\mu \frac{\delta}{\varepsilon}} \quad \text{(S4.16)}$$

The solute Stokes radius (r_s) is estimated by the Stokes–Einstein equation:

$$r_s = \frac{TK_b}{6\pi\mu D_\infty} \quad \text{(S4.17)}$$

in which K_b is the Boltzmann constant, and D_∞ is the solute diffusion coefficient in water.

Text S4.6 Polyelectrolyte layer growth analysis

The thickness of the PE layer could be estimated by two conceptual structural models: solid film (compacted) and packed sphere (porous), as schemed in Figure S4.8. In the compacted structure, the PE particles are tightly packed without any void spaces or porosity. This means that the deposited particles form a dense and continuous layer on the substrate, resulting in a solid and impermeable structure. In the porous structure, PE particles are assumed to be spherical. These

particles are deposited in an organized and compact manner on the substrate, and void spaces are formed between the particles, resulting in a porosity of 48% within the PE layer. The equations for calculating thickness are shown as follows:

$$H_1 = \frac{M}{\rho A} \tag{S4.18}$$

$$N_1 = \frac{M}{\frac{4}{3}\pi r^3 \rho} \tag{S4.19}$$

$$N_2 = \frac{A}{4r^2} \tag{S4.20}$$

$$H_2 = \frac{N_1}{N_2} \times 2r \tag{S4.21}$$

where H_1 and H_2 are the thickness of PE layer with compacted and loose structures respectively, M is the total deposited PE particle mass on a membrane coupon, ρ is the PE density, A is the membrane coupon area, and r is the PE particle radius.

Table S4.1 Theoretical thickness of the PEI and PSS layer with three scans.

Polyelectrolyte	r (nm)	A (cm^2)	ρ (g mL^{-1})	H_1 (nm)	H_2 (nm)
PEI	7	16	1.030	98	187
PSS	6	16	0.801	56	107

where r is the PE particle radius, A is the membrane coupon area, ρ is the PE density, and H_1 and H_2 are the thickness of the PE layer with compacted and loose structures, respectively.

Table S4.2 The mass transfer coefficients (K_m) of the $(PEI_nPSS_n)_x$ membranes with different bilayer numbers and scans

PEM Membrane	K^* $(m\ s^{-1})^{1/2}(m^2\ s^{-1})^{-2/3}$	Organic solute	$D \times 10^{-9}$ $(m^2\ s^{-1})$	K_m $(\mu m\ s^{-1})$
$(PEI_1PSS_1)_1$	35.99	Erythritol	0.81	19.40
		Xylose	0.74	18.27
		Glucose	0.67	17.10
		Sucrose	0.52	14.44
$(PEI_2PSS_2)_1$	23.58	Erythritol	0.81	12.71
		Xylose	0.74	11.97
		Glucose	0.67	11.20
		Sucrose	0.52	9.46
$(PEI_3PSS_3)_1$	20.06	Erythritol	0.81	10.82
		Xylose	0.74	10.18
		Glucose	0.67	9.53
		Sucrose	0.52	8.05
$(PEI_4PSS_4)_1$	21.08	Erythritol	0.81	11.36
		Xylose	0.74	10.70
		Glucose	0.67	10.01
		Sucrose	0.52	8.46
$(PEI_5PSS_5)_1$	19.16	Erythritol	0.81	10.33
		Xylose	0.74	9.72
		Glucose	0.67	9.10
		Sucrose	0.52	7.69
$(PEI_1PSS_1)_2$	27.60	Erythritol	0.81	14.88
		Xylose	0.74	14.01
		Glucose	0.67	13.11
		Sucrose	0.52	11.07
$(PEI_2PSS_2)_2$	17.94	Erythritol	0.81	9.67
		Xylose	0.74	9.11
		Glucose	0.67	8.52
		Sucrose	0.52	7.20
$(PEI_3PSS_3)_2$	12.21	Erythritol	0.81	6.58
		Xylose	0.74	6.20
		Glucose	0.67	5.80
		Sucrose	0.52	4.90
$(PEI_4PSS_4)_2$	9.57	Erythritol	0.81	5.16
		Xylose	0.74	4.86
		Glucose	0.67	4.55
		Sucrose	0.52	3.84
$(PEI_5PSS_5)_2$	9.18	Erythritol	0.81	4.95
		Xylose	0.74	4.66
		Glucose	0.67	4.36
		Sucrose	0.52	3.68
NF270	36.50	Erythritol	0.81	19.68
		Xylose	0.74	18.53
		Glucose	0.67	17.34
		Sucrose	0.52	14.64

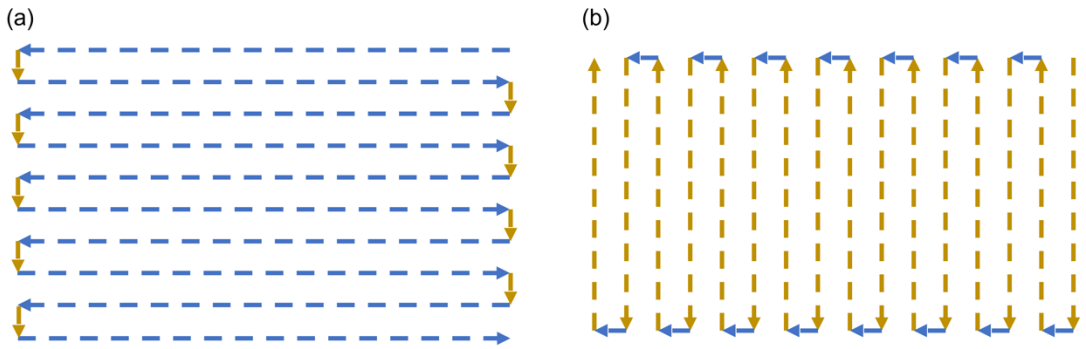

Figure S4.1 Schematic of nozzle movement trajectory in (a) line-by-line procedure and (b) column-by-column procedure.

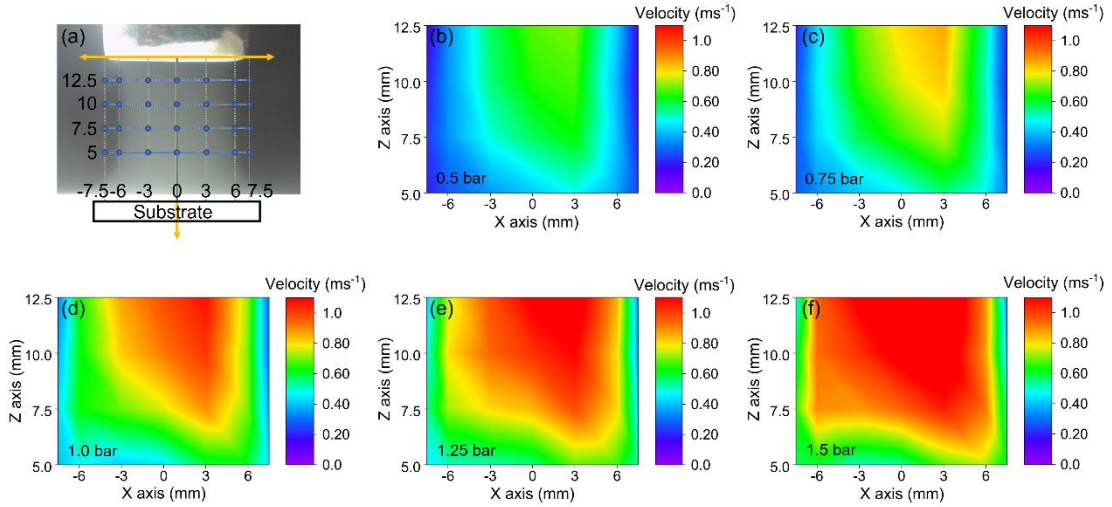

Figure S4.2 (a) Schematic illustration of the measurement points of the aerosol flow from the Collison nebulizer using the laser doppler velocimetry; (b-f) the vertical velocity distribution field of PEI aerosols at the nozzle exit under different nebulizer pressure (0.5, 0.75, 1.0, 1.25, and 1.5 bar, respectively).

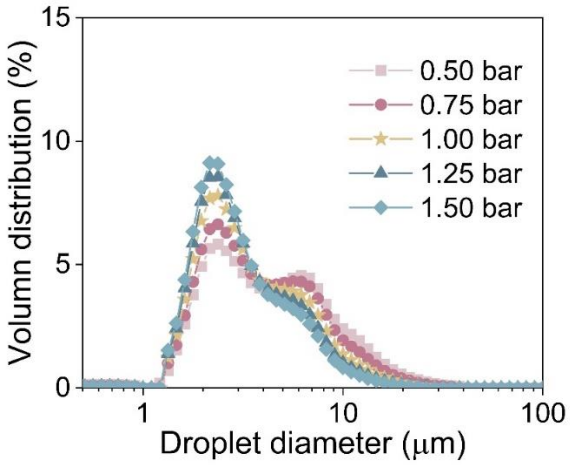

Figure S4.3 Size distribution of water droplets produced under different nebulizer pressures (0.5-1.5 bar) measured by a laser diffraction size analyzer.

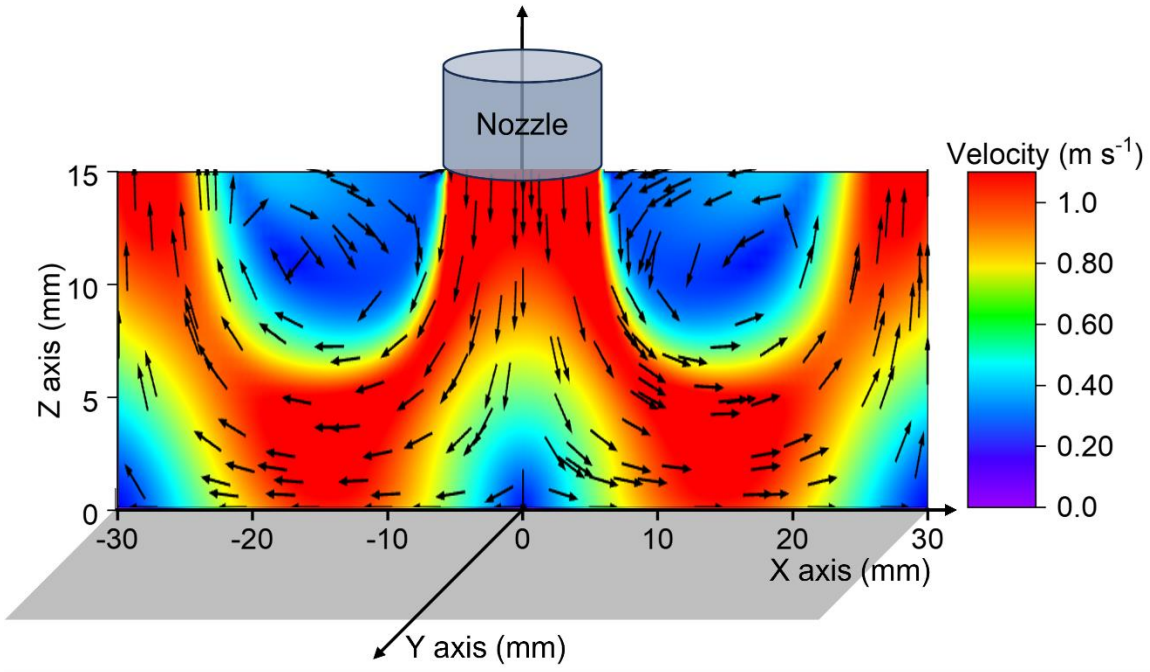

Figure S4.4 The velocity distribution field under nebulizer pressure of 1.5 bar by COMSOL simulation. The simulated 2D region from the nozzle to the membrane substrate is an axis-symmetric region with a length of 60 mm (X axis) and a height of 15 mm (Z axis). The X-Y plate in gray is the substrate.

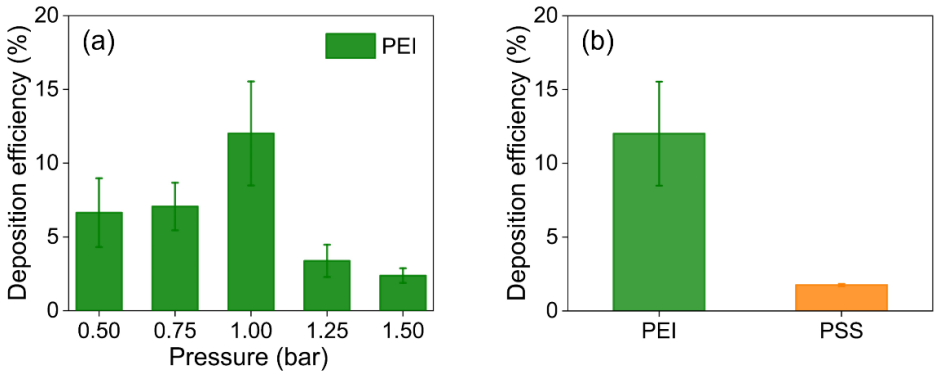

Figure S4.5 (a) PEI deposition efficiency under different nebulizer pressure and (b) comparison of PEI and PSS deposition efficiency under 1 bar nebulizer pressure.

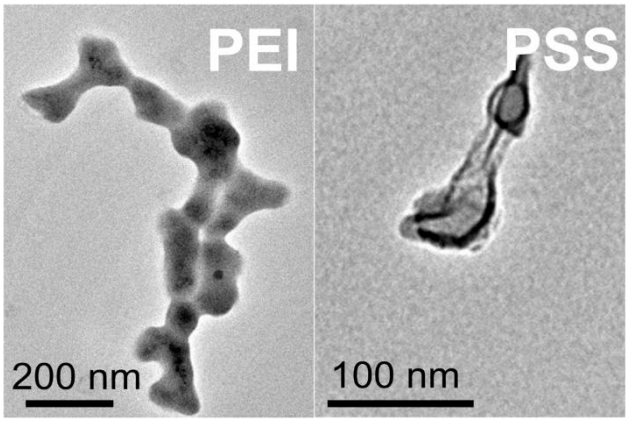

Figure S4.6 Representative TEM images of deposited PEI and PSS particles.

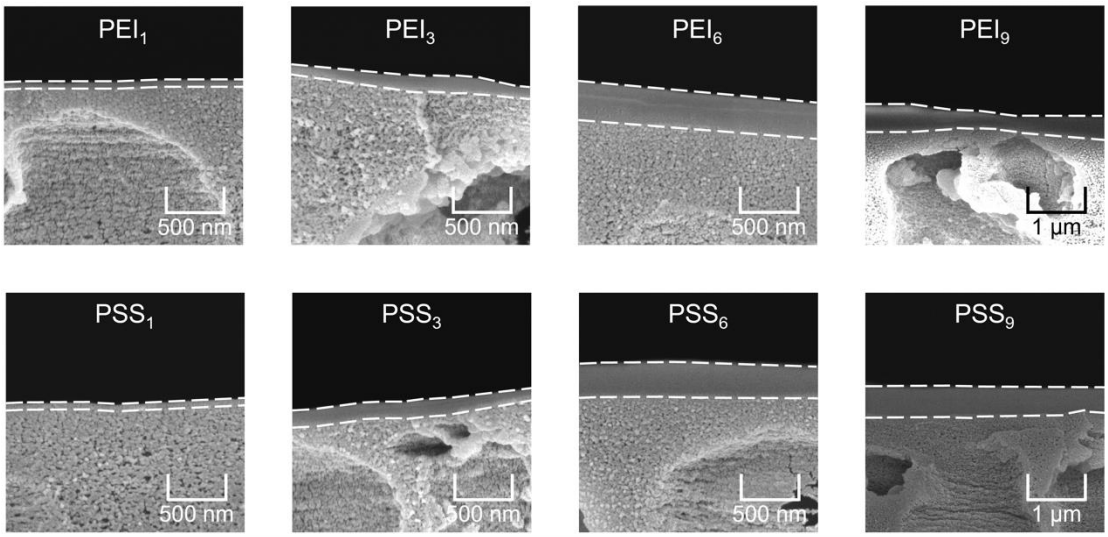

Figure S4.7 Cross-section SEM images of the PEI and PSS layers with different scans (one, three, six, and nine scans, respectively).

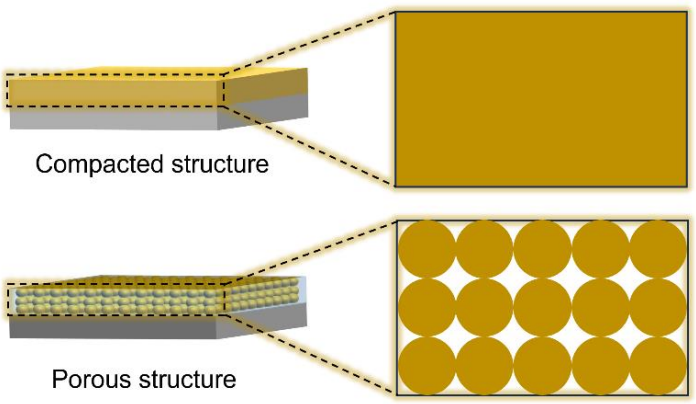

Figure S4.8 Schematics of polyelectrolyte layer structure in the solid film (compacted) model and packed sphere model.

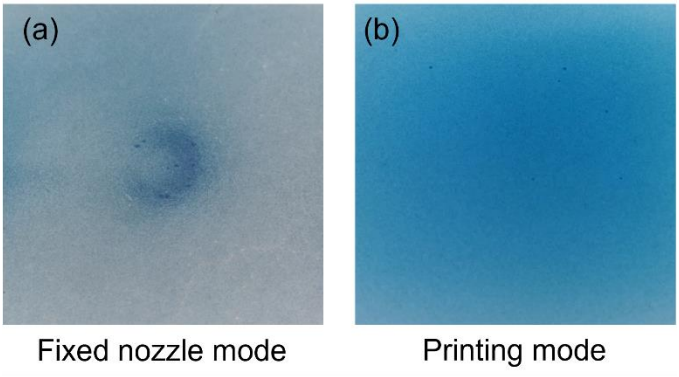

Figure S4.9 Comparison of deposition patterns of polyethylene blue aerosols under the fixed nozzle and printing (moving nozzle in a raster scan) modes.

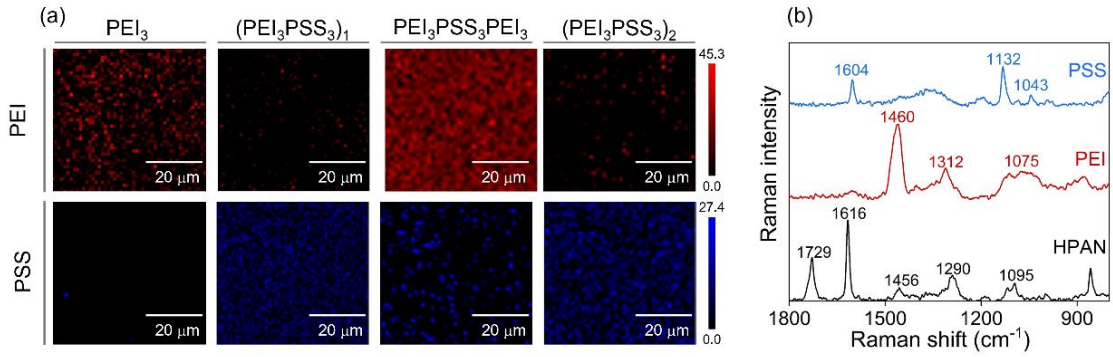

Figure S4.10 (a) Raman mapping images of the (PEInPSSn)x membranes with different bilayer numbers and scans for each single layer; (b) Raman spectra of PEI, PSS, and HPAN. The Raman mapping was performed for identifying the distribution of PEI at the characteristic wavenumber of 1312 cm^{-1}, and for identifying PSS at the characteristic peak of 1043 cm^{-1}.

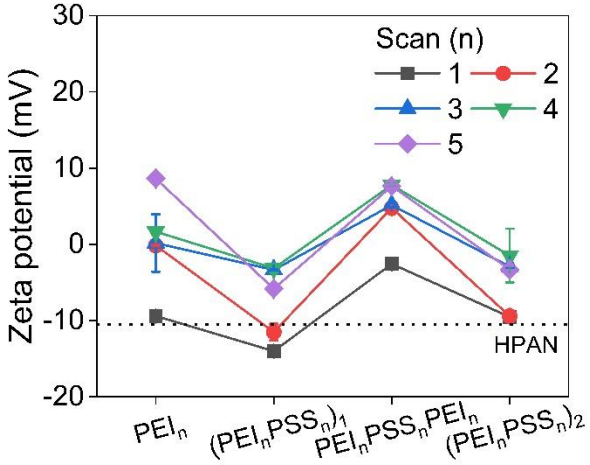

Figure S4.11 Surface zeta potential of the $(PEI_nPSS_n)_x$ membranes with different bilayer numbers and scans for each single layer.

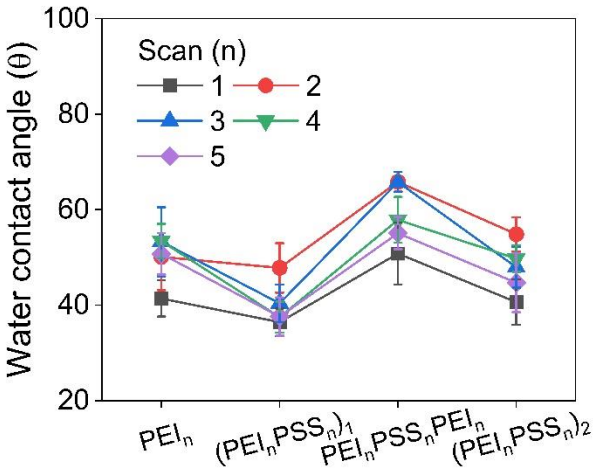

Figure S4.12 Water contact angles of the $(PEI_nPSS_n)_x$ membrane surfaces: PEI_n, $(PEI_nPSS_n)_1$, $PEI_nPSS_nPEI_n$, and $(PEI_nPSS_n)_2$ membranes with different scans. For water contact angle measurement, a 5 μL water droplet was placed on the membrane surface, and the contact angle was captured by a high-definition camera immediately. The measurements were conducted at left and right contact angles from the digital images using the Image J software. Average data was obtained from five random locations with three different membrane samples.

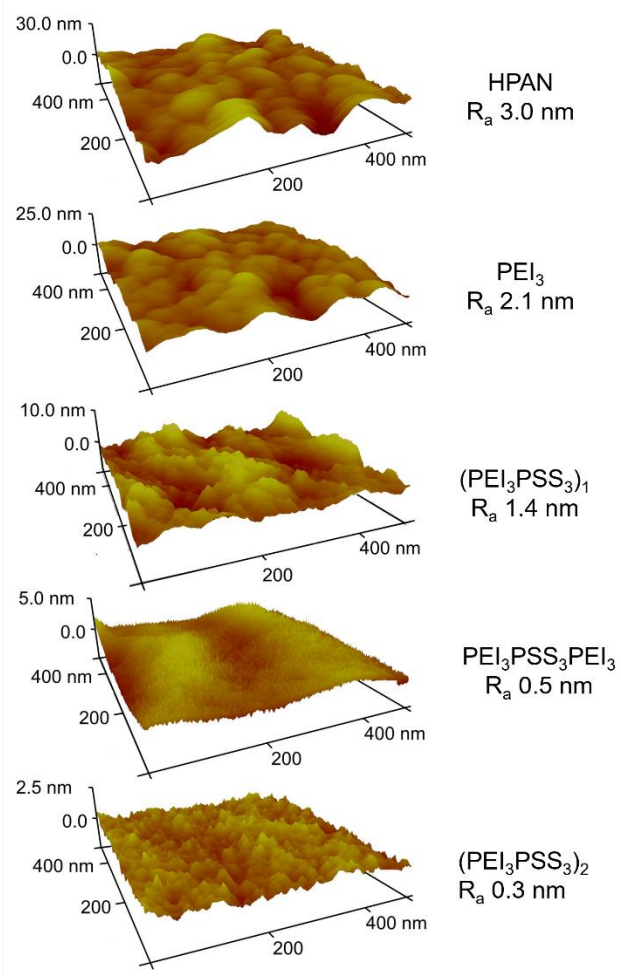

Figure S4.13 The 3D morphology of the $(PEI_nPSS_n)_x$ membrane surface with different bilayer numbers revealed by AFM (500 nm × 500 nm).

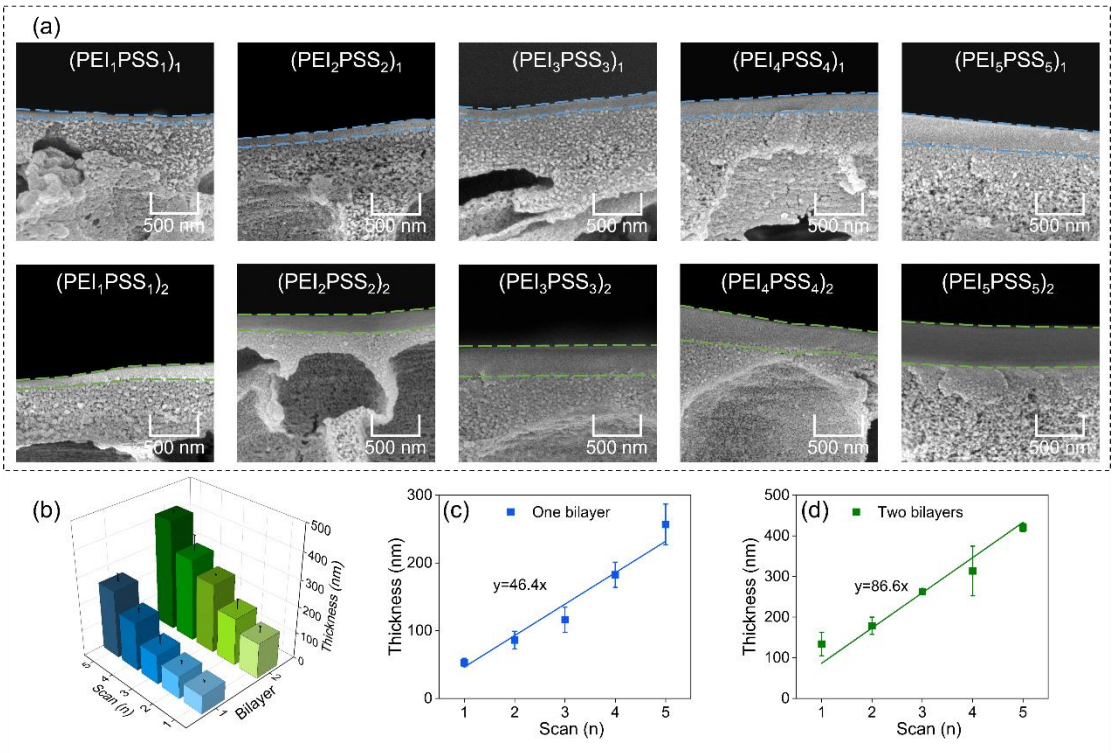

Figure S4.14 (a) Cross-section SEM images of the (PEI_1PSS_1), $(PEI_2PSS_2)_1$, $(PEI_3PSS4)_1$, $(PEI_4PSS_4)_1$, $(PEI_5PSS_5)_1$, $(PEI_1PSS_1)_2$, $(PEI_2PSS_2)_2$, $(PEI_3PSS4)_2$, $(PEI_4PSS_4)_2$ and $(PEI_5PSS_5)_2$ membranes, respectively; (b) the thickness of PEM membranes as a function of the scan number and bilayer number; (c) the thickness of one-bilayer membranes as a function of the scan number; (d) the thickness of two-bilayer membranes as a function of the scan number.

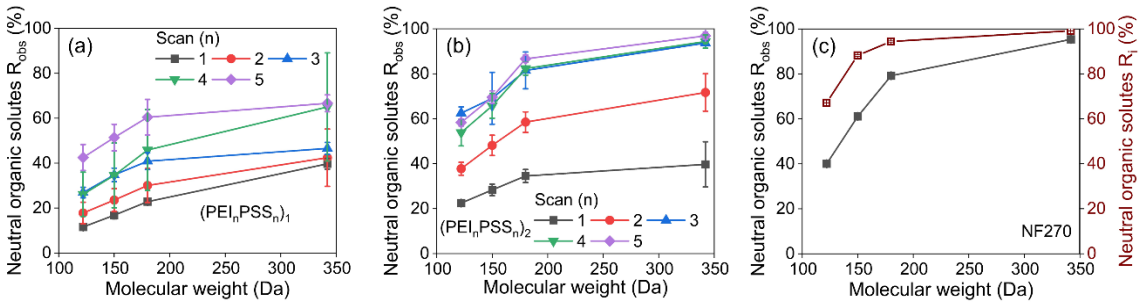

Figure S4.15 Observed rejection (R_{obs}) of neutral organic solutes of (a) $(PEI_nPSS_n)_1$ membranes, (b) $(PEI_nPSS_n)_2$ membranes, and (c) observed rejection (R_{obs}) and intrinsic rejection (R_i) of neutral organic solutes of the NF270 membrane. The solutes are erythritol, xylose, glucose, and sucrose. The data points were obtained from at least three measurements.

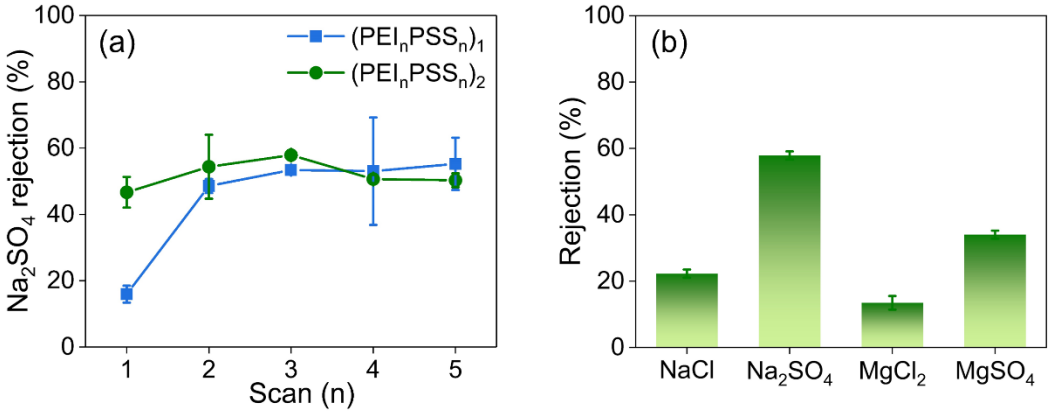

Figure S4.16 (a) Na_2SO_4 rejection of the $(PEI_nPSS_n)_x$ membranes with different bilayer numbers and scans; (b) single salt rejection of $(PEI_3PSS_3)_2$ membranes.

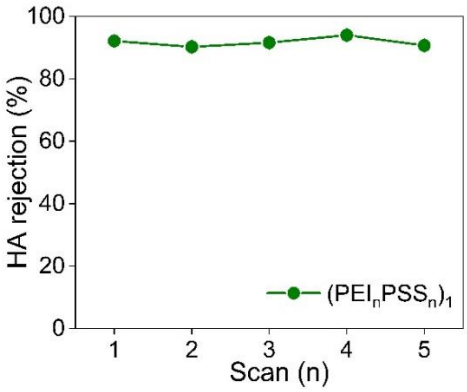

Figure S4.17 Humic acid (HA) rejection of $(PEI_nPSS_n)_1$ membranes with different scans. The HA concentration in the feed solution was 25 mg L^{-1}. The HA concentrations of the feed and permeate solutions were determined at corresponding absorption wavelengths of 254 nm using UV–vis spectroscopy (Biochrom Libra S35).

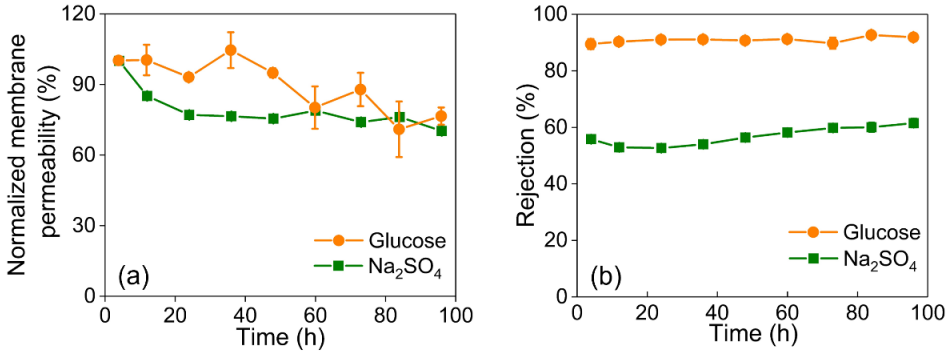

Figure S4.18 (a) Normalized membrane permeability and (b) glucose & Na_2SO_4 rejection of $(PEI_3PSS_3)_2$ membrane over 96 h of filtration experiments. The concentrations of feed glucose solution and Na_2SO_4 solution were 50 mg TOC L^{-1} and 100 mg L^{-1}, respectively. All the experiments were operated at an operating pressure of 5 bar in the crossflow filtration set-up. The permeate was collected every 12 h to measure the rejection and permeability.

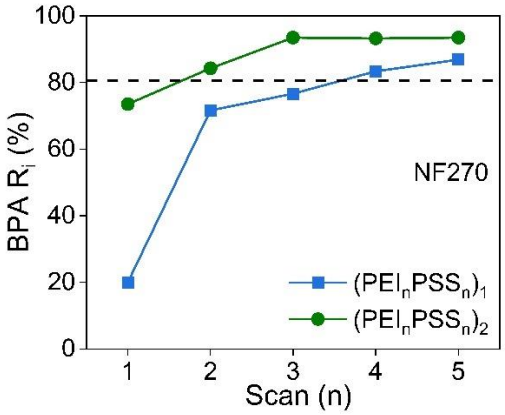

Figure S4.19 Intrinsic rejection of BPA (BPA R_i) of the $(PEI_nPSS_n)_x$ membranes with different bilayer numbers and scans. The dashed line (at 80.5% rejection) was BPA R_i of the NF270 membranes.

Chapter 5. Drying Effects on Structure and Performance of Polyelectrolyte Multilayer Membranes: Insights into Differential Responses of the Polyelectrolyte Multilayer Compaction and Substrate

Abstract

Polyelectrolyte multilayer (PEM) membranes, renowned for their tunable chemistry and versatile structure, hold significant promise for tailored nanofiltration (NF) applications. However, like most filtration membranes, PEM membranes are susceptible to structural and performance degradations upon drying. Current research lacks clarity regarding the time-dependent structural deformations induced by drying in both the PEM and the substrate, and their interplay in governing permeability and selectivity. This study systematically investigates the drying effects on PEM membranes fabricated via layer-by-layer aerosol-assisted printing of poly(allylamine hydrochloride) (PAH) and poly(sodium 4-styrenesulfonate) (PSS) on a polyacrylonitrile (PAN) substrate. We identified three sequential drying stages: (1) PEM compaction (0-2 h), (2) PAN substrate deformation (2-4 h), and (3) PEM tearing by interfacial stress (4-24 h). Furthermore, the substrate deformation drives permeability loss, and the compaction of the PEM selective layer controls selectivity. The distinction was largely due to the different elastic moduli and pore architectures of the PEM and PAN substrate. We also revealed that the incorporation of glycerol, a pore preservative, into either the PEM or the substrate, can largely maintain water permeability and solute rejection of the membranes upon drying. This is likely due to the diffusion/convective mass transfer of glycerol in between the two components. Our study provides valuable mechanistic insights into the differential responses of the PEM and substrate upon drying as well as the effective prevention strategies, which collectively advance the filtration applications of the PEM membranes.

5.1 Introduction

Polyelectrolyte multilayer (PEM) membranes, formed through the layer-by-layer (LbL) assembly of polyanions and polycations via electrostatic interactions, have become promising NF membranes. PEM NF membranes have a typical pore size in the range of 0.4-2 nm (DuChanois et al., 2019; Gan et al., 2025; Sigurdardottir et al., 2020; Wang et al., 2021) which can be precisely tailored by adjusting polyelectrolyte pairing, bilayer number, and assembly conditions. The conventional method for PEM fabrication is dip coating, which is easy to operate but time-consuming, due to the low diffusion speed of aqueous polyelectrolytes, and is material-consuming, due to the demand for a large amount of polyelectrolyte solutions. The spray-assisted LbL method is an attractive alternative technique for the fabrication of PEM with tunable properties and composition (Gan et al., 2025). The spraying technique has advantageous characteristics of low material consumption, easy control, and scalability. The droplets, produced by atomizing the polyelectrolyte solution, can be spread evenly over the substrate. After deposition, a certain period is required to allow the solvent to evaporate, enabling PEs to assemble into a dense, selective film.

Unlike dip coating, by which PEM forms entirely in an aqueous environment, spray-based membrane printing involves rapid droplet deposition and solvent evaporation both during and after deposition. This drying process is not merely a post-treatment step but an integral part of the assembly itself. As droplets impinge on the substrate surface, they spread and evaporate. Continued solvent evaporation promotes the entanglement of polymer chains, facilitating the formation of a stable PEM. Wang et al. (2011) verified that intermediate drying in between polyelectrolyte depositions resulted in more coherent films. However, excessive water evaporation during the drying process can lead to compaction of the PEM (Déjugnat et al., 2007; Lösche et al., 1998; Ma and Sun, 2009; V Klitzing, 2006). Take PAH and PSS multilayer as an example, under fully

hydrated conditions (100% relative humidity (RH)), water can constitute more than 40% of the film's volume (Déjugnat et al., 2007; Lösche et al., 1998). Upon drying the polyelectrolytic interface in the laboratory air, the PAH/PSS multilayer shrinks due to the evaporation of water from the multilayer structure, and this compaction occurs without significant polymer rearrangement (Lösche et al., 1998; V Klitzing, 2006). Déjugnat et al. (2007) used full-field transmission X-ray microscopy to prove a densification of the PEM upon heating, accompanied by significant dehydration, without loss of polymer material. For a PAH and PAA multilayer, as the RH drops below 90%, the structure does not collapse immediately because bound water is retained within the PEM's internal structure, and the polymer chains cannot easily rearrange or turn into a collapsed state due to strong electrostatic crosslinks and reduced chain flexibility (Mohammed et al., 2020; Secrist and Nolte, 2011). Notably, this compaction is largely reversible, as the PEM can re-swell almost completely when exposed to a fully hydrated condition (Lösche et al., 1998; Wong et al., 2004).

Despite early studies on PEM drying, the coupled time-dependent responses of the PEM and substrate remain poorly understood. In particular, the way their structural changes evolve simultaneously and affect each other during drying presents a significant knowledge gap. A PEM NF membrane typically consists of a porous ultrafiltration (UF) membrane as the supporting substrate and a selective PEM as the top. Common substrates include PAN, polysulfone (PSF), and polyethersulfone (PES) membranes due to their highly hydrophilic properties that can enhance water permeability and fouling resistance (Zhao and Wang, 2017). However, these UF substrates are commonly susceptible to pore collapse during drying or thermal treatment (Liu et al., 2019; Zverina et al., 2020). This phenomenon is primarily driven by capillary forces generated during the water evaporation. Specifically, the water within macrovoids induces surface tension, and as

the vapor attempts to evacuate the pores, capillary forces act inwardly on the pore walls, leading to shrinkage. While the membrane material inherently resists deformation, pore collapse occurs when the capillary force exceeds the modulus of the substrate material and thus leads to irreversible structure change. Therefore, during drying, both the PEM and the supporting substrate undergo structural changes that significantly affect the overall filtration performance of the PEM membrane. While the changes in the PEM are largely reversible, the alterations in the substrate are irreversible. However, the kinetics of structural evolution during drying, including the rate of water loss and time-dependent compaction, remain poorly quantified. Therefore, precise control over the reversible content of both the PEM and the substrate is essential to regulate their coupled yet distinct responses (PEM compaction and substrate deformation), which collectively determine the structural integrity and filtration performance of the final membrane.

In this study, we aim to investigate the distinct structural responses of the PEM and substrate during drying and their collective impact on filtration performance. We used an AAP system consisting of a commercial 3D printer with a Collison nebulizer to fabricate PEM membranes with PAH as the polycation and PSS as the polyanion. Glycerol, being the pore preservative (Beerlage, 1994; Macdonald and Pan, 1974; Zeng et al., 2022), was selectively incorporated into: (1) substrate only, (2) PEM only, and (3) both substrate and PEM. Under a controlled drying condition (constant ambient RH of 60%), we measured the moisture content changes of the composite membranes and hydraulic resistance contributions from the PEM and substrate over time. We also evaluated the water permeability and selectivity of the membranes dried at different durations. Based on all the data, we were able to identify the distinct phases of the changes of the composite membranes. Our study thus presents mechanistic insights into the coupled yet distinct responses of the PEM and substrate during drying, and how these responses collectively influence the structural integrity and

filtration performance of the final membrane. Understanding this distinction is crucial for the prevention of pore collapse caused during the drying process and thus advancing membrane storage and filtration applications.

5.2 Experimental

5.2.1 Materials and Chemicals

PAN UF membranes with a nominal average MWCO of 300 kDa were used as substrates (Sterlitech). PAH with a MW of 15 kDa (Aladdin) and PSS with a MW of 1000 kDa (Sigma-Aldrich) were used as the polycation and polyanion, respectively. NaOH was purchased from Duksan. PEG with different molecular weights (200, 400, 1000, 1500, 2000, and 6000 Da) was purchased from Sigma-Aldrich. Glycerol (99% in water) was also obtained from Sigma-Aldrich. Pure water (Milli-Q plus system, Millipore) was used for preparing solutions and testing membrane water permeability.

5.2.2 Polyelectrolyte Multilayer Membrane Fabrication

PEM membranes were assembled by AAP (Figure S3.2), as we previously reported (Gan et al., 2025). The equipment consists of an aerosol spray system (Collison nebulizer), a pressure supply system, and a 3D printer (3DLDL, Six Point Zero Inc.). The Collison nebulizer, as the aerosol generation instrument, generates micrometer-sized droplets at an applied pressure of 1 bar using compressed air as the carrier gas. A stainless-steel tube as the nebulizer outlet (14 mm diameter) was aligned perpendicular to the substrate surface, positioned 15 mm above the substrate. The 3D printer was used to control the movement of the nozzle.

Prior to LbL assembly coating, the PAN substrate was immersed in ethanol and then rinsed with pure water to remove preservatives. Subsequently, the treated PAN substrates were hydrolyzed in a 2.0 M NaOH solution at ambient temperature for 2 hours. The hydrolyzed PAN (HPAN)

membranes were rinsed with pure water to remove excessive NaOH and then stored in pure water for further PEM membrane preparation. The polyelectrolyte solutions (PAH 8.0 g L^{-1}, PSS 16.0 g L^{-1}) were added in two separate Collison nebulizers and printed on the substrates by AAP in a layer-by-layer fashion. The HPAN substrate was first sprayed with PAH aerosol, after which the PSS aerosol was introduced onto the PAH-coated membrane. The first PE bilayer (i.e., one PAH/PSS bilayer) was produced with one layer of PAH and one layer of PSS, and the PEM membranes coated with two bilayers (denoted as HPAN-PEM) were prepared by repeating the above coating process.

5.2.3 Glycerol-Polyelectrolyte Multilayer Membrane Preparation

In this experiment, the HPAN membrane was immersed in glycerol (15% weight) for at least 24 hours, allowing the pores of the HPAN substrate to be fully filled with glycerol. Before polyelectrolyte deposition, the HPAN membrane was rinsed with pure water to remove the residual glycerol solution on the surface. The glycerol-saturated HPAN substrate was denoted as GHPAN. Two PAH/PSS bilayers were printed on the GPAN substrate, and the resulting membrane was denoted as GHPAN-PEM. Glycerol was mixed into the PAH solution (8.0 g L^{-1}) and the PSS solution (16.0 g L^{-1}), so that each polyelectrolyte solution contained 15 wt.% glycerol by weight of the total solution. The polyelectrolyte solutions with added glycerol were utilized to fabricate two-bilayer PEMs on the HPAN and GHPAN substrates, denoted as HPAN-GPEM and GHPAN-GPEM, respectively. Figure S5.1 provides a schematic comparison of substrates (HPAN and GHPAN) and PEM membranes (HPAN-PEM, GHPAN-PEM, HPAN-GPEM, and GHPAN-GPEM).

5.2.4 Controlled Drying Experiment

To investigate the effects of humidity and drying duration on membrane structure, a series of membranes, including substrates (HPAN and GHPAN) and PEM membranes (HPAN-PEM, GHPAN-PEM, HPAN-GPEM, and GHPAN-GPEM), were subjected to controlled drying tests. The membranes were placed in a humidity-controlled chamber (Aritte GP_5-30L), maintained at 60% RH and a constant temperature of 23 °C. After designated drying periods (0-24 hours), each membrane was either immediately tested using a crossflow filtration setup or subjected to further characterization to evaluate structural and functional changes resulting from the drying.

5.2.5 Water Evaporation Experiment

The evaporated water weight of the membrane samples was measured using a 4-digit analytical balance (Mettler Toledo). The moisture content (%) was calculated based on the following equation.

$$Moisture\ content\ (\%) = \frac{M_t - M_d}{M_0 - M_d} \times 100 \quad (5.1)$$

where M_t is the weighed mass after drying time (t), M_0 is the initial weighed mass, and M_d is the weighed mass after controlled drying at 23 °C and 60% RH for 8 hours, followed by drying at 180 °C for 2 hours.

5.2.6 Membrane Characterization

ATR-FTIR (PerkinElmer) spectroscopy was used to investigate the surface chemistry evolution during the 24-hour drying process, with a resolution of 4 cm^{-1} and a wavenumber range from 4000 to 400 cm^{-1}. Surface and cross-sectional images of the PEM membranes were observed using a FESEM (MAIA3, Tescan) after sputter coating the samples with gold (MCM-200 ion sputter coater, Micro Optics).

5.2.7 Membrane Filtration Performance

Membrane filtration performance was evaluated using a crossflow filtration set-up. Each membrane coupon, with an effective area of 8 cm^2, was tested at 5 bar and a crossflow velocity of 26.7 cm s^{-1}. The membrane was compacted by pure water under a pressure of 5 bar for 2 hours before the permeability/rejection experiment. The weight of the permeate was measured using an automatic electronic balance (Ohaus, SPX2201) at a 60 s interval for 30 min. The PWP (J_w, $L \cdot m^{-2} \cdot h^{-1} \cdot bar^{-1}$) was calculated by the Eq. (5.2):

$$J_w = \frac{V}{\Delta P \times A \times \Delta t} \tag{5.2}$$

where ΔP (bar) is the trans-membrane pressure, A is the effective filtration membrane area (m^2), and V is the volume (L) of permeate collected over an operating time (Δt (h)).

In addition, the PWP can be alternatively displayed as a function of the hydraulic resistance R_h (m^{-1}) (Junker et al., 2023; Reurink et al., 2019):

$$R_h = \frac{\Delta P}{\mu J_w} \tag{5.3}$$

where μ is the viscosity (Pa s) of water.

Based on the above definition, the ratio (R_{PEM}/R_{HPAN}) of PEM hydraulic resistance (R_{PEM}) and HPAN hydraulic resistance (R_{HPAN}) can be defined as:

$$R_{PEM}/R_{HPAN} = \frac{J_{wHPAN}}{J_{wPEM}} \tag{5.4}$$

The MWCO values of the membranes were determined by fitting the rejection curve of PEG with different molecular weights (200, 400, 1000, 1500, 2000, and 6000 Da). The concentrations of the solutes were measured using a TOC analyzer (Shimadzu, Japan). The feed solution of each sugar was 100 mg TOC L^{-1}. The average pore sizes of the PEM membranes with different scans and bilayer numbers were estimated by the steric hindrance pore model (Text S4.5) using rejection

of PEG with different molecular weights mentioned above (Boo et al., 2018b; DuChanois et al., 2019). The solutes and salt rejection, R (%), was calculated using Eq. (5.5):

$$R = \left(1 - \frac{C_p}{C_f}\right) \times 100\% \tag{5.5}$$

where C_p is the permeate concentration and C_f is the concentration of the feed solution. The data is an average value from measuring at least three samples of each kind of membrane.

5.3 Results and Discussion

5.3.1 Water Evaporation Process

During drying, at least two main processes occur simultaneously: water evaporation at the material surface and transfer of internal moisture to the surface of the membrane (Dinçer and Zamfirescu, 2016). Moisture content reflects the drying process of a porous material, and its variation over time provides useful information about the water transport mechanisms. The moisture within a membrane comprises three distinct types: free water, capillary water, and bound water (Huang et al., 2022). Free water typically exists in deposited droplets on the surface and within the open pores of the substrate and evaporates readily during drying. Capillary water occupies the small cavities or pores in the membrane's porous network, held in place by surface tension within the pores. In addition, bound water is tightly associated with the polymer chains and counter ions via hydrogen bonding or electrostatic interactions and requires elevated temperatures to be fully removed.

The moisture content of various membranes decreased as time increased (Figure 5.1). The change of moisture content in the drying process can be divided into three phases. In the first phase, from 0 to ca. 1.5 hours, the moisture content decreased linearly over time (Figure 5.1a-f, $R^2 = 0.98$-

0.99). Free water evaporation weight can be estimated by the mass transfer-based evaporation model (Dinçer and Zamfirescu, 2016):

$$m = k \times A \times (p_{SAT} \times T - p_{SAT} \times RH) \times t$$

where m is the mass of evaporated water, k is the mass transfer coefficient, A is the evaporation area, p_{SAT} is the saturation vapor pressure at the temperature T, RH is the relative humidity, and t is the drying time.

Under identical temperature and humidity conditions, the constant vapor pressure gradient sustains a steady evaporation rate, and the free water content decreases linearly as drying progresses. The moisture of HPAN-PEM membranes decreased at a rate of 0.19 g h^{-1} (Figure 5.1c), which was higher than that of the HPAN substrates (0.17 g h^{-1}) (Figure 5.1a). We suspect that the sprayed polyelectrolyte droplets create a vastly increased number of liquid-air interfaces compared to a smooth film, thereby accelerating water evaporation. PEM membranes containing glycerol showed a moisture decrease rate of 0.15-0.16 g h^{-1} (Figure 5.1d-f), lower than that of PEM membranes prepared without glycerol (0.19 g h^{-1}) (Figure 5.1c). This suggests that pre-filling glycerol into either the substrate or PEM effectively slows down water evaporation, due to glycerol's hygroscopic nature, which enables hydrogen bond formation with water, thereby retaining moisture within the membrane structure. The water evaporated in the first phase is primarily denoted as free water, also known as void water, which is not strongly bound to the solid matrix (Ho et al., 2015). In this period, moisture movement within the membrane is rapid enough to keep a saturated condition at the surface (Dinçer and Zamfirescu, 2016). This easily removable moisture sustains a constant drying rate as it continuously migrates to the surface and evaporates. Koehler et al. (2014) have suggested that the void water does not contribute to volume changes,

which means the membrane structure remains almost unchanged upon the evaporation of void water.

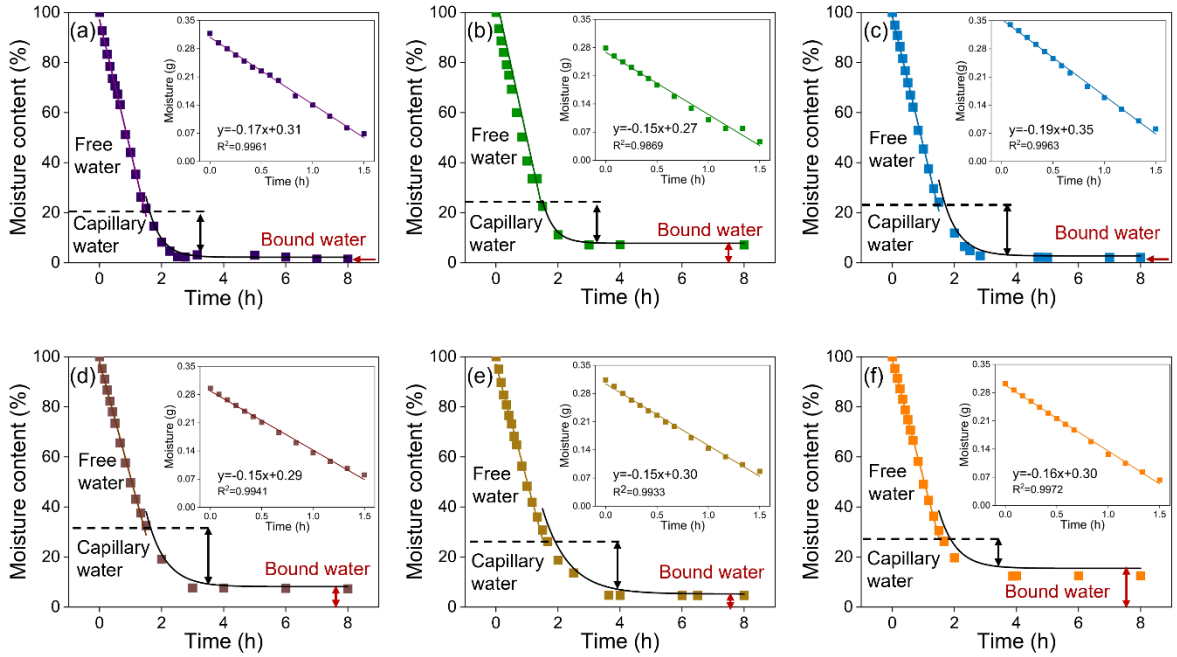

Figure 5.1 Drying effect on moisture content of the substrate and PEM membranes at 60% RH and ambient temperature: (a) HPAN substrate, (b) glycerol pre-filled HPAN substrate (GHPAN), (c) PEM membrane fabricated on the HPAN substrate (HPAN-PEM), and (d) PEM membranes fabricated on glycerol pre-filled HPAN substrates (GHPAN-PEM), (e) PEM membranes with exclusive glycerol incorporation in the PEM (HPAN-GPEM), (f) PEM membranes with glycerol incorporation in both the PEM and the HPAN substrate (GHPAN-GPEM), and the inset figures are magnified view of moisture decrease within the first 0-1.5 hours.

A diffusion process of the moisture within the water evaporation is followed by a convective mass transfer at the solid surface. Gradually, moisture cannot be transported to the drying surface

as a result of the capillary action of pressure gradients in the gas phase (Dinçer and Zamfirescu, 2016; Kusoglu and Weber, 2017). In the second drying phase (ca. 1.5-3 hours), once the easily removable free water largely evaporated, the overall rate of moisture loss slowed markedly, and the decline rate of moisture content decelerated. During this stage, evaporation is dominated by capillary water trapped within the membrane's narrow pores and cavities, where it is held in place by surface tension. The pronounced curvature of the liquid-air menisci in these small pores increases the capillary pressure (Young-Laplace equation) (Widom, 2004) and lowers the equilibrium vapor pressure at the interface (Kelvin effect) (Israelachvili, 2010), both of which act to retard evaporation relative to the first phase.

In the second phase, the membrane's porous structure becomes highly vulnerable to collapse. The water in finger-like pores and cavities induced a surface tension force. As water vapor begins to evaporate from these macropores, capillary forces act on the pore walls, leading to pore shrinkage. Simultaneously, the membrane pore itself has a resistance to this deformation. When the capillary force exceeds the elastic modulus of the membrane material, the macropores collapse. The capillary forces (F_c) can be represented by the following equation.

$$F_C = \frac{2\gamma}{r_p} cos\theta \times A \tag{5.6}$$

where γ is the liquid surface tension of the solvent (N m^{-1}), r_p is the pore radius (m), θ is the water contact angle (°), and A is the cross-sectional area of the pore. The resistance of the polymer to deformation (F_r) can be represented by the following equation.

$$F_r = 0.37E \times A \tag{5.7}$$

where E is the elastic modulus of polymer (N m^{-2}), and A is the cross-sectional area of a pore.

The capillary force can reach a significant value due to the small pore radius of NF membranes, as indicated by Eq. (5.6). In HPAN-PEM membranes, the structure is composed of a PEM selective

layer deposited on a porous PAN substrate. These two components possess distinct mechanical properties, resulting in different resistances to deformation, as described in Eq. (5.7). The elastic modulus of the PAN substrate was reported to be approximately 22 MPa (Tüfekci et al., 2020). Assuming the PAN substrate behaved as a homogeneous medium, its average pore size can be approximated as 16.4 nm (calculated based on its MWCO). The water surface tension was measured to be 72 mN m^{-1}. During the drying process, as water evaporates from the pores, the contact angle θ tends toward 0°, and cosθ approaches 1. When this capillary pressure exceeded a critical fraction of the elastic modulus, namely when $2\gamma/r_p > 0.37E$, mechanical collapse of the pore structure can occur. Given the parameters, the calculated capillary pressure ($2\gamma/r_p = 8.8$ MPa) exceeded the threshold required to overcome the mechanical resistance (0.37E = 8.1 MPa) of the PAN substrate, indicating that water evaporation can indeed induce structural deformation or even collapse within the substrate. The elastic modulus of the PAH/PSS multilayer was reported to be approximately 2.7 GPa (Ba et al., 2010), which was about two orders of magnitude higher than that of the PAN substrate. Owing to this high modulus, the PEM selective layer is expected to exhibit great resistance to deformation under capillary stresses. However, it is important to note that the pore size of the PEM layer is substantially smaller than that of the PAN substrate. Since capillary pressure is inversely proportional to pore radius, the smaller pores in the PEM layer may generate even higher capillary forces during water evaporation. The balance between this increased capillary pressure and the higher mechanical resistance of the PEM layer introduces additional complexity in predicting its deformation behavior. This aspect will be further examined in the subsequent section, following the determination of the PEM layer's pore size.

In the third phase (ca. 3-8 hours), water evaporation became virtually undetectable under conditions of 23 °C and 60% RH. The membrane was then heated to 180 °C to ensure complete

removal of residual moisture. This residual moisture represents bound water, with the content measuring 1.5% in the HPAN substrate (Figure 5.1a) and 7.1% in the GHPAN substrate (Figure 5.1b), confirming glycerol's effectiveness in retaining bound water. The residual moisture content was 2.2% in the HPAN-PEM membrane, which was higher than that in the HPAN substrate, because the PEM contained charged groups (e.g., $–SO_3^-$ and $–NH_3^+$) that form hydrogen bonding with water molecules and thus retained more water (Batys et al., 2018; Zhang et al., 2016). The residual moisture content was 7.3% in the GHPAN-PEM membrane (Figure 5.1d) and 4.6% in the HPAN-GPEM membrane (Figure 5.1e), both higher than that of the HPAN-PEM membrane, showing that the addition of glycerol enhanced bound water retention. When glycerol was incorporated into both the PEM and the HPAN substrate, the residual moisture content reached the highest, 12.5% (Figure 5.1f). This result suggests a synergistic effect between the glycerol-incorporated substrate and the glycerol-containing PEM. Consequently, the GHPAN-GPEM membrane retained a high fraction of bound water, which facilitated preserving flexibility and preventing structural collapse during drying.

5.3.2 Characterization of Dried Polyelectrolyte Multilayer Membranes

The drying of the membranes was further monitored by ATR-FTIR. The broad absorption peak around 3200-3600 cm^{-1}, corresponding to the O-H stretching vibration of water molecules, was recorded over time for comparison. For all the membranes, whether with or without glycerol prefilling, this characteristic peak of water molecules gradually decreased as drying time increased, indicating a reduction in water content due to evaporation (Figure S5.2). As mentioned above, after 24 hours of drying, the moisture content in the membranes became almost negligible, while the prefilled glycerol remained in the dried membranes. This phenomenon was further confirmed by

the FTIR spectra (Figure 5.2a). The broad absorption peak around 3200-3400 cm^{-1}, corresponding to the O-H stretching vibration of glycerol and/or retained water, was more pronounced in the spectra of the GHPAN substrates compared to HPAN substrates (Figure 5.2a). The presence of glycerol resulted in a prominent peak around 3200-3400 cm^{-1}, but for the HPAN-GPEM membranes, this peak was not as distinct because the amount of glycerol in the PEM was much lower compared to the prefilled glycerol in the substrate (Figure 5.2a).

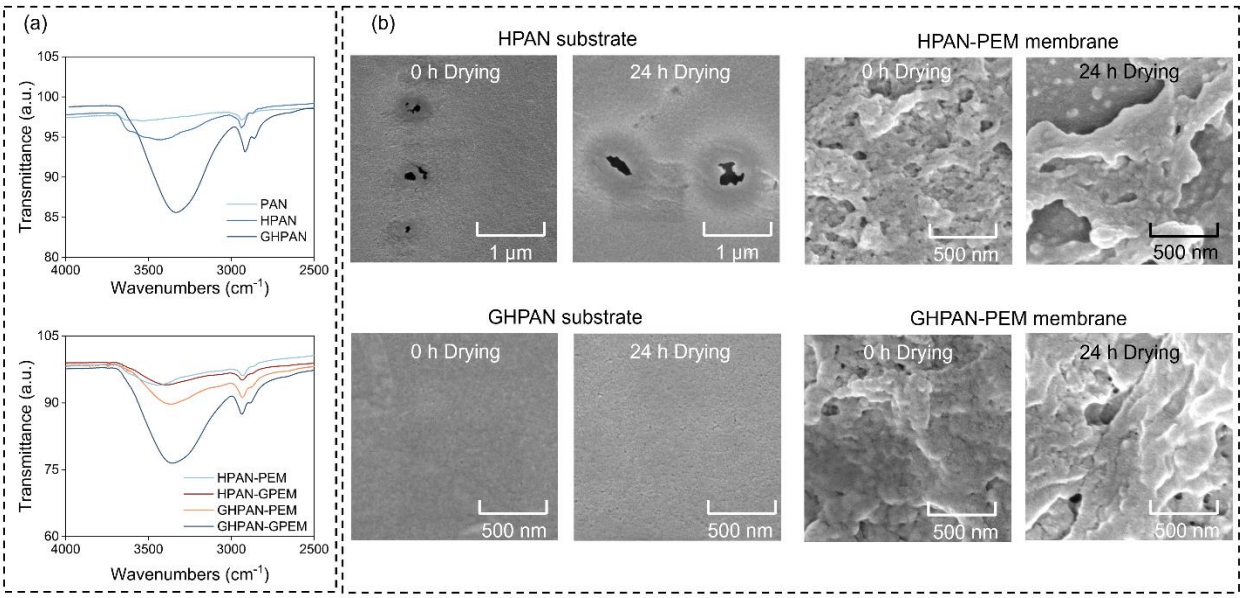

Figure 5.2 FTIR spectra for the substrate and PEM membranes after 24-hour drying: (a) Comparison of the PAN, HPAN, and GHPAN substrates, (b) Comparison of the final PEM membranes: HPAN-PEM, HPAN-GPEM, GHPAN-PEM, and GHPAN-GPEM. (c) Surface SEM images of the substrates and PEM membranes after 0 hours and 24 hours drying, including HPAN substrate, HPAN-PEM membrane, (GHPAN) substrate, and GHPAN-PEM membrane.

The membrane morphology resulting from the drying process was investigated using FESEM. The top-view FESEM images showed the morphology of the pristine HPAN substrate, HPAN-

PEM membranes, and glycerol-added PEM membranes. Drying had a discernible influence on both the pore diameter and smoothness of the HPAN substrate surface. The sizable pores were observed on the HPAN substrate with a pore diameter range of 50-200 nm (Figure 5.2b). After 24 hours of drying, the obvious pores became larger, ranging from 150 to 400 nm (Figure 5.2b). Compared to the substrate without drying, the membrane surface was smoother after 24 hours of drying. When the HPAN pores were impregnated with 15 wt.% glycerol, no discernible pores were shown on the surface both before drying and after 24 hours of drying (Figure 5.2b). The surface morphology of the HPAN-PEM membrane remained almost unchanged before and after drying because the PEM contained bound water, which helped maintain the shape and structural integrity of PEM.

5.3.3 Drying Effect on Membrane Filtration Performance

5.3.3.1 Drying Effect on the Substrate

The influence of the drying time on the water permeability is shown in Figure 5.3a. As the drying time increased, the water permeability of the HPAN substrate exhibited a decreasing trend, which can be segmented into four stages. Initially, the HPAN substrate had a water permeability of 95.0 ± 1.7 L m^{-2} h^{-1} bar^{-1}. During the first stage (ca. 0-2 h drying), the permeability decreased at a rate of -6.7 L m^{-2} h^{-2} bar^{-1} per hour. In the second stage (ca. 2-4 h drying), the water permeability dramatically dropped from 81.7 to 15.2 L m^{-2} h^{-1} bar^{-1}, indicating rapid structural changes in the HPAN substrate. In the third stage, from 4 to 8 hours of the drying process, the water permeability decreased at a slower rate of -1.5 L m^{-2} h^{-2} bar^{-1} per hour. Finally, in the fourth stage, the water permeability reached a relatively stable value of around 9.0 L m^{-2} h^{-1} bar^{-1}, indicating a consistent level of permeability under prolonged drying durations.

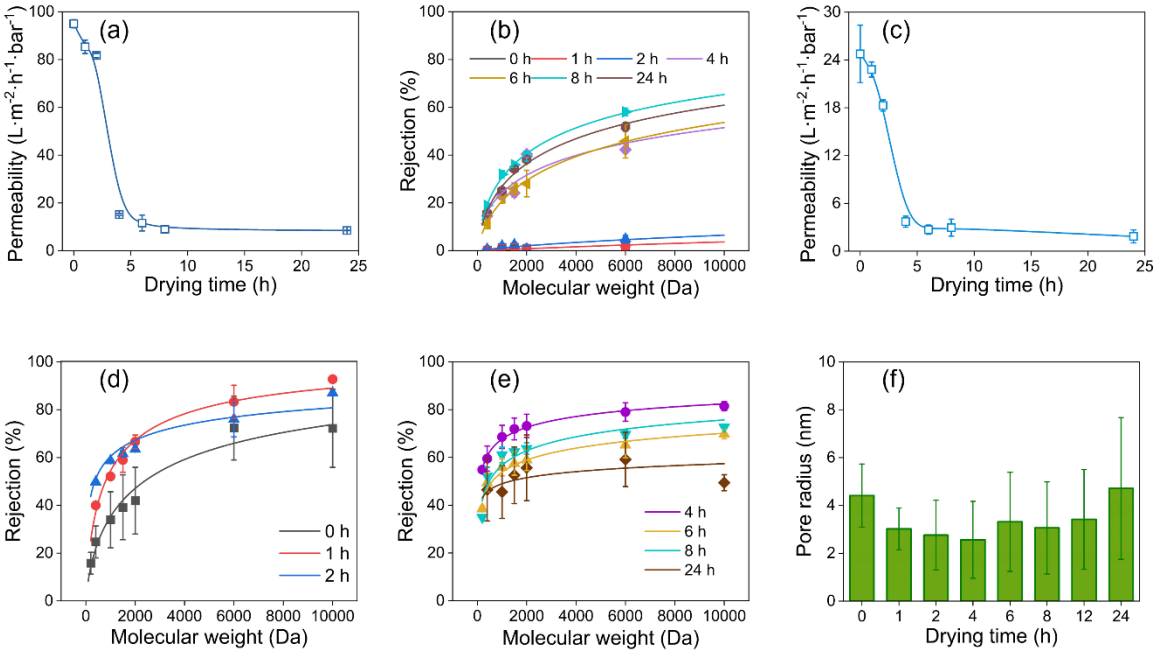

Figure 5.3 Filtration performance of the HPAN substrates and HPAN-PEM membranes after different drying durations at 60% RH: (a) pure water permeability of HPAN substrates, (b) PEG rejection curve of HPAN substrates, (c) pure water permeability of HPAN-PEM membranes, (d) PEG rejection curve of HPAN-PEM membranes after drying of 0, 1 and 2 hours, (e) PEG rejection curve of HPAN-PEM membranes after drying of 4, 6, 8 and 24 hours, (f) estimated mean pore radius of HPAN-PEM membranes, and (g) hydration resistance ratio of PEM and HPAN substrates.

Moreover, the rejections of neutral organic compounds of various molecular weights were evaluated (Figure 5.3b). During the initial stage, the PEG rejection curve of the HPAN substrate dried for 1 hour was similar to that of the HPAN substrate dried for 2 hours. While the free water evaporation induced little adjustments in the membrane structure, resulting in a decline in water permeability, the overall retention capacity of the HPAN remained unchanged during the initial

stage. In the second stage, from 2 to 4 hours of the drying process, the rejection of PEG with a molecular weight of 6000 Da (PEG6000) increased significantly from 4.8% to 42.3% (Figure 5.3a and S5.5). The sharp rise in PEG6000 rejection, coupled with the marked decrease in water permeability, indicates substantial structural changes within the HPAN substrate. These changes are largely attributed to the evaporation of the capillary water, which drives pore shrinkage or even collapse, as discussed in the previous section. In the third stage, the PEG6000 rejection increased from 42.3% to 58.1% (Figure S5.3) at a slower rate compared to that in the second stage, suggesting that structural changes in the HPAN substrate were still occurring but had begun to slow down. This corresponds to a moisture content change that became undetectable by a four-digit balance, indicating that most free and capillary water had already evaporated, leaving primarily tightly bound water. In the fourth stage, after 24 hours of drying, the PEG6000 rejection of the HPAN substrate was 51.8% (Figure S5.3), likely due to minor structural relaxation or redistribution of bound water, as the residual moisture content approached equilibrium.

5.3.3.2 Drying Effect on Polyelectrolyte Multilayer Membrane

Following the LbL spray coating of PEM onto the HPAN substrate, the impact of the drying process on the filtration performance of the PEM membrane was evaluated by measuring water permeability, MWCO, and pore size. As the drying time increased from 0 to 4 hours, the water permeability exhibited a marked downward trend (Figure 5.3c). At 0 hours, the water permeability was 24.8 L m^{-2} h^{-1} bar^{-1}, and a slight decrease to 22.8 L m^{-2} h^{-1} bar^{-1} after 1 hour drying indicated a slight impact on the membrane structure. From 0 to 2 hours drying, the permeability decreased at a rate of -3.3 L m^{-2} h^{-2} bar^{-1} per hour. The PEM coating helps mitigate the rapid loss in water permeability observed in the HPAN substrate (Figure 5.3c) during the early stages of drying. As drying proceeded into the first two hours, free water escaped and capillary water in the PEM pores

evaporated (Figure 5.1c). Notably, from 2 to 4 hours of the drying process, the dramatic reduction of the water permeability from 18.3 to 3.7 L m^{-2} h^{-1} bar^{-1} implied that prolonged drying induces significant structural change. Corresponding to the HPAN drying process, the most rapid decline in water permeability occurred between 2 and 4 hours (Figure 5.3a). This sharp decrease in water permeability of the PEM membrane suggested that the HPAN substrate's drying behavior may play a pivotal role during this stage of the drying process. As drying progressed from 4 hours to 8 hours, the water permeability decreased at a slower rate of -0.2 L m^{-2} h^{-2} bar^{-1}. Finally, the PEM membranes eventually stabilized at a consistent permeability level after extended drying and exhibited a comparable trend similar to the HPAN substrate.

The selective separation capability of PEM membranes during the drying process was evaluated based on MWCO. The MWCO values were determined from the rejection curves as the molecular weight corresponding to a 90% rejection, and the intrinsic rejections were fitted by the steric hindrance pore model to obtain the pore size of the PEM membranes (Boo et al., 2018a; DuChanois et al., 2019). The PEG rejection curve for the PEM membrane without drying was lower than that observed after 1 hour, reflecting a larger MWCO exceeding 10 kDa (Figure 5.3d). After 1 hour of drying, the MWCO decreased to 6,376 Da (Figure 5.3d). Prior analyses indicated that the HPAN substrate's retention capability remained relatively stable during the first 2 hours, suggesting that the observed changes in the retention capability of the PEM membrane after 1 hour were predominantly due to transformations of the PEM itself. The PEG rejection curve of the PEM membrane dried for 2 hours was similar to that for 4 hours. As the drying time increased from 4 to 24 hours, the PEM exhibited a decrease in rejection of various PEGs (Figure 5.3e).

The PEM serving as the selective layer determined the primary rejection capability, consequently determining the pore radius. The pore sizes estimated from the test of each organic

solute were averaged to obtain the pore size for each membrane (Boo et al., 2018a; Dang et al., 2014). The average pore radius of the PEM membrane at 0 hours was 4.4 ± 1.3 nm and decreased to 3.0 ± 0.9 nm after 1 hour of drying (Figure 5.3f). As water evaporates, the PEM experiences enhanced fast compaction, leading to tighter interchain interactions and, consequently, a reduction in pore size. Although the pores become smaller, water permeability changes only slightly because the interconnected porosity remains intact, maintaining continuous pathways for water transport. This densification results in improved selective separation, as the smaller pores more effectively restrict the passage of larger solutes. Thus, the dehydration-induced structural evolution of the PEM layer plays a critical role in defining the membrane's filtration performance during the early stages of the drying process. After 2 hours of drying, the PEM membrane exhibited an average pore radius of 2.8 ± 1.5 nm (Figure 5.3f), accompanied by a water permeability of 18.3 L m^{-2} h^{-1} bar^{-1} (Figure 5.3c). After 4 hours of drying, the pore radius decreased to 2.6 ± 1.6 nm (Figure 5.3f), and the water permeability dramatically dropped to 3.7 L m^{-2} h^{-1} bar^{-1} (Figure 5.3c). The average pore radius remained relatively stable (only decreased the pore radius by ≤ 10%) during the period of 2 to 4 hours. This almost negligible variation in pore radius suggested that the structure of the PEM layer remained largely unaffected between 2 to 4 hours. The substantial decrease in water permeability during 2-4 drying cannot be attributed solely to the minor reduction in average pore radius. Instead, this trend aligned with a pronounced drop in the water permeability of the underlying HPAN substrate (Figure 5.3a), indicating that structural changes in the substrate also played a key role. It is likely that prolonged drying induced pore collapse or densification within the HPAN support layer, leading to a significant reduction in its porosity. This reduction in the HPAN substrate's transport properties, in turn, contributed to the drastic reduction in the overall water permeability of the PEM membranes.

As drying progressed from 4 hours to 24 hours, the average pore radius of the PEM membrane gradually increased from 2.6 ± 1.6 nm to 4.7 ± 3.0 nm (Figure 5.3f). This (unexpected) augmentation in pore size is attributed to the disparate contraction rates between the PEM and the HPAN substrate experienced during the drying process. Based on the pore size of 2.6 nm, and using Eq. (5.6) and (5.7), the calculated capillary pressure ($2\gamma/r_p$ = 0.5 GPa) was found to be lower than the threshold required to overcome the mechanical resistance (0.37E = 1.0 GPa) of the PAH/PSS PEM, as defined by its reported elastic modulus of 2.7 GPa (Ba et al., 2010). Therefore, the PEM is unlikely to continue to shrink. In contrast, the PAN substrate lacks sufficient mechanical strength to resist the capillary forces, resulting in pore collapse and structural deformation. This differential response is critical in understanding the overall mechanical stability of PEM membranes during drying. While the PEM layer may maintain its structural integrity, the underlying PAN substrate may undergo shrinkage, pore collapse, or other forms of deformation. This mismatch in mechanical behavior can further introduce interfacial stress between the layers, resulting in the development of fissures within the membrane, consequently facilitating the expansion of the mean pore radius.

To more clearly illustrate the relative contribution of PEM compaction and HPAN substrate collapse to PEM membrane filtration performance, the hydraulic resistance ratio of the standalone PEM and the bare HPAN substrate was calculated (Eq. 5.4) and shown in Figure 5.4. At 0 hours, the hydraulic resistance ratio was 3.1, reflecting that the PEM serving as the selective layer was the principal barrier to water transport. During the first 2 hours of drying, the hydraulic resistance ratio climbed to its peak, reaching 6.0 (Figure 5.4), indicating that evaporation of free water led to significant compaction of the PEM, thereby increasing water transport resistance. This was in accordance with a substantial decrease of the effective pore size from 4.4 ± 1.3 nm at 0 hours to

2.8 ± 1.5 nm after 2 hours drying. After 2 hours drying, the hydraulic resistance ratio gradually declined (Figure 5.4), indicating that substrate deformation began to play a more dominant role in contributing to the overall water transport resistance. Overall, the decline in water permeability became more pronounced initially, gradually slowed, and stabilized over the 24-hour drying process.

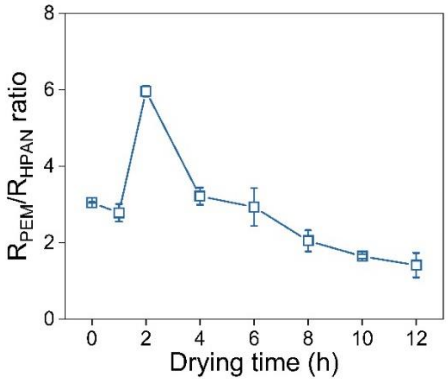

Figure 5.4 Hydraulic resistance ratio between PEM and HPAN substrate after different drying durations at 60% RH.

5.3.4 Glycerol's Effect on Preventing Pore Structure Shrinkage

Generally, glycerol was incorporated as an additive to prevent the substrate's pore structure from shrinking during the water evaporation process. The presence of glycerol solutions within the HPAN pores notably alleviated the impact of drying on the water permeability of the HPAN substrate (Figure 5.5a). After 1 hour of drying, the water permeability was 82.1 ± 3.9 L m^{-2} h^{-1} bar^{-1}, which decreased modestly to 72.6 ± 17.1 L m^{-2} h^{-1} bar^{-1} by 4 hours and further stabilized at 71.2 ± 5.9 L m^{-2} h^{-1} bar^{-1} after 24 hours. In contrast to the water-filled HPAN membrane, which displayed a notable decrease in water permeability during the drying process, the GHPAN substrate maintained a relatively stable water permeability over time. When HPAN substrates were

filled with glycerol solutions, the PEG rejection curves exhibited similarity regardless of drying duration (Figure 5.5a), indicating that glycerol effectively stabilizes the pore structure during the drying process.

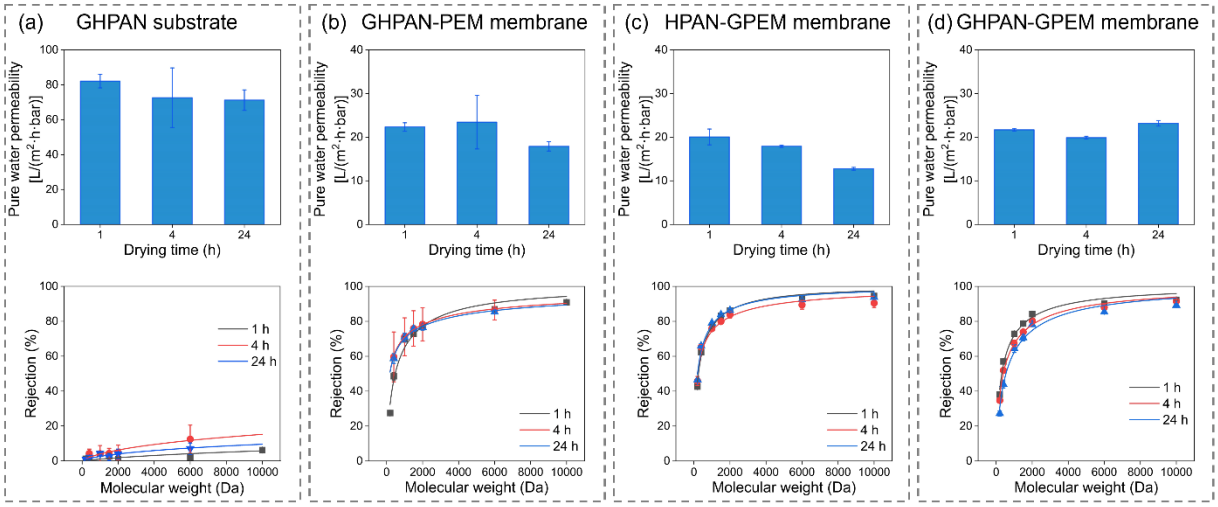

Figure 5.5 Pure water permeability, and PEG rejection curves of the PEM membranes after 1, 4, 24 hours of drying time at 60% RH: (a) glycerol pre-filled HPAN (GHPAN) substrate, (b) PEM membranes fabricated on glycerol pre-filled HPAN substrates (GHPAN-PEM), (c) PEM membranes with exclusive glycerol incorporation in the PEM (HPAN-GPEM), (d) PEM membranes with glycerol incorporation in both the PEM and the HPAN substrate (GHPAN-GPEM).

Following the LbL spray coating of the PEM onto the GHPAN substrate, the effect of drying time on water permeability was evaluated (Figure 5.5b). After 1 hour of drying, the water permeability was measured at 22.3 ± 1.0 L m^{-2} h^{-1} bar^{-1}, and it remained relatively stable at 23.4 ± 6.1 L m^{-2} h^{-1} bar^{-1} after 4 hours. Moreover, prolonged drying for 24 hours led to a slight decrease in water permeability because of the PEM compaction. On the contrary, the HPAN-PEM

membrane displayed a notable decrease in water permeability over time (Figure 5.3c). The PEG rejection curves for the GHPAN-PEM membranes remained similar after 1, 4, and 24 hours of drying (Figure 5.5b). Furthermore, the calculated average pore radius remained nearly identical (Figure S5.4). Glycerol from the GPAN substrate likely diffuses into the PEM films, preventing PEM compaction and helping to maintain a stable average pore radius. These results also indicate that glycerol effectively prevents the pore structure of the HPAN substrate from collapsing during the drying process, thereby preserving the overall filtration performance of the PEM membrane after prolonged drying.

To assess the distinct effects of substrate deformation versus PEM compaction on membrane structure alterations, glycerol was exclusively incorporated into the PEM. The water permeability of these membranes (HPAN-GPEM) exhibited a gradual decline with drying time, as shown in Figure 5.5c. After 1 hour of drying, the water permeability was 20.1 ± 1.8 L m^{-2} h^{-1} bar^{-1}, decreasing to 17.9 ± 0.2 L m^{-2} h^{-1} bar^{-1} after 4 hours. Moreover, prolonged drying for 24 hours led to an obvious decrease in water permeability, registering 12.8 ± 0.3 m^{-2} h^{-1} bar^{-1}. The final permeability was much higher than that in the case of HPAN-PEM (3.7 L m^{-2} h^{-1} bar^{-1}), suggesting that the glycerol in PEM diffused to the HPAN and reduced the deformation degree of the HPAN. However, the PEG rejection curves remained similar (Figure 5.5c) and the average pore radii remained around 2.0 nm (Figure S5.4) for the PEM membranes after 1, 4, and 24 hours of drying, indicating that the selective layer retained its separation capability. The decreased pore size compared to the initial pore size of the HPAN-PEM membrane (4.4 ± 1.3 nm) was likely due to glycerol incorporation in the PEM, which reduced its free volume. These results suggested that while glycerol within the PEM mitigated structural changes, the unprotected HPAN substrate still underwent pore collapse over prolonged drying, leading to a reduction in water permeability.

Lastly, when glycerol was introduced into both the PEM and the HPAN substrate, the water permeability, PEG rejection curves (Figure 5.5d), and average pore radii (Figure S5.4) of these PEM membranes all remained nearly constant with drying time, as expected.

The specific role that glycerol plays in the drying process of PEMs remains a subject of debate in current research. Gherasim et al. (2016) showed that PEM membranes were dipped into a 20 wt.% glycerol aqueous solution to prevent the pores from collapsing during drying. It was believed that covalent crosslinking between PEI and the aldehyde impurities in glycerol had happened, as the imine bonds (C=N) were found. In contrast to Gherasim's findings, Li et al. (2022) found that there was no interaction between PEI and glycerol and concluded that glycerol only protected the PEM membrane from pore collapse. In our study, the glycerol incorporated into the PEM layer gradually diffused into the upper region of the HPAN substrate. Glycerol's strong hygroscopic nature enabled it to retain residual moisture at the PEM-HPAN interface, effectively preventing complete dehydration. This localized moisture retention helped mitigate the mechanical stresses that arise from differential shrinkage between the PEM and HPAN substrate. As a result, the formation of cracks or delamination was suppressed. In sum, incorporating glycerol into the PEM layer effectively prevented the shrinkage-induced tearing of both the PEM and HPAN layers, thereby preserving membrane integrity during the drying process.

5.4 Conclusion

In this work, the drying process of PEM membranes on HPAN substrates is systematically investigated, focusing on both the support and selective layers, as well as the protective role of glycerol. The HPAN substrate is notably susceptible to pore collapse during drying, resulting in a significant decrease in water permeability as drying time progresses. For the PEM membrane, the

three distinct stages characterized the effect of drying on PEM membrane filtration performance: in the 0-2 hour period, the retention capacity increased while water permeability was maintained, mainly reflecting the effect of PEM compaction; during the 2-4 hour period, intensified drying resulted in a drastic reduction in water permeability with retention capacity remaining stable, mainly as a result of the substrate collapse; and in the 4-24 hour period, prolonged drying further reduced water permeability, increased average pore size, and diminished the retention capacity, largely as a result of interfacial stress-caused fissure of the PEM.

Glycerol plays an essential role in mitigating these adverse effects. On the one hand, incorporation of glycerol solely into the substrate effectively prevents substrate pore collapse, although the drying process still induces slight compaction of the PEM and a modest reduction in water permeability. On the other hand, exclusive incorporation of glycerol into the PEM itself successfully avoids tearing, thereby preserving the average pore size and retention performance. Ultimately, incorporating glycerol into either the substrate or the PEM layer helps preserve membrane performance during drying by retaining bound water through hydrogen bonding. Glycerol can also diffuse between the substrate and the PEM film, helping to prevent pore collapse in the substrate and compaction in the PEM, thereby maintaining the filtration performance of the PEM membranes during the drying process.

Acknowledgement

This work was supported by Hong Kong Research Grants Council's General Research Fund Scheme (15214222) and Science, Technology and Innovation Commission of Shenzhen Municipality (SGDX20210823103401009).

Appendix C: Supporting Information for Chapter 5

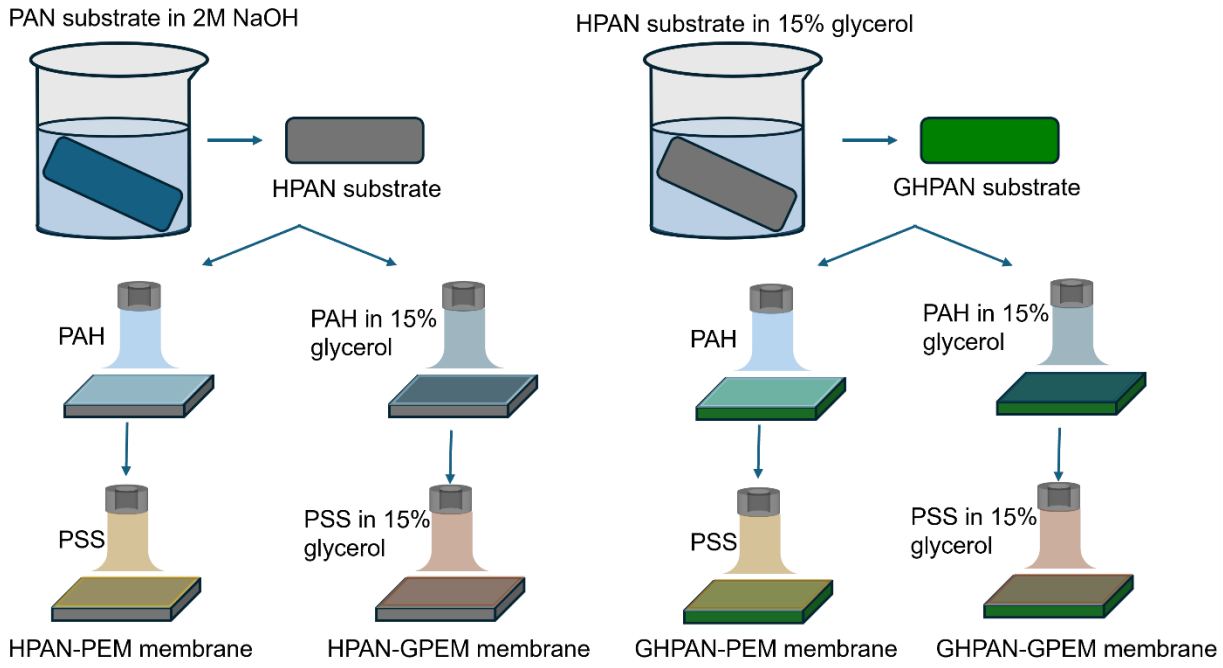

Figure S5.1 Schematic illustration of the membrane fabrication process for substrates (HPAN and GHPAN) and PEM membranes (HPAN-PEM, GHPAN-PEM, HPAN-GPEM, and GHPAN-GPEM).

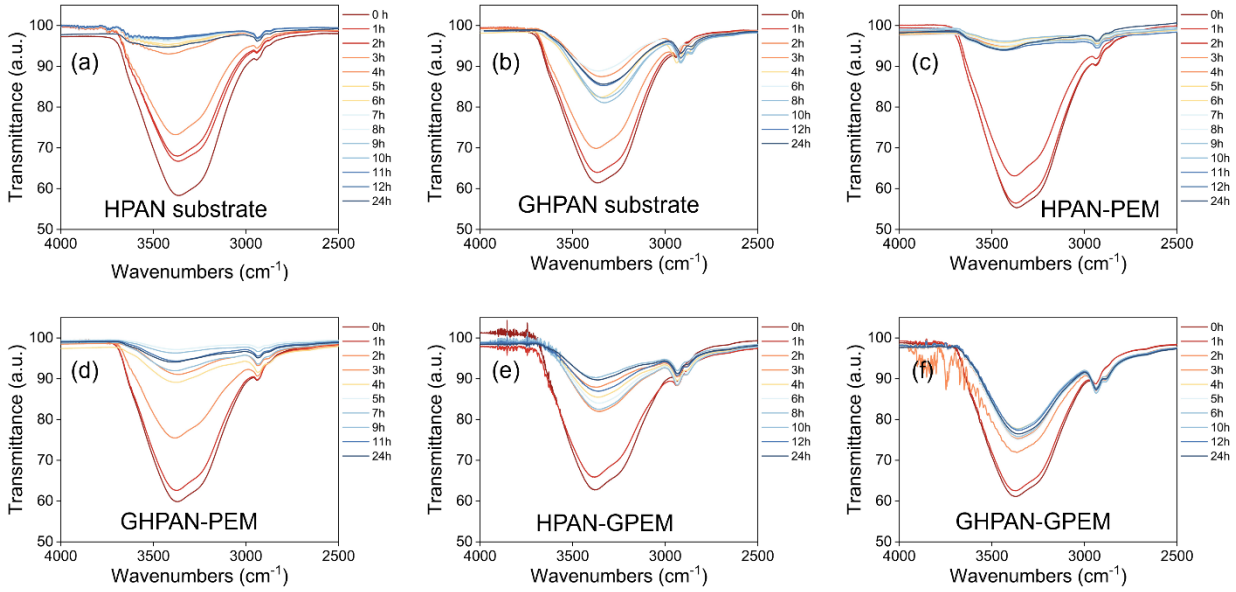

Figure S5.2 FTIR spectra of various membranes during 24-hour drying at 60% relative humidity: (a) HPAN substrate, (b) glycerol pre-filled HPAN substrate (GHPAN), (c) PEM membrane fabricated on the HPAN substrate (HPAN-PEM), (d) PEM membranes fabricated on glycerol pre-filled HPAN substrates (GHPAN-PEM), (c) PEM membranes with exclusive glycerol incorporation in the PEM (HPAN-GPEM), (d) PEM membranes with glycerol incorporation in both the PEM and the HPAN substrate (GHPAN-GPEM).

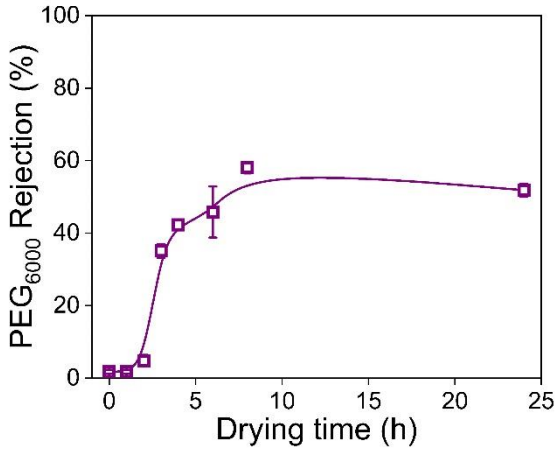

Figure S5.3 PEG6000 rejection of the HPAN substrate during 24-hour drying at 60% relative humidity.

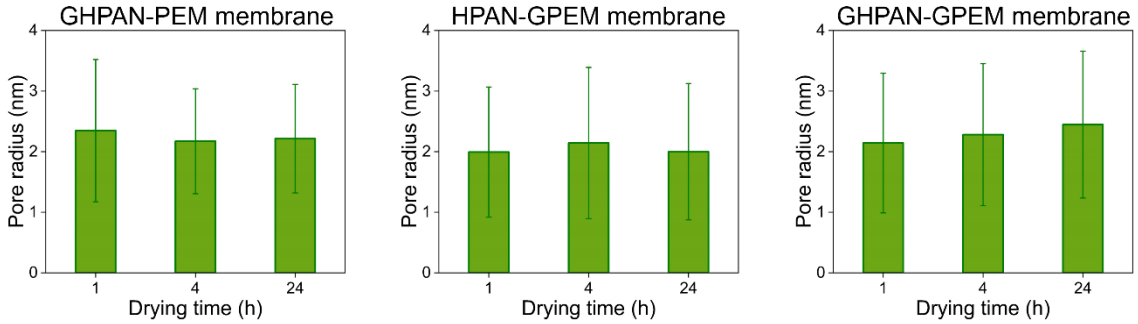

Figure S5.4 Pore radius of the PEM membranes after 1, 4, and 24 hours of drying time at 60% relative humidity.

Chapter 6. Conclusions, Impacts, and Future Directions

6.1 Conclusions

This thesis has established systematic fabrication-structure-performance relationships regarding the PEM NF membranes obtained via AAP. These fabrication-structure-performance relationships can be used to develop novel NF membranes with tunable permeability and selectivity with applications in various water or wastewater treatment scenarios. The main conclusions are summarized as follows:

(1) Aerosol-assisted printing can evenly distribute ultrafine polyelectrolyte droplets and precisely control the stacking of PE to form a PEM. The thickness of the polyelectrolyte layer and PEM shows linear growth as the printing scans increase. During the PEM assembly, two adjacent oppositely charged PE layers are strongly interdigitated, forming a PEC layer. PE interdigitation forms an effective polymeric network barrier, which increases resistance to solute and water transport.

(2) Larger droplets during nebulization retain greater momentum and thereby achieve more efficient deposition onto the substrate. Higher deposition efficiency of PE droplets results in the formation of thicker layers, thereby engendering a higher overall hydraulic resistance. Higher charge density of the PE pair leads to a denser PEM membrane.

(3) By manipulating the PE deposition mass and layering, PEM membranes with tunable pore radii (0.40-0.56 nm) and water permeability (5-60 $L \cdot m^{-2} \cdot h^{-1} \cdot bar^{-1}$) were obtained for various water treatment applications, ranging from micropollutant removal to humic acid filtration.

(4) The drying of the PEM membranes has three sequential stages: initial PEM compaction, subsequent substrate deformation, and eventual PEM tearing caused by interfacial stress. The substrate deformation drives permeability loss, and selective PEM layer compaction

controls selectivity. These differences stem from the different elastic moduli and pore architectures of the PEM and the PAN substrate. Incorporating glycerol as a pore-preserving additive, either in the substrate or within the PEM, effectively maintains the PEM membrane structure during drying and facilitates preserving its separation performance.

6.2 Impacts

The novel aerosol-assisted printing technique for fabricating PEM NF membranes addresses the longstanding scalability limitations of conventional methods such as dip coating. This breakthrough enables rapid, efficient, and material-saving membrane production, making it more feasible for industrial-scale applications. For example, the $(PEI_3PSS_3)_2$ membrane with an area of 64.8 cm^2 was fabricated efficiently using only 18 min and 6 mL of the PE solution. In contrast, a typical time of several hours and solutions of hundreds of milliliters are needed for the preparation of a two-bilayer PEM membrane of similar size by dip coating (Gopalakrishnan et al., 2024; Liang and Lin, 2021; Scheepers et al., 2023). The fabrication time can be further shortened by using arrays of spray nozzles.

The ability to rapidly deposit materials in a controlled and efficient manner is a key advantage of this AAP method, making it a promising approach for various applications that require thin, uniform coatings. Fine-tuning membrane structure and performance through precise control of the printing process provides a new platform for customized water treatment. Furthermore, the method can be extended to functional materials, such as metal nanoparticles, carbon nanotubes, and two-dimensional materials (graphene oxide (Jiang et al., 2015), covalent organic framework (Wienkamp et al., 2025), and metal-organic framework (Hurrle et al., 2017)), opening new pathways for advanced antifouling and catalytic membrane surfaces. Overall, these advancements

contribute significantly to the development of next-generation membrane technologies for safe and sustainable water treatment.

6.3 Future Directions

While this study provides novel insights into tailoring PEM NF membranes via the AAP technique, several questions should be explored in the future.

(1) The aerosol-assisted printing technique can be further improved for scalable fabrication. Incorporating multiple nozzles in a parallel array can expand the coating area without compromising deposition density, allowing high-throughput membrane production. In addition, integrating the process into a roll-to-roll configuration would further enhance scalability by enabling continuous coating of large-area substrates. Multi-nozzle arrays and roll-to-roll integration provide a promising pathway toward industrial-scale membrane fabrication using aerosol-assisted printing.

(2) Micropollutants can be effectively removed by tuning the pore size of PEM NF membranes through steric hindrance in this study. However, other separation mechanisms, such as hydrophobic interactions, electrostatic effects, and dielectric exclusion, also play important roles. A deeper understanding of these mechanisms is still needed to fully elucidate their contributions to PEM membrane performance. Gaining detailed insights into these rejection pathways will be crucial for designing next-generation membranes capable of addressing a broad spectrum of micropollutants, particularly the pressing challenge of removing persistent and hazardous compounds like per-and polyfluoroalkyl substances.

(3) Incorporating functional additives into PE solutions provides a versatile strategy for enhancing the performance of PEM NF membranes. For instance, the addition of carbon-based nanomaterials such as graphene oxide or carbon nanotubes can improve mechanical

strength and permeability by increasing free volume and creating additional water transport pathways. Hydrophilic additives like zwitterionic compounds can enhance antifouling properties and water affinity, while cross-linking agents such as glutaraldehyde can improve chemical stability and resistance to chlorine degradation. These tailored modifications enable the fabrication of PEM membranes with tunable selectivity, improved durability under harsh operating conditions, and expanded applicability for complex water and wastewater treatment scenarios.

Reference

Agranovski, I. (2011) Aerosols: science and technology, John Wiley & Sons.

Alemu, D., Wei, H.Y., Ho, K.C. and Chu, C.W. 2012. Highly conductive PEDOT: PSS electrode by simple film treatment with methanol for ITO-free polymer solar cells. Energy & Environmental Science 5(11), 9662-9671.

Azinfar, A. and Helm, C.A. 2023. Self-patterning of polyelectrolyte multilayer films: The roles of PSS molecular weight, the top layer, and post-preparation treatment. Macromolecules 56(8), 3095-3109.

Azinfar, A., Neuber, S., Vancova, M., Sterba, J., Stranak, V. and Helm, C.A. 2021. Self-patterning polyelectrolyte multilayer films: Influence of deposition steps and drying in a vacuum. Langmuir 37(35), 10490-10498.

Ba, C., Ladner, D.A. and Economy, J. 2010. Using polyelectrolyte coatings to improve fouling resistance of a positively charged nanofiltration membrane. Journal of Membrane Science 347(1-2), 250-259.

Badalov, S., Oren, Y. and Arnusch, C.J. 2015. Ink-jet printing assisted fabrication of patterned thin film composite membranes. Journal of Membrane Science 493, 508-514.

Bandini, S. and Vezzani, D. 2003. Nanofiltration modeling: the role of dielectric exclusion in membrane characterization. Chemical Engineering Science 58(15), 3303-3326.

Bang, J.H. and Suslick, K.S. 2010. Applications of Ultrasound to the Synthesis of Nanostructured Materials. Advanced materials (Weinheim) 22(10), 1039-1059.

Barui, S. 2021. 3D inkjet printing of biomaterials: Principles and applications. Medical Devices & Sensors 4(1), e10143.

Bashir, J., Ilyas, S., Asif, A., de Vos, W.M., Khan, A.L. and Akhtar, F.H. 2025. Polyelectrolyte Multilayer-Based Nanofiltration Membranes with Tunable Performance for Target Pollutants. ACS Applied Polymer Materials 7(5), 3147-3156.

Bason, S. and Freger, V. 2010. Phenomenological analysis of transport of mono- and divalent ions in nanofiltration. Journal of Membrane Science 360(1), 389-396.

Bason, S., Kaufman, Y. and Freger, V. 2010. Analysis of ion transport in nanofiltration using phenomenological coefficients and structural characteristics. The Journal of Physical Chemistry B 114(10), 3510-3517.

Batys, P., Zhang, Y., Lutkenhaus, J.L. and Sammalkorpi, M. 2018. Hydration and Temperature Response of Water Mobility in Poly(diallyldimethylammonium)–Poly(sodium 4-styrenesulfonate) Complexes. Macromolecules 51(20), 8268-8277.

Beerlage, M.A. (1994) Polyimide ultrafiltration membranes for non-aqueous systems.

Beeson, R. 1998 Thermal inkjet: Meeting the applications challenge, pp. 27-30, Society of Imaging Science and Technology.

Bidwai, S. 2025 Membrane Separation Technology Market Size and Forecast 2025 to 2034.

Bigioni, T.P., Lin, X.-M., Nguyen, T.T., Corwin, E.I., Witten, T.A. and Jaeger, H.M. 2006. Kinetically driven self assembly of highly ordered nanoparticle monolayers. Nature Materials 5(4), 265-270.

Boo, C., Wang, Y., Zucker, I., Choo, Y., Osuji, C.O. and Elimelech, M. 2018a. High Performance Nanofiltration Membrane for Effective Removal of Perfluoroalkyl Substances at High Water Recovery. Environmental Science & Technology 52(13), 7279-7288.

Boo, C., Wang, Y.K., Zucker, I., Choo, Y., Osuji, C.O. and Elimelech, M. 2018b. High performance nanofiltration membrane for effective removal of perfluoroalkyl substances at high water recovery. Environmental Science & Technology 52(13), 7279-7288.

Born, M. 1920. Volumen und hydratationswärme der ionen. Zeitschrift für physik 1(1), 45-48.

Bose, S., Keller, S.S., Alstrøm, T.S., Boisen, A. and Almdal, K. 2013. Process optimization of ultrasonic spray coating of polymer films. Langmuir 29(23), 6911-6919.

Bowen, W.R. and Mohammad, A.W. 1998. Characterization and prediction of nanofiltration membrane performance-a general assessment. Chemical Engineering Research and Design 76(8), 885-893.

Bowen, W.R., Mohammad, A.W. and Hilal, N. 1997. Characterisation of nanofiltration membranes for predictive purposes -use of salts, uncharged solutes and atomic force microscopy. Journal of Membrane Science 126(1), 91-105.

Brinke, E.t., Reurink, D.M., Achterhuis, I., de Grooth, J. and de Vos, W.M. 2020. Asymmetric polyelectrolyte multilayer membranes with ultrathin separation layers for highly efficient micropollutant removal. Applied Materials Today 18, 100471.

Castelnovo, M. and Joanny, J.-F. 2000. Formation of polyelectrolyte multilayers. Langmuir 16(19), 7524-7532.

Chen, G., Gu, Y., Tsang, H., Hines, D.R. and Das, S. 2018. The effect of droplet sizes on overspray in aerosol‐jet printing. Advanced Engineering Materials 20(8), 1701084.

Chen, S., Wu, Y., Mi, F., Lin, Y., Yu, L. and Sung, H. 2004. A novel pH-sensitive hydrogel composed of N,O-carboxymethyl chitosan and alginate cross-linked by genipin for protein drug delivery. Journal of Controlled Release 96(2), 285-300.

Chen, Y.F. and Lin, Y.C. 2009. Surface modifications of Al-Zn-Mg alloy using combined EDM with ultrasonic machining and addition of TiC particles into the dielectric. Journal of Materials Processing Technology 209(9), 4343-4350.

Cheng, W., Liu, C., Tong, T., Epsztein, R., Sun, M., Verduzco, R., Ma, J. and Elimelech, M. 2018a. Selective removal of divalent cations by polyelectrolyte multilayer nanofiltration membrane: Role of polyelectrolyte charge, ion size, and ionic strength. Journal of Membrane Science 559, 98-106.

Cheng, X.Q., Wang, Z.X., Zhang, Y., Zhang, Y., Ma, J. and Shao, L. 2018b. Bio-inspired loose nanofiltration membranes with optimized separation performance for antibiotics removals. Journal of Membrane Science 554, 385-394.

Chiarelli, P.A., Johal, M.S., Casson, J.L., Roberts, J.B., Robinson, J.M. and Wang, H.L. 2001. Controlled fabrication of polyelectrolyte multilayer thin films using spin-assembly. Advanced Materials 13(15), 1167.

Cho, J., Char, K., Hong, J.D. and Lee, K.B. 2001. Fabrication of highly ordered multilayer films using a spin self-assembly method. Advanced Materials 13(14), 1076.

Cho, K.L., Hill, A.J., Caruso, F. and Kentish, S.E. 2015. Chlorine Resistant Glutaraldehyde Crosslinked Polyelectrolyte Multilayer Membranes for Desalination. Advanced Materials 27(17), 2791-2796.

Cho, K.L., Lomas, H., Hill, A.J., Caruso, F. and Kentish, S.E. 2014. Spray Assembled, Cross-Linked Polyelectrolyte Multilayer Membranes for Salt Removal. Langmuir 30(29), 8784-8790.

Choi, W., Gu, J.-E., Park, S.-H., Kim, S., Bang, J., Baek, K.-Y., Park, B., Lee, J.S., Chan, E.P. and Lee, J.-H. 2015. Tailor-Made Polyamide Membranes for Water Desalination. ACS Nano 9(1), 345-355.

Choi, Y.J. and Lee, L.S. 2017. Partitioning behavior of bisphenol alternatives BPS and BPAF compared to BPA. Environmental Science & Technology 51(7), 3725-3732.

Cranston, E.D. and Gray, D.G. 2006. Morphological and optical characterization of polyelectrolyte multilayers incorporating nanocrystalline cellulose. Biomacromolecules 7(9), 2522-2530.

Dang, H.Q., Price, W.E. and Nghiem, L.D. 2014. The effects of feed solution temperature on pore size and trace organic contaminant rejection by the nanofiltration membrane NF270. Separation and Purification Technology 125, 43-51.

Davis, S.S. 1978. Physico-chemical studies on aerosol solutions for drug delivery I. Water-propylene glycol systems. International Journal of Pharmaceutics 1(2), 71-83.

de Grooth, J., Haakmeester, B., Wever, C., Potreck, J., de Vos, W.M. and Nijmeijer, K. 2015. Long term physical and chemical stability of polyelectrolyte multilayer membranes. Journal of Membrane Science 489, 153-159.

Decher, G., Hong, J.D. and Schmitt, J. 1992. Buildup of ultrathin multilayer films by a self-assembly process: III. Consecutively alternating adsorption of anionic and cationic polyelectrolytes on charged surfaces. Thin Solid Films 210(1-2), 831-835.

Deen, W.M. 1987. Hindered transport of large molecules in liquid-filled pores. AICHE journal 33(9), 1409-1425.

Déjugnat, C., Köhler, K., Dubois, M., Sukhorukov, G.B., Möhwald, H., Zemb, T. and Guttmann, P. 2007. Membrane densification of heated polyelectrolyte multilayer capsules characterized by soft X-ray microscopy. Advanced materials 19(10), 1331-1336.

Dierendonck, M., De Koker, S., De Rycke, R. and De Geest, B.G. 2014. Just spray it - LbL assembly enters a new age. Soft Matter 10(6), 804-807.

Dinçer, İ. and Zamfirescu, C. (2016) Drying phenomena: theory and applications, John Wiley & Sons.

Dubas, S.T. and Schlenoff, J.B. 1999. Factors controlling the growth of polyelectrolyte multilayers. Macromolecules 32(24), 8153-8160.

DuChanois, R.M., Epsztein, R., Trivedi, J.A. and Elimelech, M. 2019. Controlling pore structure of polyelectrolyte multilayer nanofiltration membranes by tuning polyelectrolyte-salt interactions. Journal of Membrane Science 581, 413-420.

DuChanois, R.M., Mazurowski, L., Fan, H., Verduzco, R., Nir, O. and Elimelech, M. 2023. Precise Cation Separations with Composite Cation-Exchange Membranes: Role of Base Layer Properties. Environmental Science & Technology 57(15), 6331-6341.

Durmaz, E.N., Sahin, S., Virga, E., de Beer, S., de Smet, L.C.P.M. and de Vos, W.M. 2021. Polyelectrolytes as Building Blocks for Next-Generation Membranes with Advanced Functionalities. ACS Applied Polymer Materials 3(9), 4347-4374.

Elshof, M.G., de Vos, W.M., de Grooth, J. and Benes, N.E. 2020. On the long-term pH stability of polyelectrolyte multilayer nanofiltration membranes. Journal of Membrane Science 615, 118532.

Emonds, S., Kamp, J., Viermann, R., Kalde, A., Roth, H. and Wessling, M.J.J.o.M.S. 2022. Open and dense hollow fiber nanofiltration membranes through a streamlined polyelectrolyte-based spinning process. Journal of Membrane Science 644, 120100.

Evdochenko, E., Kamp, J., Femmer, R., Xu, Y., Nikonenko, V.V. and Wessling, M. 2020. Unraveling the effect of charge distribution in a polyelectrolyte multilayer nanofiltration membrane on its ion transport properties. Journal of Membrane Science 611, 118045.

Fathizadeh, M., Tien, H.N., Khivantsev, K., Chen, J.-T. and Yu, M. 2017. Printing ultrathin graphene oxide nanofiltration membranes for water purification. Journal of Materials Chemistry A 5(39), 20860-20866.

Felton, L.A. 2013. Mechanisms of polymeric film formation. International Journal of Pharmaceutics 457(2), 423-427.

Feng, J.Q., Go, L.-S., Calubayan, J. and Tomaska, R. 2021. Working mechanism and behavior of Collison nebulizer. Aerosol Science and Engineering 5(3), 285-291.

Finbloom, J.A., Raghavan, P., Kwon, M., Kharbikar, B.N., Yu, M.A. and Desai, T.A. Codelivery of synergistic antimicrobials with polyelectrolyte nanocomplexes to treat bacterial biofilms and lung infections. Science Advances 9(3), eade8039.

Friedlander, S.K. and Smoke, D. 2000 Haze: Fundamentals of aerosol dynamics, Oxford University Press, New York.

Friedlander, S.K.J.N.Y. 1977. Smoke, dust and haze: Fundamentals of aerosol behavior.

Fu, J. and Schlenoff, J.B. 2016. Driving forces for oppositely charged polyion association in aqueous solutions: enthalpic, entropic, but not electrostatic. Journal of the American Chemical Society 138(3), 980-990.

Gan, L., Zhang, J., Wu, Y., Chen, Z., Zhao, Z., Lin, S. and Jiang, Y. 2025. Tailoring polyelectrolyte multilayer nanofiltration membranes by aerosol-assisted printing: Insights into membrane formation mechanisms. Environmental Science & Technology 59(1), 913-923.

Gao, P., Hunter, A., Benavides, S., Summe, M.J., Gao, F. and Phillip, W.A. 2016. Template synthesis of nanostructured polymeric membranes by inkjet printing. ACS Applied Materials & Interfaces 8(5), 3386-3395.

Gao, X., He, C., Xiao, C., Zhuang, X. and Chen, X. 2013. Biodegradable pH-responsive polyacrylic acid derivative hydrogels with tunable swelling behavior for oral delivery of insulin. Polymer 54(7), 1786-1793.

Gao, Y., Wang, K., Wang, X. and Huang, X. 2022. Exploitation of Amine Groups Cooped up in Polyamide Nanofiltration Membranes to Achieve High Rejection of Micropollutants and High Permeance of Divalent Cations. Environmental Science & Technology 56(15), 10954-10962.

Gherasim, C.V., Luelf, T., Roth, H. and Wessling, M. 2016. Dual-charged hollow fiber membranes for low-pressure nanofiltration based on polyelectrolyte complexes: One-step fabrication with tailored functionalities. ACS Applied Materials & Interfaces 8(29), 19145-19157.

Gilbert, J.B., Rubner, M.F. and Cohen, R.E. 2013. Depth-profiling X-ray photoelectron spectroscopy (XPS) analysis of interlayer diffusion in polyelectrolyte multilayers. Proceedings of the National Academy of Sciences 110(17), 6651-6656.

Gopalakrishnan, A., Janardhanan, D.V., Sasi, S., Aravindakumar, C.T. and Aravind, U.K. 2024. Organic micropollutant removal and phosphate recovery by polyelectrolyte multilayer membranes: Impact of buildup interactions. Chemosphere 350, 141078.

Gummel, J., Cousin, F. and Boué, F. 2007. Counterions Release from Electrostatic Complexes of Polyelectrolytes and Proteins of Opposite Charge: A Direct Measurement. Journal of the American Chemical Society 129(18), 5806-5807.

Guo, H., Deng, Y., Tao, Z., Yao, Z., Wang, J., Lin, C., Zhang, T., Zhu, B. and Tang, C.Y. 2016. Does hydrophilic polydopamine coating enhance membrane rejection of hydrophobic endocrine-disrupting compounds? Environmental Science & Technology Letters 3(9), 332-338.

Guo, Y., Geng, W. and Sun, J. 2009. Layer-by-Layer Deposition of Polyelectrolyte−Polyelectrolyte Complexes for Multilayer Film Fabrication. Langmuir 25(2), 1004-1010.

Hart, M.B., Scotto, C.S., Tucker, J.E., McPherson, D.C., Minter, Z., Kesavan, J., Silcott, D., Lin, H.B. and Eversole, J.D. 2020. Toward biological aerosol reference standards. Aerosol Science and Technology 54(5), 601-610.

Hartig, S.M., Greene, R.R., Dikov, M.M., Prokop, A. and Davidson, J.M. 2007. Multifunctional nanoparticulate polyelectrolyte complexes. Pharmaceutical research 24, 2353-2369.

Haynie, D.T., Cho, E. and Waduge, P. 2011. "In and out diffusion" hypothesis of exponential multilayer film buildup revisited. Langmuir 27(9), 5700-5704.

He, P. and Derby, B. 2017. Controlling coffee ring formation during drying of inkjet printed 2D inks. Advanced materials interfaces 4(22), n/a.

Higaki, Y., Nishida, J., Takenaka, A., Yoshimatsu, R., Kobayashi, M. and Takahara, A.J.P.J. 2015. Versatile inhibition of marine organism settlement by zwitterionic polymer brushes. Polymer Journal 47(12), 811-818.

Hinds, W.C. (1999) Aerosol technology : Properties, behavior, and measurement of airborne particles, Wiley, New York.

Ho, T.T.M., Bremmell, K.E., Krasowska, M., MacWilliams, S.V., Richard, C.J.E., Stringer, D.N. and Beattie, D.A. 2015. In situ ATR FTIR spectroscopic study of the formation and hydration of a fucoidan/chitosan polyelectrolyte multilayer. Langmuir 31(41), 11249-11259.

Huang, W.-P., Hu, J.-Q., Qian, H.-L., Ren, K.-F. and Ji, J. 2022. Dynamic structural controlment for the functionalization of polyelectrolyte multilayer films. Supramolecular Materials 1, 100016.

Hurrle, S., Friebe, S., Wohlgemuth, J., Wöll, C., Caro, J. and Heinke, L. 2017. Sprayable, large-area metal–organic framework films and membranes of varying thickness. Chemistry : a European journal 23(10), 2294-2298.

Ilyas, S., de Grooth, J., Nijmeijer, K. and de Vos, W.M. 2015. Multifunctional polyelectrolyte multilayers as nanofiltration membranes and as sacrificial layers for easy membrane cleaning. Journal of Colloid and Interface Science 446, 386-393.

Israelachvili, J.N. (2010) Intermolecular and Surface Forces, Elsevier Science & Technology, Chantilly.

Izquierdo, A., Ono, S.S., Voegel, J.C., Schaaf, P. and Decher, G. 2005. Dipping versus spraying: Exploring the deposition conditions for speeding up layer-by-layer assembly. Langmuir 21(16), 7558-7567.

Izumrudov, V.A., Mussabayeva, B.K. and Murzagulova, K.B. 2018. Polyelectrolyte multilayers: Preparation and applications. Russian Chemical Reviews 87(2), 192.

Jean, B., Dubreuil, F., Heux, L. and Cousin, F. 2008. Structural details of cellulose nanocrystals/polyelectrolytes multilayers probed by neutron reflectivity and AFM. Langmuir 24(7), 3452-3458.

Ji, Y., An, Q., Zhao, Q., Chen, H., Qian, J. and Gao, C. 2010. Fabrication and performance of a new type of charged nanofiltration membrane based on polyelectrolyte complex. Journal of Membrane Science 357(1), 80-89.

Jiang, Y., Wang, W. N., Liu, D., Nie, Y., Li, W., Wu, J., Zhang, F., Biswas, P. and Fortner, J.D. 2015. Engineered crumpled graphene oxide nanocomposite membrane assemblies for advanced water treatment processes. Environmental Science & Technology 49(11), 6846-6854.

Jiang, Y., Wang, W., Biswas, P. and Fortner, J.D. 2014. Facile aerosol synthesis and characterization of ternary crumpled graphene-TiO_2-magnetite nanocomposites for advanced water treatment. ACS Applied Materials & Interfaces Journal 6(14), 11766-11774.

Jones, C.S., Lu, X., Renn, M., Stroder, M. and Shih, W.-S. 2010. Aerosol-jet-printed, high-speed, flexible thin-film transistor made using single-walled carbon nanotube solution. Microelectronic Engineering 87(3), 434-437.

Jonkers, W.A., de Vos, W.M. and te Brinke, E. 2024. Asymmetric polyelectrolyte multilayer membranes: Influence of bottom section polycation on layer growth and retention mechanisms. Journal of Membrane Science 698, 122577.

Junker, M.A., de Vos, W.M., de Grooth, J. and Lammertink, R.G.H. 2023. Relating uncharged solute retention of polyelectrolyte multilayer nanofiltration membranes to effective structural properties. Journal of Membrane Science 668, 121164.

Kim, S.H., Hong, K., Lee, K.H. and Frisbie, C.D. 2013. Performance and stability of aerosol-jet-printed electrolyte-gated transistors based on poly (3-hexylthiophene). ACS Applied Materials & Interfaces 5(14), 6580-6585.

Klitzing, R.v. 2006. Internal structure of polyelectrolyte multilayer assemblies. Physical Chemistry Chemical Physics 8(43), 5012-5033.

Koehler, R., Steitz, R. and von Klitzing, R. 2014. About different types of water in swollen polyelectrolyte multilayers. Advances in Colloid and Interface Science 207, 325-331.

Krasemann, L. and Tieke, B. 2000. Selective ion transport across self-assembled alternating multilayers of cationic and anionic polyelectrolytes. Langmuir 16(2), 287-290.

Krogman, K.C., Zacharia, N.S., Schroeder, S. and Hammond, P.T. 2007. Automated Process for Improved Uniformity and Versatility of Layer-by-Layer Deposition. Langmuir 23(6), 3137-3141.

Kusoglu, A. and Weber, A.Z. 2017. New Insights into Perfluorinated Sulfonic-Acid Ionomers. Chemical Reviews 117(3), 987-1104.

Kwon, Y.-N. and Leckie, J.O. 2006. Hypochlorite degradation of crosslinked polyamide membranes: II. Changes in hydrogen bonding behavior and performance. Journal of Membrane Science 282(1), 456-464.

Li, C., Hu, D., Liu, L., Zhu, L., Xu, M., Wang, C. and Li, Y. 2022. Polyelectrolyte complex nanofiltration membranes by surface deposition of polyethylenimine on polyanion supports. Journal of Applied Polymer Science 139(19), 52137.

Li, Q., Chen, G.Q., Liu, L. and Kentish, S.E. 2018. Spray assisted layer-by-layer assembled one-bilayer polyelectrolyte reverse osmosis membranes. Journal of Membrane Science 564, 501-507.

Li, X., Liu, C. and Van der Bruggen, B. 2020. Polyelectrolytes self-assembly: Versatile membrane fabrication strategy. Journal of Materials Chemistry A 8(40), 20870-20896.

Liang, Y. and Lin, S. 2020. Intercalation of zwitterionic surfactants dramatically enhances the performance of low-pressure nanofiltration membrane. Journal of Membrane Science 596, 117726.

Liang, Y. and Lin, S. 2021. Mechanism of permselectivity enhancement in polyelectrolyte-dense nanofiltration membranes via surfactant-assembly intercalation. Environmental Science & Technology 55(1), 738-748.

Liang, Y., Zhu, Y., Liu, C., Lee, K.R., Hung, W.S., Wang, Z., Li, Y., Elimelech, M., Jin, J. and Lin, S. 2020. Polyamide nanofiltration membrane with highly uniform sub-nanometre pores for sub-1 A precision separation. Nat Commun 11(1), 2015.

Liu, C., Shi, L. and Wang, R. 2015. Crosslinked layer-by-layer polyelectrolyte nanofiltration hollow fiber membrane for low-pressure water softening with the presence of SO_4^{2-} in feed water. Journal of Membrane Science 486, 169-176.

Liu, Y., Wang, K., Zhou, Z., Wei, X., Xia, S., Wang, X.-m., Xie, Y.F. and Huang, X. 2022. Boosting the performance of nanofiltration membranes in removing organic micropollutants:

trade-off effect, strategy evaluation, and prospective development. Environmental Science & Technology 56(22), 15220-15237.

Liu, Y., Wang, X., Yang, H., Xie, Y.F. and Huang, X. 2019. Preparation of nanofiltration membranes for high rejection of organic micropollutants and low rejection of divalent cations. Journal of Membrane Science 572, 152-160.

Lösche, M., Schmitt, J., Decher, G., Bouwman, W.G. and Kjaer, K. 1998. Detailed structure of molecularly thin polyelectrolyte multilayer films on solid substrates as revealed by neutron reflectometry. Macromolecules 31(25), 8893-8906.

Ma, D., Li, H., Meng, Z., Zhang, C., Zhou, J., Xia, J. and Wang, Y. 2021. Absolute and fast removal of viruses and bacteria from water by spraying-assembled carbon-nanotube membranes. Environmental Science & Technology 55(22), 15206-15214.

Ma, Y. and Sun, J. 2009. Humido-and thermo-responsive free-standing films mimicking the petals of the morning glory flower. Chemistry of Materials 21(5), 898-902.

Macdonald, W. and Pan, C. 1974 Method for drying water-wet membranes, Google Patents.

Malaisamy, R. and Bruening, M.L. 2005. High-flux nanofiltration membranes prepared by adsorption of multilayer polyelectrolyte membranes on polymeric supports. Langmuir 21(23), 10587-10592.

Manisha, B. and Devendra, V. (2017) Advances in Biomaterials for Biomedical Applications, p. 66, Springer.

Martin, G.D. and Hutchings, I.M. 2012. Fundamentals of inkjet technology. Inkjet technology for digital fabrication, 21-44.

May, K.R. 1973. The collison nebulizer: Description, performance and application. Journal of Aerosol Science 4(3), 235-243.

Mc Callion, O.N.M., Taylor, K.M.G., Thomas, M. and Taylor, A.J. 1996. The influence of surface tension on aerosols produced by medical nebulisers. International Journal of Pharmaceutics 129(1), 123-136.

McCallion, O.N., Taylor, K.M., Thomas, M. and Taylor, A.J. 1995. Nebulization of fluids of different physicochemical properties with air-jet and ultrasonic nebulizers. Pharmaceutical research 12, 1682-1688.

Mermut, O., Lefebvre, J., Gray, D.G. and Barrett, C.J. 2003. Structural and mechanical properties of polyelectrolyte multilayer films studied by AFM. Macromolecules 36(23), 8819-8824.

Michaels, A.S. and Miekka, R.G. 1961. Polycation-polyanion complexes: preparation and properties of poly-(vinylbenzyltrimethylammonium) poly-(styrenesulfonate). The Journal of Physical Chemistry 65(10), 1765-1773.

Mitra, S. and Kundagrami, A. 2023. Polyelectrolyte complexation of two oppositely charged symmetric polymers: A minimal theory. The Journal of chemical physics 158(1), 014904-014904.

Modi, S., Foston, M.B. and Biswas, P. 2023. Controlled synthesis of smaller than 100 nm lignin nanoparticles in a furnace aerosol reactor. ACS ES&T Engineering 3(5), 671-681.

Mohammed, M.A., Sproncken, C.C.M., Gumí-Audenis, B., Lazdanaité, E., Stabile, R., Voets, I.K. and Raz, O. 2020. Reversibly programmable photonics via responsive polyelectrolyte multilayer cladding. Advanced optical materials 8(16), n/a.

Molazemhosseini, A., Magagnin, L., Vena, P. and Liu, C.-C. 2017. Single-use nonenzymatic glucose biosensor based on CuO nanoparticles ink printed on thin film gold electrode by micro-plotter technology. Journal of Electroanalytical Chemistry 789, 50-57.

Morelos-Gomez, A., Cruz-Silva, R., Muramatsu, H., Ortiz-Medina, J., Araki, T., Fukuyo, T., Tejima, S., Takeuchi, K., Hayashi, T., Terrones, M. and Endo, M. 2017. Effective NaCl and dye

rejection of hybrid graphene oxide/graphene layered membranes. Nature Nanotechnology 12(11), 1083-1088.

Nakao, S. and Kimura, S. 1981. Analysis of solutes rejection in ultrafiltration. Journal of Chemical Engineering of Japan 14(1), 32-37.

Ng, L.Y., Mohammad, A.W. and Ng, C.Y. 2013. A review on nanofiltration membrane fabrication and modification using polyelectrolytes: Effective ways to develop membrane selective barriers and rejection capability. Advances in Colloid and Interface Science 197-198, 85-107.

Nghiem, L.D., Schäfer, A.I. and Elimelech, M. 2004. Removal of natural hormones by nanofiltration membranes: measurement, modeling, and mechanisms. Environmental Science & Technology 38(6), 1888-1896.

Ou, Z. and Muthukumar, M. 2006. Entropy and enthalpy of polyelectrolyte complexation: Langevin dynamics simulations. The Journal of Chemical Physics 124(15).

Ouyang, L., Malaisamy, R. and Bruening, M.L. 2008. Multilayer polyelectrolyte films as nanofiltration membranes for separating monovalent and divalent cations. Journal of Membrane Science 310(1), 76-84.

Paltrinieri, L., Wang, M., Sachdeva, S., Besseling, N.A.M., Sudhölter, E.J.R. and De Smet, L.C.P.M. 2017. Fe_3O_4 nanoparticles coated with a guanidinium-functionalized polyelectrolyte extend the pH range for phosphate binding. Journal of Materials Chemistry. A, 5(35), 18476-18485.

Picart, C., Mutterer, J., Richert, L., Luo, Y., Prestwich, G.D., Schaaf, P., Voegel, J.C. and Lavalle, P. 2002. Molecular basis for the explanation of the exponential growth of polyelectrolyte multilayers. Proceedings of the National Academy of Sciences 99(20), 12531-12535.

Porcel, C.H., Izquierdo, A., Ball, V., Decher, G., Voegel, J.C. and Schaaf, P. 2005. Ultrathin coatings and (poly (glutamic acid)/polyallylamine) films deposited by continuous and simultaneous spraying. Langmuir 21(2), 800-802.

Qi, S., Li, W., Zhao, Y., Ma, N., Wei, J., Chin, T.W. and Tang, C.Y. 2012. Influence of the properties of layer-by-layer active layers on forward osmosis performance. Journal of Membrane Science 423-424, 536-542.

Rathee, V.S., Sidky, H., Sikora, B.J. and Whitmer, J.K. 2018. Role of associative charging in the entropy–energy balance of polyelectrolyte complexes. Journal of the American Chemical Society 140(45), 15319-15328.

Regenspurg, J.A., Jonkers, W.A., Junker, M.A., Achterhuis, I., te Brinke, E. and de Vos, W.M. 2024. Polyelectrolyte multilayer membranes: An experimental review. Desalination 583, 117693.

Regenspurg, J.A., Martins Costa, A.F., Achterhuis, I. and de Vos, W.M. 2022. Influence of molecular weight on the performance of polyelectrolyte multilayer nanofiltration membranes. ACS Applied Polymer Materials 4(5), 2962-2971.

Reurink, D.M., te Brinke, E., Achterhuis, I., Roesink, H.D.W. and de Vos, W.M. 2019. Nafion-based low-hydration polyelectrolyte multilayer membranes for enhanced water purification. ACS Applied Polymer Materials 1(9), 2543-2551.

Reurink, D.M., Willott, J.D., Roesink, H.D.W. and de Vos, W.M. 2020. Role of polycation and cross-linking in polyelectrolyte multilayer membranes. ACS Applied Polymer Materials 2(11), 5278-5289.

Richardson, J.J., Björnmalm, M. and Caruso, F. 2015. Technology-driven layer-by-layer assembly of nanofilms. Science 348(6233), aaa2491.

Sakai, S. 2000 Dynamics of piezoelectric inkjet printing systems, pp. 15-20, Society of Imaging Science and Technology.

Salary, R.R., Lombardi, J.P., Weerawarne, D.L., Rao, P.K. and Poliks, M.D. A state-of-the-art review on aerosol jet printing (AJP) additive manufacturing process, American Society of Mechanical Engineers, NEW YORK.

Saleh, E., Zhang, F., He, Y., Vaithilingam, J., Fernandez, J.L., Wildman, R., Ashcroft, I., Hague, R., Dickens, P. and Tuck, C. 2017. 3D inkjet printing of electronics using UV conversion. Advanced Materials Technologies 2(10), 1700134.

Salomäki, M. and Kankare, J. 2008. Specific anion effect in swelling of polyelectrolyte multilayers. Macromolecules 41(12), 4423-4428.

Sanyal, O., Liu, Z., Meharg, B.M., Liao, W. and Lee, I. 2015. Development of polyelectrolyte multilayer membranes to reduce the COD level of electrocoagulation treated high-strength wastewater. Journal of Membrane Science 496, 259-266.

Scardaci, V., Coull, R., Lyons, P.E., Rickard, D. and Coleman, J.N. 2011. Spray deposition of highly transparent, low-resistance networks of silver nanowires over large areas. Small 7(18), 2621-2628.

Schaaf, P., Voegel, J.C., Jierry, L. and Boulmedais, F. 2012. Spray-assisted polyelectrolyte multilayer buildup: From step-by-step to single-step polyelectrolyte film constructions. Advanced Materials 24(8), 1001-1016.

Scheepers, D., de Keizer, J., Borneman, Z. and Nijmeijer, K. 2023. The pH as a tool to tailor the performance of symmetric and asymmetric layer-by-layer nanofiltration membranes. Journal of Membrane Science 670, 121320.

Schlenoff, J.B. and Dubas, S.T. 2001. Mechanism of polyelectrolyte multilayer growth: charge overcompensation and distribution. Macromolecules 34(3), 592-598.

Schlenoff, J.B., Dubas, S.T. and Farhat, T. 2000. Sprayed polyelectrolyte multilayers. Langmuir 16(26), 9968-9969.

Secrist, K.E. and Nolte, A.J. 2011. Humidity swelling/deswelling hysteresis in a polyelectrolyte multilayer film. Macromolecules 44(8), 2859-2865.

Seiti, M., Degryse, O., Monica Ferraro, R., Giliani, S., Bloemen, V. and Ferraris, E. 2023. 3D Aerosol Jet® printing for microstructuring: Advantages and limitations. International Journal of Bioprinting 9(6), 257.

Shin, D.Y., Moon, Y.J., Kim, J.Y. and Kang, K.-T. 2023. Measurement of inkjet droplet size based on Fraunhofer diffraction. Review of Scientific Instruments 94(10).

Shiratori, S.S. and Rubner, M.F. 2000. pH-dependent thickness behavior of sequentially adsorbed layers of weak polyelectrolytes. Macromolecules 33(11), 4213-4219.

Sigurdardottir, S.B., DuChanois, R.M., Epsztein, R., Pinelo, M. and Elimelech, M. 2020. Energy barriers to anion transport in polyelectrolyte multilayer nanofiltration membranes: Role of intra-pore diffusion. Journal of Membrane Science 603, 117921.

Sill, A., Nestler, P., Azinfar, A. and Helm, C.A. 2019. Tailorable polyanion diffusion coefficient in LbL films: The role of polycation molecular weight and polymer conformation. Macromolecules 52(22), 9045-9052.

Sill, A., Nestler, P., Thran, P. and Helm, C.A. 2021. Dependence of PSS diffusion in multilayers of entangled PDADMA on temperature and salt concentration: More than one diffusion constant. Macromolecules 54(20), 9372-9384.

Smith, P.J. and Shin, D.H. (2012) Inkjet-based micromanufacturing, John Wiley & Sons.

Solis, F.J. and De La Cruz, M.O. 2000. Flexible linear polyelectrolytes in multivalent salt solutions: Solubility conditions. EPJ Direct 2, 1-18.

Son, M., Yang, W., Bucs, S.S., Nava-Ocampo, M.F., Vrouwenvelder, J.S. and Logan, B.E. 2018. Polyelectrolyte-based sacrificial protective layer for fouling control in reverse osmosis desalination. Environmental Science & Technology Letters 5(9), 584-590.

Steckel, H. and Eskandar, F. 2003. Factors affecting aerosol performance during nebulization with jet and ultrasonic nebulizers. European Journal of Pharmaceutical Sciences 19(5), 443-455.

Taketa, T.B., Rocha Neto, J.B.M., dos Santos, D.M., Fiamingo, A., Beppu, M.M., Campana-Filho, S.P., Cohen, R.E. and Rubner, M.F. 2020. Tracking sulfonated polystyrene diffusion in a chitosan/carboxymethyl cellulose layer-by-layer film: Exploring the internal architecture of nanocoatings. Langmuir 36(18), 4985-4994.

Tang, H., Ji, S., Gong, L., Guo, H. and Zhang, G. 2013. Tubular ceramic-based multilayer separation membranes using spray layer-by-layer assembly. Polymer Chemistry 4(23), 5621-5628.

te Brinke, E., Achterhuis, I., Reurink, D.M., de Grooth, J. and de Vos, W.M. 2020. Multiple approaches to the buildup of asymmetric polyelectrolyte multilayer membranes for efficient water purification. ACS Applied Polymer Materials 2(2), 715-724.

Tempel, H., Joshi, R. and Schneider, J.J. 2010. Ink jet printing of ferritin as method for selective catalyst patterning and growth of multiwalled carbon nanotubes. Materials Chemistry and Physics 121(1), 178-183.

Thünemann, A.F., Müller, M., Dautzenberg, H., Joanny, J.-F. and Löwen, H. (2004) Polyelectrolytes with Defined Molecular Architecture II. Schmidt, M. (ed), pp. 113-171, Springer Berlin Heidelberg, Berlin, Heidelberg.

Towle, E.G., Ding, I. and Peterson, A.M. 2020. Impact of molecular weight on polyelectrolyte multilayer assembly and surface properties. Journal of Colloid Interface Science 570, 135-142.

Tüfekci, M., Durak, S.G., Pir, İ., Acar, T.O., Demirkol, G.T. and Tüfekci, N. 2020. Manufacturing, characterisation and mechanical analysis of polyacrylonitrile membranes. Polymers 12(10), 2378.

V Klitzing, R. 2006. Internal structure of polyelectrolyte multilayer assemblies. Physical Chemistry Chemical Physics 8(43), 5012-5033.

Wan, Z. and Jiang, Y. 2021. Synthesis-structure-performance relationships of nanocomposite polymeric ultrafiltration membranes: A comparative study of two carbon nanofillers. Journal of Membrane Science 620.

Wang, C., Park, M.J., Gonzales, R.R., Matsuyama, H., Drioli, E. and Shon, H.K. 2023. Graphene oxide-based layer-by-layer nanofiltration membrane using inkjet for desalination. Desalination 549.

Wang, C., Park, M.J., Seo, D.H., Phuntsho, S., Gonzales, R.R., Matsuyama, H., Drioli, E. and Shon, H.K. 2022a. Inkjet printed polyelectrolyte multilayer membrane using a polyketone support for organic solvent nanofiltration. Journal of Membrane Science 642, 119943.

Wang, K., Fu, W., Wang, X.-m., Xu, C., Gao, Y., Liu, Y., Zhang, X. and Huang, X. 2022b. Molecular design of the polyamide layer structure of nanofiltration membranes by sacrificing hydrolyzable groups toward enhanced separation performance. Environmental Science & Technology 56(24), 17955-17964.

Wang, K., Wang, X., Januszewski, B., Liu, Y., Li, D., Fu, R., Elimelech, M. and Huang, X. 2022c. Tailored design of nanofiltration membranes for water treatment based on synthesis-property-performance relationships. Chemical Society Reviews 51(2), 672-719.

Wang, L., Wang, L. and Su, Z. 2011. Surface defects in polyelectrolyte multilayers: Effects of drying and deposition cycle. Soft Matter 7(10), 4851-4855.

Wang, N., Zhang, G., Ji, S., Qin, Z. and Liu, Z. 2010. The salt-, pH- and oxidant-responsive pervaporation behaviors of weak polyelectrolyte multilayer membranes. Journal of Membrane Science 354(1), 14-22.

Wang, W.N., Jiang, Y. and Biswas, P. 2012. Evaporation-induced crumpling of graphene oxide nanosheets in aerosolized droplets: Confinement force relationship. The Journal of Physical Chemistry Letters 3(21), 3228-3233.

Wang, W.N., Kaihatsu, Y., Iskandar, F. and Okuyama, K. 2009. Highly luminous hollow chloroapatite phosphors formed by a template-free aerosol route for solid-state lighting. Chemistry of Materials Journal 21(19), 4685-4691.

Wang, W.N., Widiyastuti, W., Lenggoro, I.W., Kim, T.O. and Okuyama, K. 2007. Photoluminescence optimization of luminescent nanocomposites fabricated by spray pyrolysis of a colloid-solution precursor. Journal of The Electrochemical Society 154(4), J121-J128.

Wang, Y., Zucker, I., Boo, C. and Elimelech, M. 2021. Removal of emerging wastewater organic contaminants by polyelectrolyte multilayer nanofiltration membranes with tailored selectivity. ACS ES&T Engineering 1(3), 404-414.

Widom, B. 2004. Capillarity and wetting phenomena: Drops, bubbles, pearls, waves. Physics Today 57(12), 66-67.

Wienkamp, K., Wallraff, A., Wessling, M. and Roth, H. 2025. Separation of complex multi-salt-organic mixtures containing lithium salts with polyelectrolyte multilayer nanofiltration membranes. Desalination 614, 119026.

Wijshoff, H. 2018. Drop dynamics in the inkjet printing process. Current Opinion in Colloid & Interface Science 36, 20-27.

Wilkinson, N.J., Smith, M.A.A., Kay, R.W. and Harris, R.A. 2019. A review of aerosol jet printing-a non-traditional hybrid process for micro-manufacturing. The International Journal of Advanced Manufacturing Technology 105(11), 4599-4619.

Wong, J.E., Rehfeldt, F., Hänni, P., Tanaka, M. and Klitzing, R.v. 2004. Swelling behavior of polyelectrolyte multilayers in saturated water vapor. Macromolecules 37(19), 7285-7289.

Xiang, F., Givens, T.M. and Grunlan, J.C. 2015. Fast spray deposition of super gas barrier polyelectrolyte multilayer thin films. Industrial & Engineering Chemistry Research 54(19), 5254-5260.

Xiong, T., Li, C., He, X., Xie, B., Zong, J., Jiang, Y., Ma, W., Wu, F., Fei, J., Yu, P. and Mao, L. 2023. Neuromorphic functions with a polyelectrolyte-confined fluidic memristor. Science 379(6628), 156-161.

Xu, R., Zhang, Z., Deng, C., Nie, C., Wang, L., Shi, W., Lyu, T. and Yang, Q. 2024. Micropollutant rejection by nanofiltration membranes: A mini review dedicated to the critical factors and modelling prediction. Environmental Research 244, 117935.

Yang, Z., Long, L., Wu, C.Y. and Tang, C.Y. 2022. High permeance or high selectivity? Optimization of system-scale nanofiltration performance constrained by the upper bound. ACS ES&T Engineering 2(3), 377-390.

Yassari, M., Karami, P., Taghipour, A., Rahimpour, A. and Sadrzadeh, M. 2025. Sustainable layer-by-layer assembled nanofiltration membranes with optimized pore size for lithium-magnesium selective separation. Journal of Environmental Chemical Engineering 13(3), 116478.

Yoo, D., Shiratori, S.S. and Rubner, M.F. 1998. Controlling bilayer composition and surface wettability of sequentially adsorbed multilayers of weak polyelectrolytes. Macromolecules 31(13), 4309-4318.

Yu, J., Jackson, N.E., Xu, X., Morgenstern, Y., Kaufman, Y., Ruths, M., de Pablo, J.J. and Tirrell, M. 2018. Multivalent counterions diminish the lubricity of polyelectrolyte brushes. Science 360(6396), 1434-1438.

Yuksel, S., Kabay, N. and Yuksel, M. 2013. Removal of bisphenol A (BPA) from water by various nanofiltration (NF) and reverse osmosis (RO) membranes. Journal of Hazardous Materials 263(2), 307-310.

Yunker, P.J., Still, T., Lohr, M.A. and Yodh, A.G. 2011. Suppression of the coffee-ring effect by shape-dependent capillary interactions. Nature 476(7360), 308-311.

Zacharia, N.S., Modestino, M. and Hammond, P.T. 2007. Factors influencing the interdiffusion of weak polycations in multilayers. Macromolecules 40(26), 9523-9528.

Zeng, H., Guo, J., Zhang, Y., Xing, D., Yang, F., Huang, J., Huang, S. and Shao, L. 2022. Green glycerol tailored composite membranes with boosted nanofiltration performance. Journal of Membrane Science 663, 121064.

Zhang, H., Zhang, H., Luo, J. and Wan, Y. 2019. Enzymatic cascade catalysis in a nanofiltration membrane: Engineering the microenvironment by synergism of separation and reaction. ACS Applied Materials & Interfaces Journal 11(25), 22419-22428.

Zhang, P., Qian, J.W., Yang, Y., An, Q.F., Liu, X.Q. and Gui, Z.L. 2008. Polyelectrolyte layer-by-layer self-assembly enhanced by electric field and their multilayer membranes for separating isopropanol-water mixtures. Journal of Membrane Science 320(1-2), 73-77.

Zhang, Y., Li, F., Valenzuela, L.D., Sammalkorpi, M. and Lutkenhaus, J.L. 2016. Effect of water on the thermal transition observed in poly(allylamine hydrochloride)-poly(acrylic acid) complexes. Macromolecules 49(19), 7563-7570.

Zhao, G.J., Han, W.J., Dong, L.L., Fan, H.W., Qu, Z., Gu, J.H. and Meng, H. 2022. Sprayed separation membranes: A systematic review and prospective opportunities. Green Energy & Environment 7(6), 1143-1160.

Zhao, Q., An, Q.F., Ji, Y., Qian, J. and Gao, C. 2011. Polyelectrolyte complex membranes for pervaporation, nanofiltration and fuel cell applications. Journal of Membrane Science 379(1), 19-45.

Zhao, S. and Wang, Z. 2017. A loose nano-filtration membrane prepared by coating HPAN UF membrane with modified PEI for dye reuse and desalination. Journal of Membrane Science 524, 214-224.

Zhao, Y., Tong, T., Wang, X., Lin, S., Reid, E.M. and Chen, Y. 2021. Differentiating solutes with precise nanofiltration for next generation environmental separations: a review. Environmental Science & Technology 55(3), 1359-1376.

Zhou, B., Luo, J., Jin, M., Xue, N., He, R., Li, W. and He, T. 2025. Micropollutants removal from aquaculture water using layer-by-layer self-assembled nanofiltration membranes. Water Research 271, 122933.

Zhu, Q., Shentu, B., Liu, Q. and Weng, Z. 2006. Swelling behavior of polyethylenimine-cobalt complex in water. European Polymer Journal 42(6), 1417-1422.

Zverina, L., Koch, M., Andersen, M.F., Pinelo, M., Woodley, J.M. and Daugaard, A.E. 2020. Controlled pore collapse to increase solute rejection of modified PES membranes. Journal of Membrane Science 595, 117515.